TETHERED NANOPARTICLE – POLYMER COMPOSITES: PHASE BEHAVIOR, STRUCTURE, DYNAMICS AND RHEOLOGY

A Dissertation

Presented to the Faculty of the Graduate School

of Cornell University

In Partial Fulfillment of the Requirements for the Degree of

Doctor of Philosophy

by

Samanvaya Srivastava

January 2014

TETHERED NANOPARTICLE – POLYMER COMPOSITES: PHASE BEHAVIOR, STRUCTURE, DYNAMICS AND RHEOLOGY

Samanvaya Srivastava, Ph. D.

Cornell University 2014

Nanoparticle – polymer composites, or polymer nanocomposites, are ubiquitous in the modern world. Controlled dispersion of nanoparticles in nanocomposites is often a critical requirement and has lead to evolution of a variety of strategies for regulating nanoparticle interactions and assembly. This work focuses on one such technique wherein the nanoparticle surfaces are densely tethered with polymer chains. Complete screening of the interparticle interactions and steric repulsion among the tethered chains thus results in repulsive and stable nanoparticles across a range of polymer molecular weights and chemistries and nanoparticle volume fraction. These nanoparticles are found to be ideal for studying polymer nanocomposites, and a phase diagram constructed on the basis of nanoparticle arrangements is presented.

Tethered nanoparticles, in the limit small tethered polymer chains, also serve as model systems for studying the properties of soft nanoparticles. Well-dispersed suspensions of these soft nanoparticles in oligomers exhibit unique properties across the jamming transition, including anomalous structural and dynamic trends typically associated with complex molecular fluids. In the jammed regime, these suspensions behave as typical soft glasses and allow for quantitative comparisons with the existing models for soft glasses. At the same time, the tethered chains facilitate relaxations even in the deeply jammed regime and thus lead to novel features including Newtonian behavior and terminal relaxations in the jammed suspensions. On the other end of the spectrum, studies of suspensions of these nanoparticles in extremely large polymer chains provide insights on the physical processes responsible for the atypical, negative non-Einsteinian deviations in the viscosity typically observed in blends of nanoparticles in large polymer hosts.

We also explore the origins of atypical faster – than – diffusion relaxation mechanisms in soft materials through studying the relaxation mechanisms in these jammed suspensions as well as single-component tethered nanoparticle fluids. A simple theoretical framework is presented to account for the genesis of driving mechanisms in our systems, and comparisons between theoretical and experimental results provide strong support to the existing theory that hyperdiffusion in soft materials arises from the system's response to internal stresses; however, the origin of these internal stresses might vary considerably from one material to another.

BIOGRAPHICAL SKETCH

Samanvaya Srivastava was born on February 12th, 1986 and brought up in Kanpur, Uttar Pradesh. He grew up in a *combined* family and was greatly influenced over the formative years by his grandparents. Pursuing the best education possible was always a priority for his family (his three aunts all hold Ph.D. degrees) and although he initially had ambitions of getting into the family business, his parents never allowed that to become an excuse for going easy with education.

His frequent visits to IIT Kanpur campus through family connections and exposure to its serene environment over the years deeply placed a belief in him that that was *the place to be at*. So when he was actually accepted in the institute, it was literally a dream that came true. However, he had never thought of the possibilities beyond that, and three year into the five-year program, like most of his classmates, was determined to get a job in the financial/consulting job after graduation. Priorities changed dramatically, however, when he started working on his master's thesis and he finally ended up joining Cornell University to pursue Ph.D. in chemical engineering with Lynden Archer.

Moving to Ithaca was a welcome change from the Indian-city-life for him, and he fell in love with the surroundings and the easy-going nature of the town. Last four and a half years have been a very pleasant experience for him, and he truly enjoyed his stay there and made quite a few very good friends. As he prepares to move on and face the real world, he takes away fond memories and remains certain that time spent in Ithaca will influence him greatly in the years to come.

Dedicated to my grandparents, my parents, my sister

and to the ultimate quest for knowledge.

ACKNOWLEDGMENTS

I would begin by expressing immense gratitude towards my advisor, Prof. Lynden Archer, for providing the best advice, in matters academic and otherwise. Our interactions and counsel that I received from you have made me a better person, and I can't thank you enough for it. Your enthusiasm and dedication towards research, and your management of the research group and administrative duties are an inspiration for me. If I ever become an academician and be half as good an advisor to my students as you were to me, I would consider myself successful. Thank you Professor!

The theoretical frameworks for most of my experiments owe their success to the various stimulating discussions with Prof. Donald Koch. I express my gratefulness towards him for being patient with me.

I acknowledge the suggestions that were provided by my other committee members, Prof. Itai Cohen and Prof. Emmanuel Giannelis, through the course of my Ph.D. The enthusiasm and unique vision that Prof. Cohen brought to our Rheology meetings always motivated me think in a broader context and prepared me well in facing audience outside Cornell.

In the laboratory, I would begin by thanking Praveen, Henry, Shekhar and Jen for teaching me the basics of synthesis and characterization, and getting me started. At the same time, the contribution of students who worked with me over the years – Vishal, Jay, Daniel, Shaomao and Dan, Zhengyuan and Luigi, towards this thesis is indispensible. Towards the end of my degree, my work with Rahul, Akanksha and Ritesh helped me think about research in a context larger than just laboratory work as a graduate student. I would also thank other members of the Archer group with whom I interacted with over the years, including JP, Juchen, Ric, Gil, Wanda, Luke, Zichao, Rajesh, Sung A, Alex, Yingying, Sampson, TJ, Lin, Wajdi, Pooja, Shuya, Ashwin and Madhur, for making the whole Ph.D. a very enjoyable experience.

I would also thank Prof. Fernando Escobedo, Hsiu-yu, Arijit, Anubhab and Sushmit for the various discussions that I had with them and for providing a different perspective to my experiments and “completing the picture”.

A substantial portion of my Ph.D. consists of work that was carried out at Argonne National Laboratories, and it wouldn’t have been possible to carry out any of it without the help and support of Dr. Suresh Narayanan, Dr. Alec Sandy, Dr. Xiaobing Zuo and Dr. Jan Ilavsky, and from Prof. Wesley Burghardt at Northwestern University. I extend my sincerest gratitude towards them.

I also appreciate the constant help and support over the year from the staff members at CCMR and KAUST-CU Center for energy and sustainability, including Dr. Yuanming Zhang, Dr. David Jung, Celia Szczepura and Brenda Fisher.

All my friends made my stay in Ithaca an extremely enjoyable experience. Amit and Shruti, Halder and Meloni, Vikram, Anant, Rajesh, Praveen, Umang, Henry, Bryan, Jen, Aadhar, Sasi, Raghu, Abhishek, Pankaj, Apoorva, Pooja M, Poornima, Ashwin, Sushmit, Rahul, Akanksha, Ritesh, Pooja N - the list can go on and on, and there are not enough words to express my thankfulness for all you guys. Thanks to the cricket club for keeping cricket alive in Ithaca. And to the International Cricket Council for organizing cricket all over the world, which made Ithaca winters bearable. I would also like to thank my friends from the high school and undergraduate days who are now scattered all over the world, with special thanks to Ankit, Vivek, Vibhu and Anvita, Bagri, Joshi and Deepali.

For two years, I lived in William Keeton House. I was fortunate to get a chance to work with Ethan, Jeff Cowie, Jeff Hancock, Deb and all the other staff members, and thanks to all you guys for making it such an enriching experience.

This Ph.D. would have never happened without the guidance and motivation that was provided by Vivek Sir, Prof. Ashutosh Sharma and Dipankar in my formative years, and I’ll always be indebted to them for all the encouragement that they have been providing ever since.

To my family: all your love, support and blessings have kept me going. Baba, Dadi, Nana, Nani, Papa, Mummy, Vrinda and my whole extended family never made me feel I was away from home. I'll always be indebted for everything I am to all of you.

TABLE OF CONTENTS

LIST OF FIGURES

LIST OF TABLES

CHAPTER 1

INTRODUCTION

Partly adapted with permission from

S. Srivastava, J. L. Schaefer, Z. Yang, Z. Tu, and L. A. Archer, Polymer–Particle Composites: Phase Stability and Applications in Electrochemical Energy Storage. *Advanced Materials,* in press. DOI: 10.1002/adma.201303070.

1.1. Polymer Nanocomposites

Inclusion of small inorganic objects to reinforce organic or inorganic matrices has been practiced for decades, with the earliest examples comprising of Bakelite and reinforced rubber [1]. When the dimensions of the inclusions approach nanometer length scales, large interfacial regions are created. In favorable situations, both the size and spatial distribution of these interfaces can be controlled to create new hybrid materials with physical and transport properties inaccessible in their pure constituents or in their poorly prepared mixtures [2, 3]. In recent years such polymer–nanoparticle composite materials, *nanocomposites*, have found applications in virtually every field of technology. The most notable examples include: biomedicine – where nanocomposites are used for non–isotopic sensing [4], for dental and bone implants [5-7], and are under development for tissue engineering, as well as for light, heat, and magnetically actuated materials for therapeutics delivery, diagnostics, and treatment [8-11]; water treatment and purification – where polymer–particle composites have been shown to enhance permeate flux in osmosis membranes without compromising salt rejection [12-14]; to increase the biological fouling resistance of membranes, and to selectively remove heavy metals from the water supply [12, 15-17]. And, following the seminal works from Bawendi, Alivisatos and others [18, 19],

nanocomposite materials based on conjugated–polymer/semiconductor–nanocrystals composites are increasingly finding applications in solid–state lighting and photovoltaic devices [20, 21].

Polymer–particle composites based on micron– and nano–sized structures have long been important in electrochemical energy storage technologies [22-24]. They are expected to play an even more dominant role in the future of energy storage, as recent advances in synthesis of nanoscale electrode materials in various sizes, shapes, and mass distributions [25-29], lead to scalable approaches and wider commercial use of designer nanoparticles that impart specific functionalities in commercial devices. Synergistic research aimed at understanding the beneficial and deleterious effects that come with the vast number of interfaces introduced by nanosized objects in electrochemical cells are also expected to define new strategies for integrating nanostructures in electrodes and electrolytes for batteries, capacitors, and fuel cells; strategies that might, for example, maximize their benefits for achieving fast transport, enhance active materials utilization and permit development of engineered electrodes able to absorb the mechanical stresses and strains associated with electrochemical processes in the cell, while at the same time minimizing undesirable side reactions that consume the electrolyte and electrode materials and may lead to dangerous out–gassing during battery operation.

Control of the particle dispersion state in its polymeric host is understood to represent an important first–step in enabling practical utilization of nanocomposites in most of these applications. This situation often runs counter to what is observed, particularly for nanometer–size particles, where the range and strength of the net inter–particle force typically favors particle agglomeration. Achieving polymer–particle composites with controlled distribution of particles in a host material therefore continues to be a fundamental challenge and has attracted

considerable research interest. It is a requirement for creating device components with predictable properties, performance, and lifetimes.

Nanocomposites created by physical mixing layered silicates in polymers are inexpensively prepared and were among the first materials to be studied extensively [2, 30, 31]. Mica and other phyllosilicates with characteristic sheet spacing of a few nanometers and aspect ratios as high as 1000 are currently among the most extensively studied systems. When well incorporated in polymers, these materials have been reported to yield significantly improved stiffness, mechanical strength and gas barrier properties [2]. It is now accepted that a requirement for good mixing is that the polymer and particle surface chemistries must be carefully controlled and that good dispersion is achieved only in situations where the particle surface is carefully prepared and/or conditioned and favorable polymer–particle interactions are achieved by design, or more commonly by serendipity, to overcome strong particle–particle interactions and polymer bridging, which favor agglomeration [32-34].

Recently, nanoparticles smaller than the random coil size or radius of gyration of their polymer host were shown to mix even better with the host than larger particles. Importantly, this strategy has been shown to work even in cases when the particles and host might be otherwise considered incompatible [35]. This remarkable effect is currently thought to be of entropic origin, but the precise driving force for mixing is still not well understood. Apart from these special cases, however, strong van der Waals attraction forces at the nanoscale coupled with excluded volume interactions and depletion attraction forces experienced by the polymer host typically induce strong particle–particle aggregation, frustrating all efforts to control the dispersion state. A perhaps obvious solution is to densely graft the particles with ligands that are long enough and stiff enough to prevent irreversible aggregation. This approach has inspired development of a

class of sterically stabilized nanoparticle systems [36-44], wherein partial/complete screening of the attractive forces is achieved through irreversible tethering of polymer chains on the surface of the particles and thus provides a precise control over particle dispersion irrespective of particle concentration and the surrounding environment.

1.2. Tethered Nanoparticle–Polymer Composites

The physics of nanoparticles with well–protected surfaces via chemical linking of polymeric chains on its surface is the focus of this work. The chemistry approach we have undertaken allows for extremely high grafting density of the chains (1–3 chains/nm^2) and is compatible with a variety of nanoparticle (SiO_2, ZiO_2, TiO_2, Fe_2O_3, CNTs etc.) and polymer (PEG, PI, PS, PDMS etc.) chemistries [40, 45]. The high grafting densities ensure complete screening of the attractive inter–particle van der Waals interactions and thus allow for well–dispersed nanocomposites when these tethered nanoparticles are mixed with polymeric hosts. When the tethered and host polymer are of the same chemistry, these tethered nanoparticle–polymer composites have minimal enthalpic interactions among the constitutive elements of the composites and thus serve as model systems for polymer nanocomposites, or nano–colloidal suspensions in cases when the tethered and the host polymers are of sufficiently small lengths.

An important and intriguing subclass of the nanocomposites investigated in the present work comprises of self–suspended tethered nanoparticles. These single–component suspensions have large polymer chains tethered densely on the surfaces of the nanoparticles, and exhibit fluid like properties even in the absence of any external solvent [42, 46]. A strong space–filling requirement is imposed on the tethered chains in these self–suspended nanoparticle fluids, which manifests as unique properties including long–range correlation among the nanoparticles mediated by the tethered chains, extremely homogenous nanoparticle distributions and soft

glassy behavior even at very low particle loadings [47]. This new material platform has also allowed exploration of niche applications like carbon dioxide capture [48-51] and single ion conductors [52-54], where the entropic frustration of the tethered polymers could be utilized to capture CO_2 or the single component nature of the material can be exploited to synthesize virtually immobile poly–anionic (or poly–cationic) nanoparticles.

1.2.1. Goals and Methods

The tethered nanoparticles provide for an excellent platform to study the fundamental properties of polymer nanocomposites, soft colloids and single–component nanoparticle fluids. The versatility of the material platform in allowing access to a variety of physical process is summarized in Figure 1. The goal of the present work is to explore the physical processes that govern the structure and relaxations of these systems at the nano– as well as the macro–scale. Bulk rheology, nanoparticle arrangements and bulk and nanoscale relaxations in these materials are investigated in a variety of settings by tuning the size and grafting density of the tethered chains, size of the host chains, nanoparticle size and volume fractions and temperature.

Nanoparticle structure and phase behavior of polymer nanocomposites has been studied using our in house line–collimated small angle X–ray scattering (SAXS) setup as well as a point–collimated SAXS setup at the Advanced Photon Source, Argonne National Laboratory. The flow behavior was investigated using conventional oscillatory and steady shear rheology. Relaxation events at the nanoscale were studied using X–ray photon correlation spectroscopy (XPCS) at Advanced Photon Source, Argonne National Laboratory.

1.2.2. Model Polymer Nanocomposites

As has already been discussed, it is a common practice to introduce nanoscale objects into

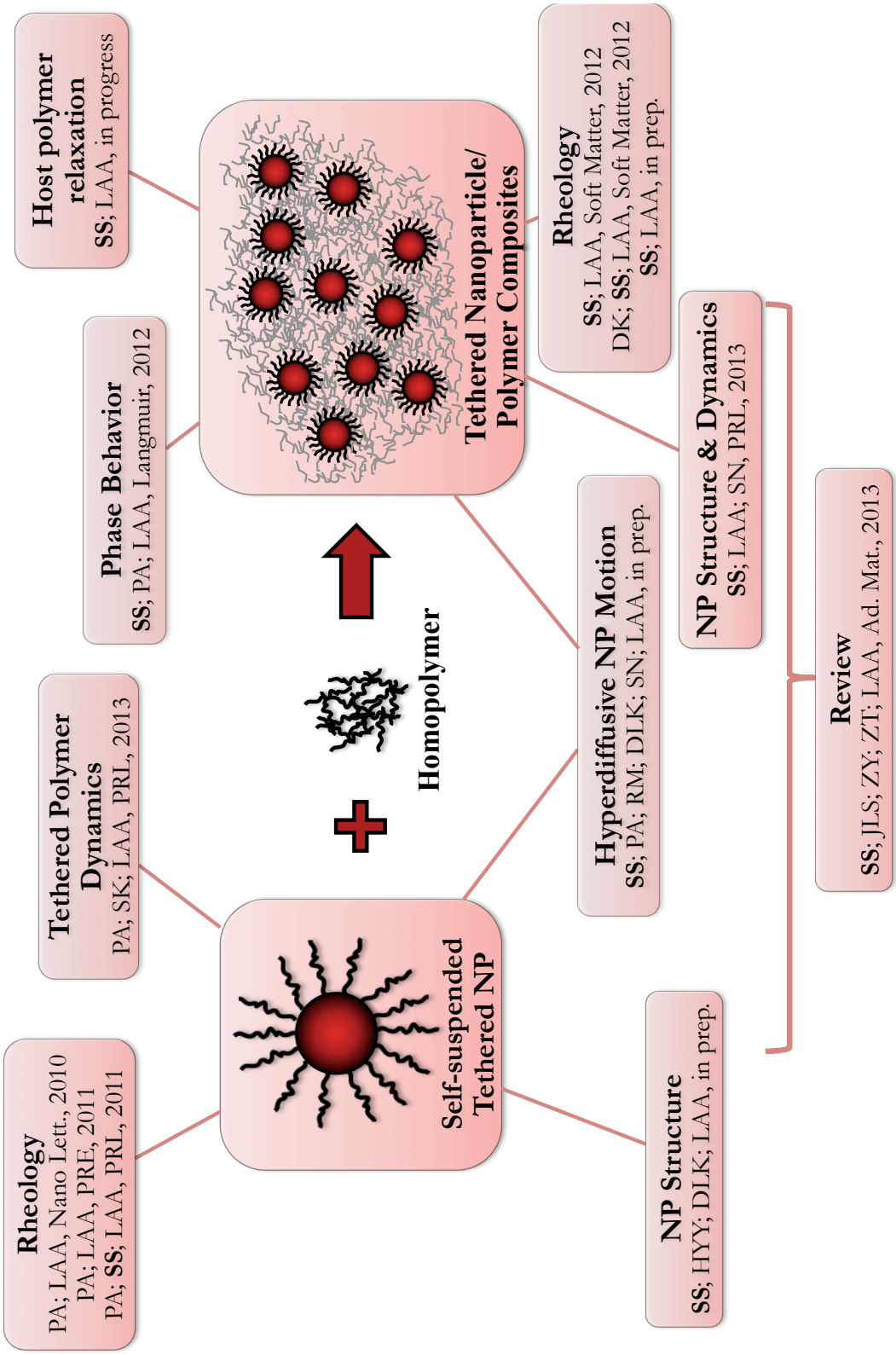

Figure 1 Tethered nanoparticle–polymer composites: a versatile platform.

organic and inorganics matrices to seek their reinforcement. Densely grafted tethered nanoparticles are model nano–objects to serve this purpose owing to an absence of enthalpic interactions among themselves and very low tendency to form agglomerate, thus alleviating the most common difficulty encountered in polymer nanocomposites. Dense grafting of the chains results in a complete remediation of agglomeration, even in cases where the nanoparticles phase separate from the host matrix, which is indeed remarkable considering the bulk of studies which have appeared in trying to address the issue of nanoparticle agglomeration in polymer hosts. Small angle X–ray studies were found to be instrumental in determining the phase behavior of tethered nanoparticles in polymer hosts and provide for a robust methodology to determine the composition of the nanocomposites even in cases when the conventional methods seem to provide ambiguous results.

Upon dispersion in extremely large polymer matrices, these tethered nanoparticles are also valuable for investigating the origins of the unconventional *non–Einsteinian* behavior of polymer nanocomposites wherein the bulk viscosity of the matrix is found to decrease upon addition of nanoparticles [55-57]. Exploiting unique combinations of the tethered and the host polymers allow for insightful experiments that probe at the flow behavior and glass transition of the bulk matrix as well as the relaxation dynamics of the nanoparticles and the polymer hosts at the nanoscale. These measurements provide for direct connections between the bulk and the nanoscale behavior of such nanocomposites and go a long way towards achieving a convincing understanding of this unique phenomenon.

1.2.3. Model Soft Glasses

Understanding the physics of glass transition and the slow dynamics of materials near the glass transition remain one of the longstanding challenges in condensed matter physics [58-61].

Colloidal systems have been of particular interest to researchers owing to their ability to mimic simple atomic and molecular systems, albeit with larger length and time scales that facilitate experimental investigations [62-64]. Soft colloids have recently garnered heightened interest arising from the richer physics associated with these systems and their ability to mimic even complex molecular systems like water [65, 66]. Both the polymer–suspended and self–suspended tethered nanoparticles exhibit flow behavior and relaxation mechanisms typically associated with soft glassy systems. In combination with an effective screening of the inter–particle interactions and facile tuning of the degree of jamming through subtle changes in the system parameters, these again serve as model systems for studying soft glasses.

The flow behavior of soft glassy materials has been described by Sollich's soft glassy rheology (SGR) model [67, 68] with reasonable success. Suspensions of tethered nanoparticles, in the limit of high particle loadings, are shown to exhibit many features that are typically associated with soft glassy materials. This work complements the investigations of soft glassy behavior of self–suspended nanoparticle fluids [69]. Qualitative and quantitative comparisons with the SGR model exhibit the versatility of our material platform in accessing a large range of features associated with soft glassy systems. A new rheology technique, termed as time–strain superposition, which reveals the very long time relaxations in soft glassy systems is also presented.

In contrast to the extremely slow relaxation events typically associated with soft glassy materials, certain soft glasses also exhibit relaxation processes that occur at fairly accessible time scales, and more importantly, are hyperdiffusive in nature [70-72]. The tethered nanoparticles employed in the present study also exhibit similar hyperdiffusive relaxations, both in the presence of a polymeric host and in the limiting case of self–suspended nanoparticles. The simplicity of the

material platform considered in this work further allows for a simple description of the hyperdiffusive relaxations, and provides valuable insights into the origins of hyperdiffusive relaxations in soft materials.

1.2.4. Model Soft Nano–Colloids

As described in the previous section, soft colloids are able to simulate complex molecular systems and are thus of even greater significance. Tethered nanoparticles also serve as model nano–colloids and investigations of the structure, dynamics and flow behavior of their suspensions in oligomers offer unique opportunities for understanding the behavior of soft colloids in particular and systems interacting with soft interaction potentials in general. The flow behavior of these nano–colloidal suspensions transits from that of a simple colloidal suspension to that of a soft glassy material over small increases in the particle loadings and serves as a model system for studying the properties of repulsive glasses across the glass transition. The structure and the relaxation processes in these suspensions exhibit an even more unique behavior upon the glass transition that has been only observed in complex molecular fluids like water and liquid silica. Thus, these model nano–colloids serve as convenient systems to study the physics of complex molecular fluids and also for comparisons with theoretical predictions.

1.3. Outline of This Dissertation

In Chapter 2 we review in extensive detail the current progress in the area of polymer nanocomposites. Structure, phase behavior and mechanical properties of composites of polymers and bare–nanoparticle as well as tethered nanoparticles, and those of single–component self–suspended nanoparticles are discussed.

Chapter 3 discusses SAXS investigation of the phase behavior of tethered nanoparticle–polymer

composites. The phase behavior is discussed in context of a phase diagram proposed for planar polymer brushes interacting with polymer melts, and important distinctions between the two cases arising from the curvature effects introduced by the small size of the nanoparticle cores are highlighted.

Chapter 4 outlines in detail the synthesis procedure followed for both self–suspended nanoparticle fluids and suspensions of tethered nanoparticles in oligomers. This is followed by an extensive report based on SAXS experiments of the nanoparticle arrangements in oligomer–suspended and self–suspended tethered nanoparticles.

In Chapter 5, we discuss the rheology of oligomer–suspended tethered nanoparticles and their comparisons with the SGR model. The flow behavior is shown to vary from resembling a simple Newtonian suspension to a soft glass. Insights on particle interactions obtained from linear viscoelastic behavior of these materials are also discussed.

Chapter 6 introduces a novel procedure for creating rheological maps of soft glasses over extremely large time scales by simple superposition of the moduli vs. frequency data obtained at different strain amplitudes. Results from experiments performed on oligomer–suspended tethered nanoparticles and calculations from the SGR model are discussed. This procedure reveals the extremely long time scales associated with bulk relaxations in soft glassy materials, and the relaxations times for a variety of soft glassy systems are compared with the model calculations.

Non–Einsteinian trends in the bulk viscosity of polymer nanocomposites comprising of tethered nanoparticles dispersed in large, entangled polymers are the focus of Chapter 7. Novel measurement techniques are employed to elucidate the origin of the unusual behavior by providing a description of the relaxation processes in the bulk and on the scale of individual particles as well as individual host chains. This chapter also introduces hyperdiffusive

relaxations observed in soft materials, which is the focus of study for Chapter 9.

Chapter 8 discusses the relaxation processes at length scales comparable to individual particles in oligomer–suspended tethered nanoparticles. XPCS measurements reveal unique features associated with these suspensions, including hyperdiffusive relaxations and the first evidences in a colloidal system of a transport anomaly typically observed in complex molecular fluids.

Finally, in Chapter 9, we discuss the origins of the peculiar hyperdiffusive relaxations observed in soft materials arising from volume heterogeneities. Hyperdiffusive relaxations are found to be a characteristic of both oligomer–suspended and self–suspended tethered nanoparticles. We present a straightforward theoretical framework to describe the genesis of hyperdiffusion in self–suspended tethered nanoparticles, which in turn strongly support the current understanding of origin of hyperdiffusion in soft materials.

CHAPTER 2

PHASE STABILITY AND MECHANICAL PROPERTIES OF POLYMER–PARTICLE COMPOSITES: A REVIEW OF LITERATURE

Adapted with permission from

S. Srivastava, J. L. Schaefer, Z. Yang, Z. Tu, and L. A. Archer, Polymer–Particle Composites: Phase Stability and Applications in Electrochemical Energy Storage. *Advanced Materials,* in press**.** DOI: 10.1002/adma.201303070.

Abstract

Polymer–particle composites are used in virtually every field of technology. When the particles approach nanometer length scales, large interfacial regions are created, which present opportunities and challenges for both basic science and applications. In favorable situations, both the size and spatial distribution of these interfaces can be controlled to create new hybrid materials with physical and transport properties inaccessible in their pure constituents or in their poorly prepared mixtures. This chapter surveys progress made primarily in the last decade in understanding phase behavior, structure, and properties of nanoparticle–polymer composites. It takes a decidedly polymers perspective of these composites and explores how physical and chemical synthesis strategies might be employed to create polymer–nanoparticle hybrids with controlled distribution of particles. We also point out opportunities in the area where recent advances in nanoparticle synthesis and polymer science are inspiring new approaches and where newcomers to the field could make important contributions.

2.1. Structure and Phase Behavior

2.1.1. Bare Nanoparticle – Polymer Composites

A majority of the earlier research on nanocomposites relied on favorable interactions between the polymer and the nanoscale object, including the extensively studied system of polymer layered silicate nanocomposites, to control the particle dispersion state. Typically, the route to synthesizing well dispersed layered silicate nanocomposites entails the selection of polymer chain chemistries and architectures that facilitate complete screening of electrostatic forces between the layers, leading to intercalated or exfoliated nanocomposites, respectively. The reader is referred to a few excellent reviews to survey recent progress in this area [3, 73, 74]. Attractive interactions between particles and a polymer host favor spontaneous absorption of the host chains in a variety of conformations (Figure 2). Whether the interactions are produced by strong ionic or weak hydrogen bonds, the interaction strength dictates the robustness of the dispersion. The ultimate dispersion state also depends sensitively on the synthesis scheme, which in turn varies significantly among nanoparticle/polymer combinations. Thus, the specific approaches employed to achieve control of the particle dispersion are as a rule quite specific and highly specialized [75, 76].

Nanocomposites based on silica nanoparticles are among the most extensively studied materials. Physical mixing of the host polymers and nanoparticles is either carried out in the presence of a common solvent with subsequent removal of the solvent or addition on nanoparticles to the polymer melt with vigorous mixing. Sonication and post–mixing annealing is often employed to maximize the interaction between the particles and the polymer and improve the dispersion. Because many metal oxides exhibit similar surface chemistry to silica in the most widely used dispersant, water, procedures used for creating silica nanocomposites are often interchangeable

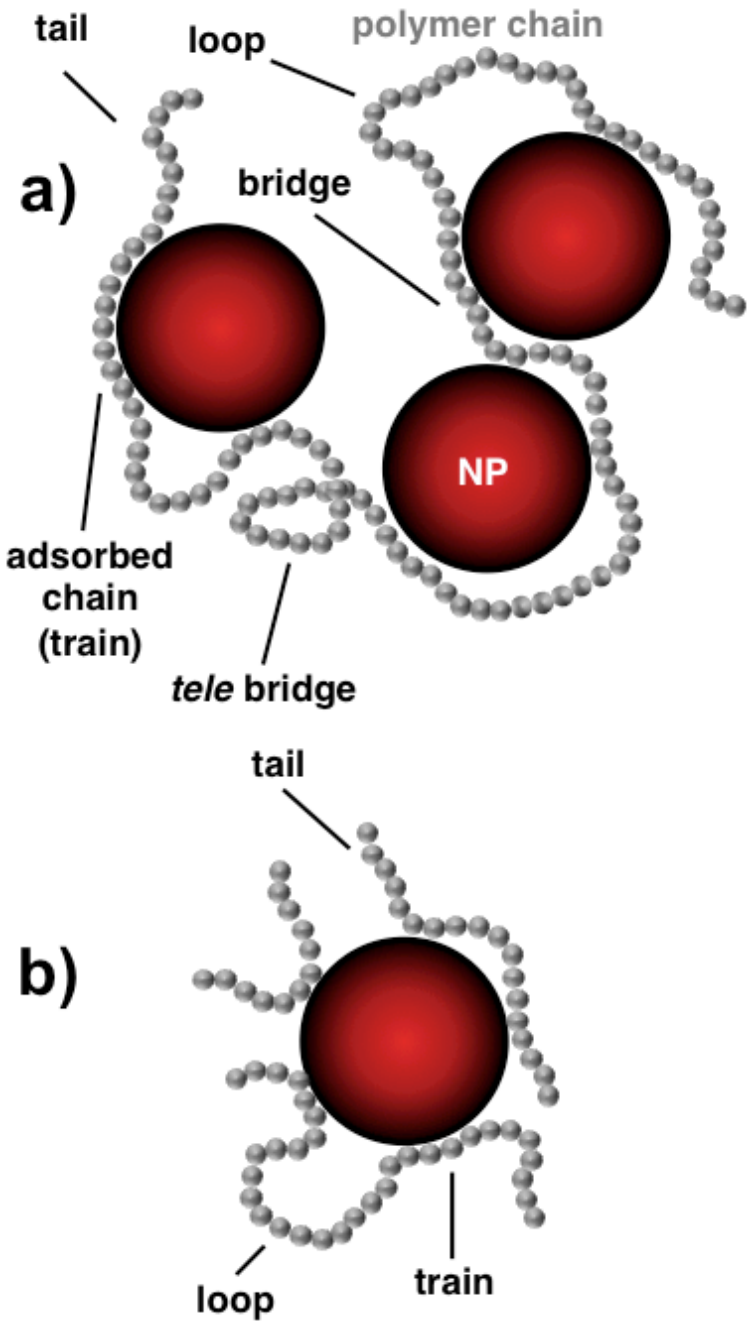

Figure 2 a, b. Typical polymer chain conformations around nanoparticles in a polymer nanocomposite.

with those used for nanocomposites based on other metal oxide particles. Colloidal silica has been reported to form good dispersions owing to large available surface area and favorable interactions with a wide variety of polymers [32, 77-83]. In some cases, long polymer chains can bridge between two or more particles (as depicted in Figure 2), which can lead to further strengthening of the composite. The propensity of different polymers to absorb on the particle surface therefore provides a good rule–of–thumb for assessing the dispersion state of nanoparticles.

Although much confusion exists in the early literature about the surface chemistry of silica, it is now known that the isoelectric point of silica particles in salt–free, aqueous media lies between pH of 4 and 5 [84]. At pH values above 5, SiO_2 particles present around 4.2 hydroxyl groups per square nanometer of surface and are negatively charged. The number of surface hydroxyls and charge increase almost continuously as the pH rises to about 11, at which point the particles spontaneously dissolve to form silicate ions in solution. At pH values below 4, SiO_2 exhibits a positive surface charge in salt–free aqueous solution. At neutral pH, pristine or ion–exchanged silica particles possess large numbers of surface hydroxyl groups that may form particle–particle bridges over time, leading to aggregation, or may serve as adsorption sites for ions or polar macromolecules, leading to stable dispersions. It is then unsurprising that suspensions of SiO_2 particles in highly polar polymers such as polyethylene oxide (PEO) [32, 33, 77], poly (methyl acrylate) [78], poly (methyl methacrylate) [79, 80], poly (2–vinylpyridine) and poly (ethyl methacrylate) [79] are found to be very stable, whereas those based on less polar polyethylene oxide dimethyl ether [77] are only moderately stable. And composites based on most organic polymers, including polystyrene [76, 81], and polytetrahydrofuran [77] are unstable, leading to spontaneous formation of diffusion–limited fractal like aggregate structures. Further, as the SiO_2

particle dimensions approach nanometer–scales, the number of surface hydroxyl groups become so large, that the probability of particle–particle collisions leading to bridging is essentially unity and it becomes virtually impossible to maintain a stable dispersion even in polar polymers over long time, leading to significant aging of the properties of the nanocomposites which appear to be very stable over short time scales.

Notwithstanding these obvious difficulties, a large body of work has been devoted towards understanding the dispersion state of SiO_2–polymer nanocomposites prepared using mechanical mixing and polymer processing techniques. These studies show that the details of the preparation method and annealing history of the nanocomposite affect the dispersion state appreciably, even in cases where favorable polymer–particle interactions might suggest good dispersion [78, 82, 83]. SiO_2–poly (methyl acrylate) composites, for example, have been shown, with the help of X–ray scattering and electron microscopy, to exhibit highly process– and time–dependent morphologies as shown in Figure 3 [78]. This last finding is important because it highlights that the long time scales associated with diffusion of chains in a high–molar mass host polymer will invariably lead to errors in the initial assessment of the particle dispersion state. Motion of the chains from/to the particle surface can produce gradual changes in the properties of the nanocomposite over time, where either coarsening of particle aggregates or improvement in the dispersion state of the nanoparticles might occur depending on the form of interactions between the particle and the polymer [82, 83]. These effects are further complicated by the rich milieu of conformational and dynamic transitions polymer chains experience near adsorbing surfaces [46, 85-87].

The general consensus is that bare nanoparticles either immediately or over time form aggregates when mixed with a polymer and are thus best suited for applications where polymer

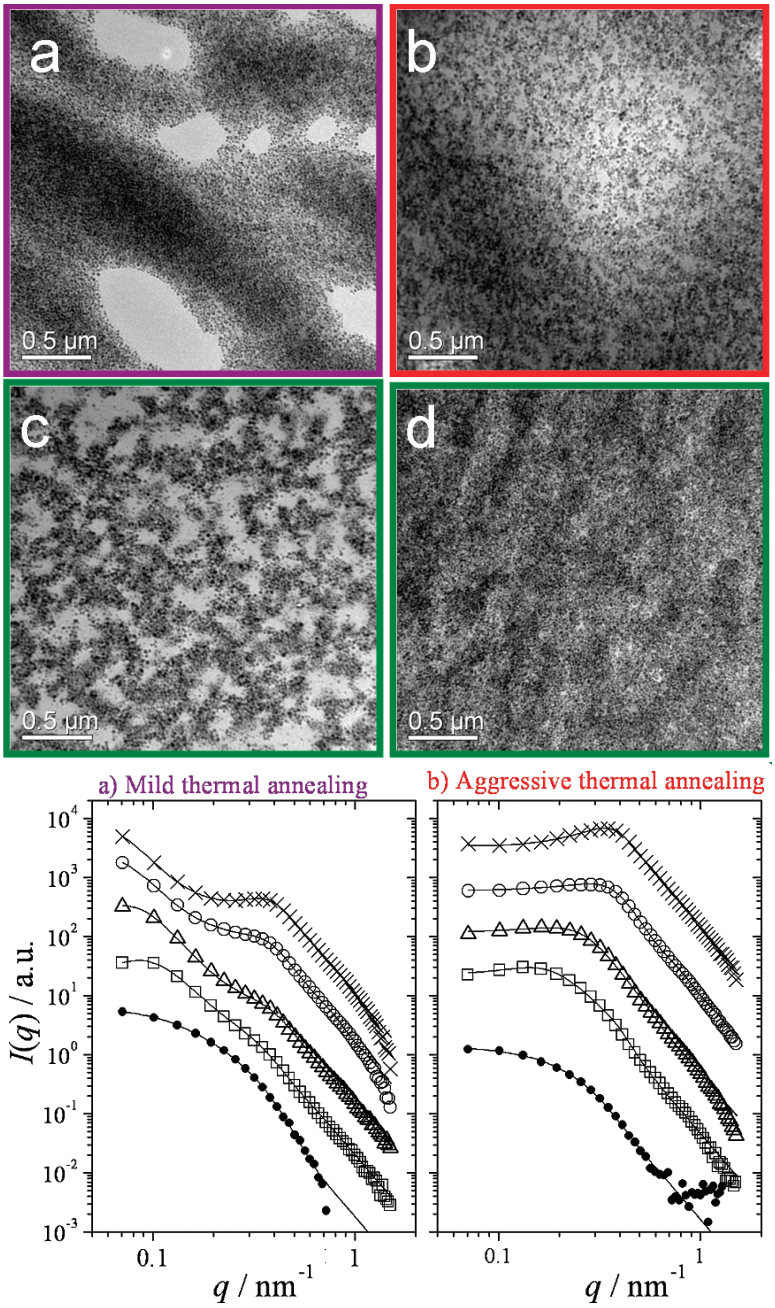

Figure 3 Electron micrographs and X–ray scattering profiles depicting the variations in particle dispersion morphologies in silica/poly(methyl acrylate) composites following different post–casting treatments. Adapted with permission from D. W. Janes, J. F. Moll, S. E. Harton, C. J. Durning, Macromolecules 2011, 44, 4920. Copyright 2011 American Chemical Society.

nanocomposites with a connected network of particles percolating through the polymer are desired. Anisotropic particles achieve percolation at even lower particle loadings, as has been shown for rod shaped particles in comparison to spheres, and it becomes practically viable to use those in cases where a percolating network is required [88-92].

2.1.2. Tethered Nanoparticle – Polymer Composites

Chemical treatment of nanoparticles with an excess of molecular species, such as silanes, which are able to react with and passivate the surface groups, is a widely practiced method that facilitates dispersion of nanoparticles in polymers [93-95]. Treatment of silica particles with trimethoxyphenylsilane has for example been shown to lead to replacement of the hydroxyl groups with phenylsilane groups, thus rendering good dispersions when mixed with polystyrene, at least in the case when the particles are smaller than the polymer chains [96]. An even more versatile approach is to functionalize the particles with long chains that completely prevent particle–particle contacts and bridging by reaction of surface groups. Recent experimental as well as theoretical works have considerably advanced our understanding of these systems and provide important guidance for how the components ought to be selected to control dispersion state of particles in polymers. Much of this understanding is based on ideas about polymer mixing and "wetting" derived from theories for planar brushes [97-100]. The interdigitation or wetting of polymer chains tethered to particles by a host polymer increases the overall available configurational space for both polymers, and thereby favors dispersion. As the available surface for tethered–host polymer contacts increases in proportion to the distance from the center of a sphere, the high curvature of nanoparticles is intuitively expected to impact these physics and to favor dispersion. This expectation is confirmed by a variety of recent studies that have characterized phase stability of nanocomposites using a range of analytical techniques including

electron and optical microscopy, small angle X–ray scattering, and mechanical rheometry [39, 41, 94, 101-112].

Remarkably, irrespective of the particle and polymer chemistries used, results from these studies can be summarized in a simple phase diagram as shown in Figure 4a, which underscores the important role of polymer–polymer contacts and wetting. The solid and dashed lines in the figure denote the wet to dry brush transition and the complete expulsion of host chains in planar brushes, respectively [100]. The most striking feature of this phase diagram is the enhanced stability towards phase separation that is observed across almost all the studies wherein phase separation is observed when the ratio (P/N) of the degree of polymerization of the host polymer, P, to that of the particle–tethered polymer, N, is around 5, irrespective of the particle chemistry, polymer size, and polymer chemistry. This enhanced stability in comparison to planar brushes, where phase separation occurs at $P/N \leq 1$ [100], is attributed to the strong particle curvature that provides for enhanced configurational freedom for the tethered chains, as depicted in the Figure 4b. These experimental findings have been accompanied by extensive theoretical and simulation efforts [113-120] that have largely confirmed the increased degree of chain interpenetration owing to particle curvature, thus leading to the strong deviations from planar brushes. Lastly, is should be noted that polydispersity in tethered polymer size further enhances the degree of interpenetration and thus can positively contribute towards the improved phase stability [120, 121]. These effects are also influenced by particle shape. Phase stability of rod–shaped tethered nanoparticle–polymer composites were in fact recently reported to exhibit better than expected dispersion stability [91, 122, 123]. As with spherical particles, critical P/N value for phase separation increased with decreasing particle size. We anticipate that subtle effects of shape on particle curvature will lead to enhanced dispersion in nanocomposites based on particles with

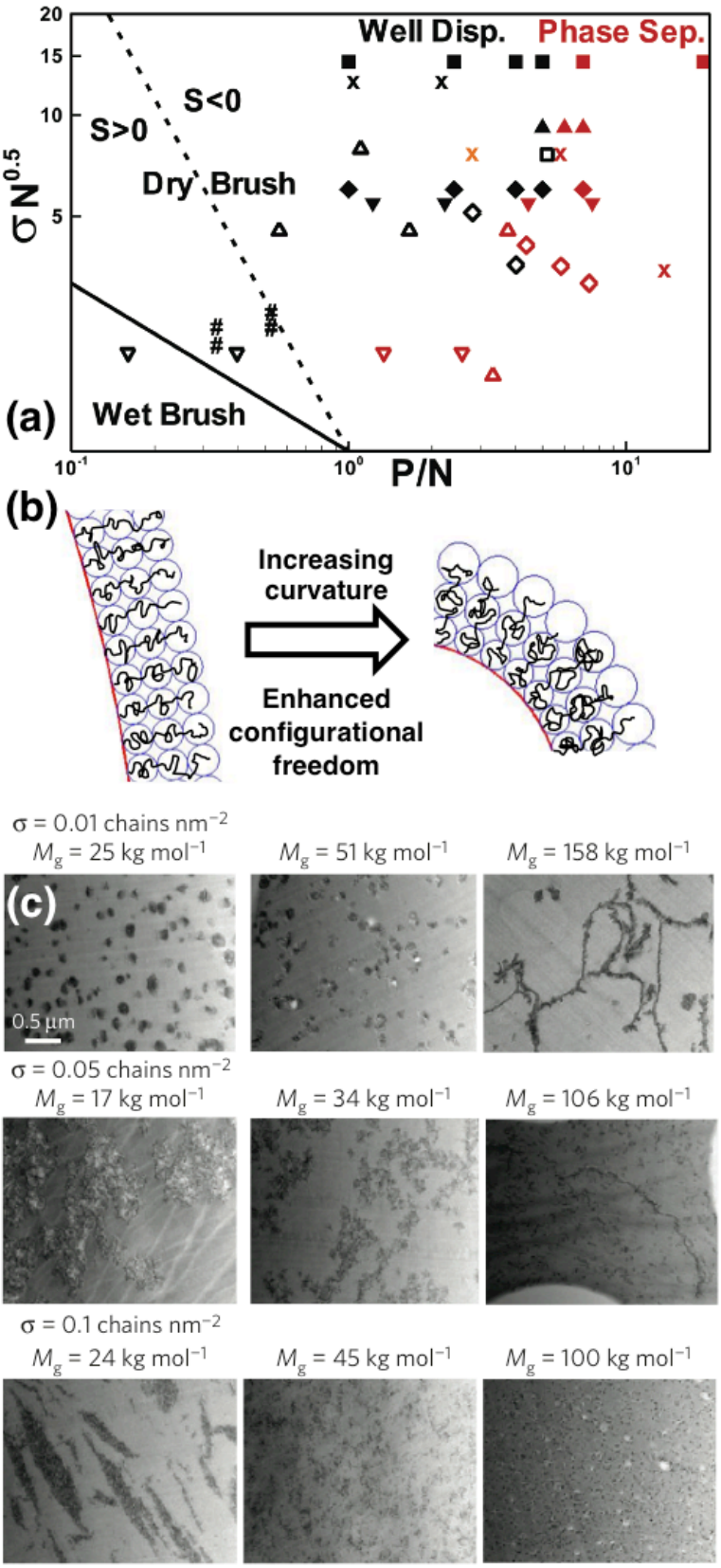
Well Disp.
Phase Sep.
S<0
S>0
Dry Brush
Wet Brush
(a)
σN^0.5
P/N
(b)
Increasing curvature
Enhanced configurational freedom
σ = 0.01 chains nm^-2
M_g = 25 kg mol^-1
M_g = 51 kg mol^-1
M_g = 158 kg mol^-1
(c)
0.5 μm
σ = 0.05 chains nm^-2
M_g = 17 kg mol^-1
M_g = 34 kg mol^-1
M_g = 106 kg mol^-1
σ = 0.1 chains nm^-2
M_g = 24 kg mol^-1
M_g = 45 kg mol^-1
M_g = 100 kg mol^-1

Figure 4 a. General phase diagram for tethered nanoparticles polymeric composites. Different symbols correspond to different studies. Reprinted (adapted) with permission from S. Srivastava, P. Agarwal, L. A. Archer, Langmuir 2012, 28, 6276. Copyright 2012 American Chemical Society. **b.** Schematic depicting enhanced configurational freedom of tethered polymer chains with increasing curvature. The blue circles denote the configurational space available to the tethered chains (black lines). **c.** Electron micrographs showing the range of self–assembled nanoparticle structures progressively going from spherical clusters to thick sheets, thin sheets, strings and finally well–dispersed particles with increasing grafting density and molecular weight of tethered chains (M_g). The matrix homopolymer is 142 kg mol^{-1}. Reprinted by permission from Macmillan Publishers Ltd: P. Akcora, H. Liu, S. K. Kumar, J. Moll, Y. Li, B. C. Benicewicz, L. S. Schadler, D. Acehan, A. Z. Panagiotopoulos, V. Pryamitsyn, V. Ganesan, J. Ilavsky, P. Thiyagarajan, R. H. Colby, J. F. Douglas, Nature Mater. 2009, 8, 354, copyright 2009.

anisotropic shapes including ellipsoids, discs, and tubes. Because of the lower percolation threshold, such studies are more delicate and careful studies of these geometries are just beginning to appear [91, 122, 123].

Entropic effects imparted to nanocomposites by a polymeric host or particle–tethered polymer, or sometimes both, can not only be used to facilitate dispersion, but may also be used to impart "intelligence" to the morphologies particles achieve. Interactions between immiscible polymer blocks in copolymers have, for example, been extensively studied as a means of producing directed assemblies of particles in polymers [124-142]. An even more promising route for achieving anisotropic assembly of particles was demonstrated by Kumar and coworkers, which employs partial coverage of the particle surface to allow for a competition between the entropic (tether–melt and tether–tether) and enthalpic (core–core and core–melt) interactions, leading to an array of nanoparticle structures including nanoparticle strings, sheets and spherical aggregates, as shown in Figure 4c [41, 114, 143, 144].

Another approach exploits the surface migratory tendencies of these tethered nanoparticles to synthesize composite thin films with nanoparticles decorating the free surfaces [93, 145, 146]. Akin to the migration of star polymers towards the interface in a mixture of star and linear polymers [147], the lower surface tension of the tethered chains leads to a systematic migration of the tethered nanoparticle towards the free surfaces. However, increasing nanoparticle curvature leads to more homogenous dispersions, and careful tuning of the particle size and tether length is required to achieve the desirable assembly at the free surface while maintaining partial phase stability [93, 146]. All of these effects can be enhanced using external fields, particularly those that can selectively impart body forces on the particles. For example, a magnetic field has also been utilized as an *external handle* to drive the anisotropic assembly of

tethered nanoparticle with magnetic cores, and the resulting nanocomposites have been shown to exhibit anisotropic material properties [112, 148].

The tethered nanoparticle approach outlined above, however, relies purely on entropic forces to achieve good dispersions, which means that although it is guaranteed to work for a broad range of polymer and particle chemistries, the restrictions on host polymer or tethered polymer molecular weight can easily run counter to the needs of an application. For instance, bare nanoparticles are largely preferred for applications owing to their ease of processability and ready access to all of the surface sites. In actual practice, however, uniform dispersions are only achieved when favorable interactions between the particles and the host polymer chains overcome the interparticle interactions. In this case, a physically adsorbed polymer layer on the particle surface provides the stabilization. A scaling theory proposed by deGennes [149] assumes that an adsorbed chain molecule at a neutral surface forms a self–similar carpet constituted by chains in a *loop–train–tail* configuration, in which interactions between polymer segments in the train and the surface anchors the adsorbed chain. If the interaction energy between a single segment of the chain and the surface is $\varepsilon k_B T$, it can be shown that for a polymer chain of degree of polymerization N in thermodynamic equilibrium at the surface, there are on average $\varepsilon^{-5/2}$ segments in the train [150]. This means that even when the interactions between the adsorbed chains and the surface are considered weak (i.e. $\varepsilon < 1$), the greater number of segments in each train will provide a zipper–like reinforcing effect that may produce strong–enough anchoring that, but for dynamic exchange between segments in the loops and train, the physically adsorbed chain is qualitatively identical to a surface–grafted polymer. The scaling theory predicts that in the case of ideal chains, the number of loops per chain scale as $\sqrt{N}$, meaning that the effective degree of polymerization of the tethered polymer is $N - \sqrt{N}$. And, for moderate to large

molecular weight polymers, the average thickness of the surface layer is approximately the random–coil radius, R_g, of the polymer; a conclusion that has been verified by experimental and theoretical studies of polymer adsorption on a neutral, flat surface [151, 152].

Thus, the criterion $P/N < 5$ for obtaining well dispersed polymer–grafted nanoparticles is automatically satisfied for practically any polymer length. In particular, $N/\left(N-\sqrt{N}\right)<5$ is satisfied for any polymer larger than monomers (*Kuhn*) long! It is noteworthy that nanoparticle curvature plays an extremely important role in stabilization of particles even with adsorbed polymer chains; the condition of $P/N < 1$ is never met as the dangling end is always smaller than the free polymer. Thus, enthalpic interactions lead to formation of effectively tethered nanoparticles, which in turn are stabilized through entropic forces. Another case where entropy is understood to stabilize the nanoparticle dispersions is when bare or surface protected nanoparticles are dispersed in polymers larger than the size of the nanoparticle itself [35, 55-57, 96, 153-157]. These stable dispersions also manifest unusual deviations from expected material properties for nanocomposites. Specifically, the viscosity of the nanocomposite is found to be lower than that of the host polymer [55-57, 154, 155]. The stability of the nanocomposite obtained in such situations is universally agreed [35] and has been shown to preserve over a large range of particle loadings [35, 96]. However, the origins of the phase stability and the reduction in viscosity produced upon dispersion of nanoparticles in a polymer host continue to be a subject of considerable debate in the field [96] [153]. This strategy is then of perhaps obvious significance for applications, where particles are required to play an active role and high loadings are typically preferred.

As will be discussed in later sections, a small content of extremely large polymer chains have been shown to effectively preserve the structural integrity of polymer–particle composites

containing as high as 90 wt% active particles. Polyvinyldine fluoride (PVDF), for example, has functioned as a workhorse *binder* polymer in lithium battery electrodes where it typically acts to hold particles together, forms homogenous composites with two or more active particle chemistries, and anchors the highly filled dispersion to a macroscopic current collector. Although we believe that similar entropic factors are at work in ensuring predictable material structure, mechanical properties, and repeatable function in the highly filled polymer–particle composites used for battery electrodes, systematic investigations of the phase stability and quality of dispersion in these composite electrodes have so–far not been given high priority in the field. The desire to use less expensive solvents, such as water, lower amounts–, or even no binder in electrode formulations will fuel activity in this area. Likewise, we predict that the trend towards commercial deployment of energy storage technologies based on carefully designed nanoparticles, will fuel research activity into the coating behavior and rheology of dispersions of these small particles in high molecular weight polymers.

Entropic destabilization beyond P/N of 5 can also be completely circumvented by tethering a polymer on the nanoparticle surface that interacts strongly with the host polymer chains. In this situation enthalpic gains by tethered–host polymer interactions can overcome the entropic costs associated with dispersing particles. Good dispersions might be achieved irrespective of the size and chemistry of the melt chains and up to extremely high particle loadings, as long as the interaction parameter between the tethered and the host polymer is negative. A few notable examples from the literature demonstrate the importance of this concept. PEO tethered gold nanorods have been reported to be stable in poly(methyl methacrylate) hosts ($\chi \sim -0.65$) at least up to P/N of 64 [158]; polystyrene tethered gold nanorods have also been shown to form stable in poly(2,6–dimethyl–p–phenylene oxide) (PPO) hosts ($\chi \sim -0.12$) at least up to P/N of 30 [159];

and poly(styrene–r–acrylonitrile) tethered silica nanoparticles are stable in poly(methyl methacrylate) hosts ($\chi \sim -0.15$) at least up to P/N of 580 [160]. More importantly, because the enthalpic contribution to the free energy increases in proportion to the total number of interacting segments, there is no reason to believe that any of these tethered nanoparticles will destabilize in even higher molecular weight polymer hosts than those used in the literature reports. In the extreme case, the groups tethered on the nanoparticle surface can be made a part of the host polymer backbone itself, thus removing any scope of particle aggregation and leading to completely dispersed nanocomposites [161]. Tethered nanoparticles thus allow for a facile route to synthesize well–dispersed nanoparticle–polymer composites wherein the entropic as well as the enthalpic stabilizing forces can be tuned through adjustment of the various parameters including the graft chain length, grafting density and interactions with the host chains.

2.1.3. Single–Component Nanocomposites

In all of the above examples, the polymer–tethered particles are dispersed in a host polymer to create a nanocomposite material. An intriguing recent departure from this theme is the creation of so–called self–suspended nanoparticle systems or single–component nanocomposites in which the entire nanocomposite material is created from short–polymer–tethered nanoparticle building blocks. Each building block (Figure 5a) of the material is itself a nanocomposite, and thus it is possible to control the dispersion state, structure and properties in the materials in an analogous fashion to how atomic building blocks might be used to create molecules with distinct features. An implicit advantage of such systems is that because the suspended (nanoparticle cores) and suspending phases (polymer matrix) are one and the same, material properties can be controlled precisely through the tethered polymer molecular weight, chemistry, and grafting density at the particle surface [40, 42, 45-47, 162-166]. Physical properties in these self–suspended

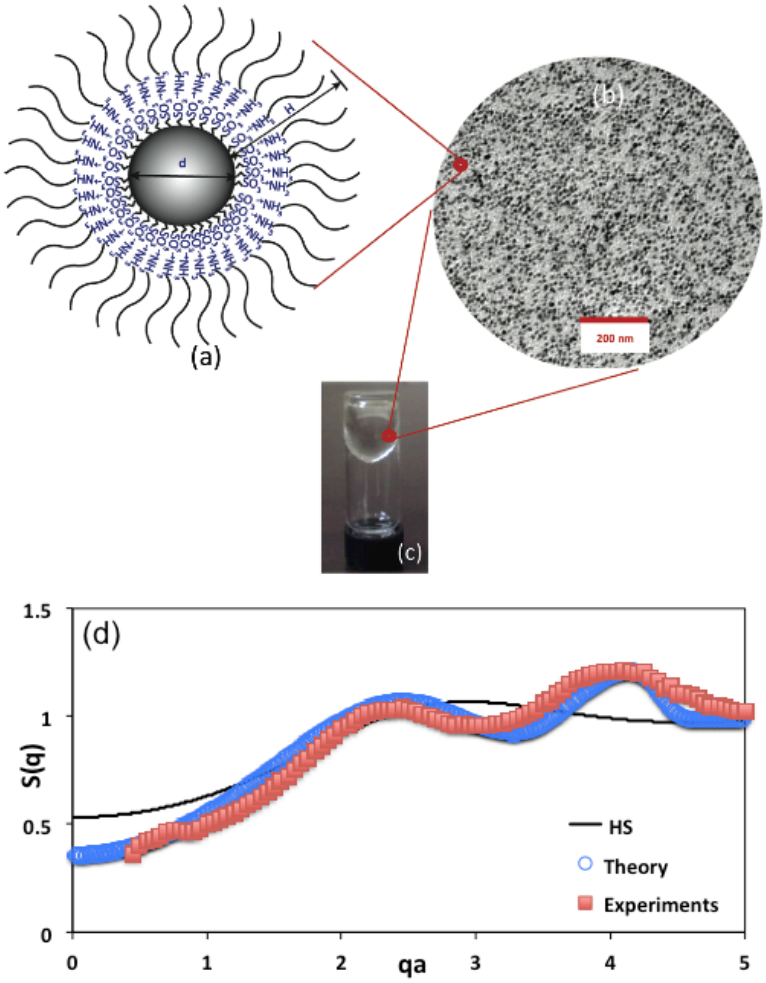

Figure 5 a. PEG chain tethered to silica nanoparticle by ionic linkage between sulfonic acid and amine groups. **b.** TEM micrograph of NIMs. **c.** Upturned vial showing NIMs flow as neat, homogeneous liquids. Reprinted (adapted) with permission from P. Agarwal, H. Qi, L. A. Archer, Nano Lett. 2010, 10, 111. Copyright 2011 American Chemical Society. **d.** Comparison between structure factors $S(q)$ from experiments, theory and hard sphere (HS) suspensions. Particle volume fraction is 8.5% in all cases.

nanoparticle fluids can also be engineered through physical and chemical changes performed on the tethered polymer (e.g. molecular weight, grafting density, architecture, and chemistry) and particle (size, shape, chemistry, mass distribution (e.g. hollow, rattles, etc.)) components. For appropriate grafting density and tether length, the tethered polymer fluidizes the nanoparticle cores and the materials exist as a liquid–like disordered phase [167, 168], as depicted in the micrograph in Figure 5b, in the absence of a suspending solvent. These single component nanocomposites may also flow like a liquid under gravity at room temperature, as shown in Figure 5c [42].

Although still in its initial stages, research on these so–called Nanoscale Organic Hybrid Materials (NOHMs) reveal behaviors that clearly show that despite their physical similarity to colloidal suspensions and star–branched polymers, comprised of individual macromolecular branches each linked by one end to a point–like, mobile constraint, these analogies are at best facile. For instance, like polymers, self–suspended poly(ethylene glycol)–tethered silica (SiO_2–PEG) and poly(isoprene)–tethered silica (SiO_2–PEG) particles have been reported to exhibit simple Newtonian flow behavior on long time–scales [42] and chain relaxation on intermediate timescales [46]. However, in contrast to star polymers, the relative viscosity decreases as the tethered polymer (suspending fluid) molecular weight is increased at fixed grafting density. Also, unlike star polymers, for which the relaxation time of the arms become exponentially slower as the molecular weight rises [169, 170], relaxation dynamics of the tethered chains in NOHMs are slowest for the lowest molecular weight chains. Likewise, whereas NOHMs, in analogy to colloidal suspensions, can be made to undergo a liquid to disordered glass/jamming transition by increasing the fraction of space occupied by the nanoparticle cores [42, 53, 171], and can be unjammed and processed by application of a force, unlike particle suspensions, they can also be

jammed by increasing temperature [172]. NOHMs differ from colloidal suspensions most fundamentally in their low–wave–number (q) scattering (Figure 5d). Specifically, whereas the structure factor $S(q)$ for colloidal suspensions reaches a composition–dependent plateau value at low q, $S(q \rightarrow 0)$ is much smaller. This arises from the space filling constraint imposed on the polymer chains, and leads to minimal compressibility and depressed scattering at low angles [47, 173]. Figure 5d shows a comparison of the structure factor profiles from experiments, from a theory developed by Yu and Koch for NOHMs [174], as well as from calculations for a hard sphere suspension model. These space filling constraints have also been shown to lead to lower relative diffusivities of the polymer–tethered nanoparticles in comparison with the bare nanoparticle composites, as revealed by MD simulations [173].

Self–suspended nanoscale hybrid materials are interesting for applications due to their high degree of tailorability. As the organic ligand is covalently linked to the nanoparticle core, one is no longer constrained by chemistry that may favor phase separation. In addition, the system presents a variety of handles that may be tuned to achieve the specific properties desired for in a particular type of application. For example, the tethered polymer matrix crystallinity or amorphicity may be altered by changes in the chain length and grafting density. Changes in the ligand chemistry will affect the interaction with foreign species, including ions [52-54, 175] and small gas molecules. Some of these features have been already exploited in novel particle–based fluids for selectively capturing CO_2 [48-51]. More remarkable shape–memory features have been achieved by cross–linking the particle–tethered chains to create networks in which the nanoparticles form the netpoints [176, 177]. Likewise, changes to the nanoparticle core chemistry can create systems that are magnetically or optically responsive [178, 179] or which function as efficient lubricants [180, 181]. Self–suspended nanocomposites based on densely

grafted ionic liquids [182-185] and those with both oligomeric chains and molecular species [54, 186] have also been demonstrated as attractive candidates for electrolytes. Recent studies discussed later in the review show that one might also pyrolyze the organic corona to inexpensively produce carbon–based composites with electronically connected cores.

2.2. Mechanical Properties of Nanocomposite Materials

Enhancing the mechanical properties of polymers while maintaining their ease of processing is high among the many motivations for adding nanoscopic fillers into polymer matrices [2, 30, 187]. Up to a thousand–fold increase in the modulus of low–cost, commodity polymers can be achieved upon addition of layered silicates [187]. Physical properties of these systems are, unfortunately, quite difficulty to tune and their structure hard to control; they have largely been replaced by nanoparticle polymer composites that permit greater tunability as they offer greater access to equilibrium particle morphologies. A key empirical result is that optimal mechanical reinforcement of a host polymer melt is achieved at or near the onset of percolation of particles to form interconnected network–like structures. As discussed in Section 3 and 4 of the review, interconnected structures formed by percolated particles can be used to advantage for enhancing ion and electron transport in polymers, and as such is a significant driver for the increasing use of nanocomposites as electrolytes and electrodes in energy storage applications. The route to achieving a percolated structure and the extent of mechanical reinforcement depends sensitively on dispersion state of the nanoparticles and interactions among the nanoparticles and with their polymer host.

Percolation or connectedness has been associated with sharp transitions to a solid–like mechanical response in nanocomposites subjected to low–frequency mechanical deformations (see Figure 6). It is achieved with relative ease in cases when spherical aggregates of bare or

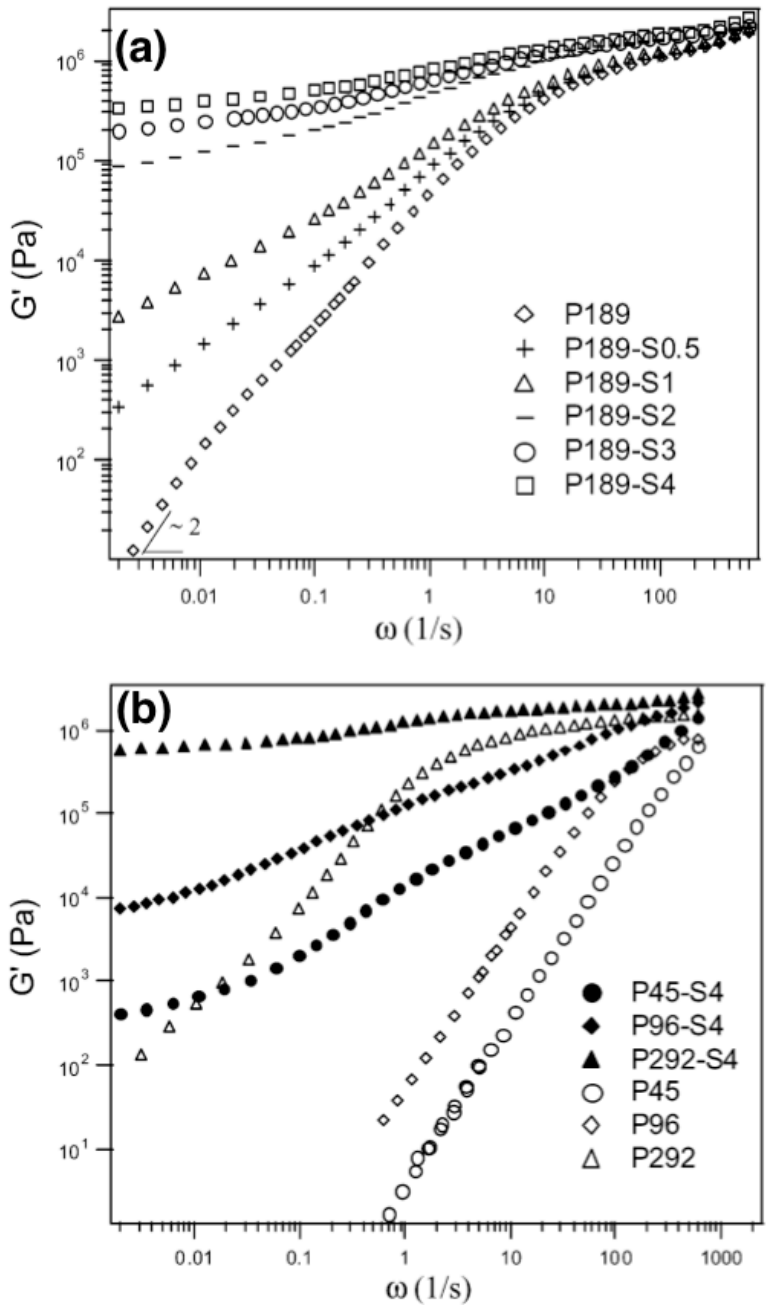

Figure 6 Frequency–dependent storage modulus of PEO/silica nanocomposites with a. fixed PEO molecular weight and different particle volume fractions and with b. fixed particle volume fraction and different PEO molecular weights. Reprinted (adapted) with permission from Q. Zhang, L. A. Archer, Langmuir 2002, 18, 10435. Copyright 2002 American Chemical Society.

sparsely tethered nanoparticles are formed in the polymer matrix [32, 34, 102, 111, 143, 144, 148, 188-190], and even more easily in cases of anisotropic assembly (strings or sheets) [143, 144, 148]. The property enhancement is understandably larger for anisotropic particles owing to better connectedness between the nanoparticle structures [143, 144]. Although these effects are most commonly reported for nanocomposites comprised of bare particles in a host polymer, they are also evident in cases where polymer grafted particles are used; wherein tethered chains facilitate connections between sparsely tethered nanoparticles in an analogous manner to the role spontaneously adsorbed melt chains in aiding particle connectedness in bare nanoparticle–polymer composites. Stronger reinforcement is observed in cases when either longer tethered chains are present, leading to greater entanglements with the neighboring chains [144] or when the nanoparticle surface interaction with the host chain is stronger and the host chains are larger, leading to stronger adsorption, more entanglements and even bridging of chains between particles [32, 188].

Because the network structure in a nanocomposite melt is maintained by particle–particle contacts and friction, nanocomposites based on polymer grafted particles exhibit substantially lower levels of reinforcement at comparable particle loadings to those based on bare or sparsely grafted particles, and require much higher particle loadings to provide comparable levels of mechanical reinforcement. These behaviors are consistent with expectations for the jamming transition in soft colloidal systems and the critical particle loading is, as expected, directly related to the particle softness and the extent of swelling of the tethered polymer by the melt [43, 191]. What has been described as the non–intuitive observations of larger moduli for composites with smaller molecular weight polymer melts [191] are also readily understood based on these same physics.

The optimal conditions required for maximum nanoparticle reinforcement of a polymer host differs significantly for nanocomposites based on melts versus glassy polymer hosts. In the former, the percolated nanoparticle network is the primary load bearing entity in the limit of zero mechanical deformation rates because, unlike the host polymer, which can relax to equilibrium on such long timescales to relieve an applied load, the particle network cannot. The point of failure/yielding of the nanocomposite is then associated with the rearrangement/mechanical degradation of the percolated structures, which has been reported to occur at strains of $O(1)$ for the particle network [34, 143, 144, 189, 190]. The situation is very different in the case of glassy polymers, where the polymer host is frozen on long timescales and the host itself dictates the point of material failure. Maximal reinforcement therefore occurs in a glassy host in which the polymer matrix interacts maximally with the particles, i.e. well–dispersed particles facilitate reinforcement [43, 52, 53, 105, 191, 192].

A less understood phenomenon is the *negative reinforcement* some particles produce in high molar mass polymers. As was mentioned in the previous section, particles with sizes smaller than the random coil size of the polymer melt are found to disperse uniformly in the host and lower both the viscosity and rubbery plateau moduli of the host polymer [35, 55-57, 96, 153-157]. This so–called *non–Einsteinian* mechanical behavior was first observed by Mackay and coworkers for polystyrene particles in polystyrene melts [55], and have been subsequently observed in a variety of combinations of host polymer and bare as well as tethered nanoparticles, including magnetite [57] and fullerene [57] nanoparticles in polystyrene hosts, silsesquioxane–polymer composites [157] and tethered silica–polymer composites [154]. Research in this important area is in its infancy, and the physics responsible for these observations are complex. Recent direct measurements of the polymer and particle dynamics suggest that polymer chain segments near

the ends may function as plasticizer for the host and thus compete with more typical reinforcing effects nanoparticles have on polymers [154].

CHAPTER 3

TETHERED NANOPARTICLE−POLYMER COMPOSITES: PHASE STABILITY AND CURVATURE

Adapted with permission from

S. Srivastava, P. Agarwal, and L. A. Archer, Tethered Nanoparticle−Polymer Composites: Phase Stability and Curvature. *Langmuir* **28**, 4097 (2012).

Abstract

Phase behavior of poly(ethylene glycol) (PEG) tethered silica nanoparticles dispersed in PEG hosts is investigated using small–angle X–ray scattering. Phase separation in dispersions of densely grafted nanoparticles is found to display strikingly different small–angle X–ray scattering signatures in comparison to phase–separated composites comprised of bare or sparsely grafted nanoparticles. A general diagram for the dispersion state and phase stability of polymer tethered nanoparticle−polymer composites incorporating results from this as well as various other contemporary studies is presented. We show that in the range of moderate to high grafting densities the dispersion state of nanoparticles in composites is largely insensitive to the grafting density of the tethered chains and chemistry of the polymer host. Instead, the ratio of the particle diameter to the size of the tethered chain and the ratio of the molecular weights of the host and tethered polymer chains (P/N) are shown to play a dominant role. Additionally, we find that well–functionalized nanoparticles form stable dispersions in their polymer host beyond the P/N limit that demarcates the wetting/dewetting transition in polymer brushes on flat substrates interacting with polymer melts. A general strategy for achieving uniform nanoparticle dispersion in polymers is proposed.

3.1. Introduction

This Chapter reports the phase behavior of polymer tethered nanoparticles dispersed in polymeric hosts and aim to define general guidelines for achieving functional nanocomposites comprised of uniform dispersions of sticky nanostructures in polymers. We also report a methodology that relies on small–angle X–ray scattering (SAXS) experiments to reliably deduce the dispersion state of polymer–grafted nanostructures in polymeric hosts. Our efforts are motivated by the large body of experimental and theoretical work, which show that depletion attraction and van der Waals forces invariably conspire to promote irreversible aggregation of nanoparticles in polymeric hosts [1, 193, 194]. This behavior runs counter to the needs of most technological applications, which seek to control nanoparticle dispersion in the host in order to simultaneously take advantage of the facile processability of polymers and the exceptional range of functionalities (e.g., electrical and ionic conductivity, ability to reversibly intercalate metal ions in battery electrodes, high refractive index, large magnetic susceptibility, large mechanical moduli, high thermal conductivity, etc.) that can be as facilely achieved with inorganic nanostructures [1, 52, 53, 193, 195, 196].

Sterically stabilizing particles with an attached polymer coating is a common method for controlling interparticle interactions and thereby the dispersion state in colloidal dispersions [194]. Such entropy–driven stabilization of nanoparticles has distinct advantages over electrostatic stabilization because of its relative insensitivity to the solution environment (presence of electrolytes, aqueous/nonaqueous environment) and concentration of particles [194]. Numerous experimental [36, 39, 41, 82, 101-105, 110, 191, 197-203] as well as theoretical [113-118] studies have appeared over the past few years that address the structure and phase stability, glass transition [101] and rheology [36, 39, 82, 102, 110, 191, 199] of tethered

nanoparticle−polymer composites. It has been shown that by tuning the size, grafting density, and chemistry of the tethered polymer, composite systems ranging from uniform dispersions of repulsive nanoparticles in a host [101, 102] to self–assemblies of anisotropically interacting nanostructures can be achieved [41, 197, 198]. Polymer tethered nanoparticle systems have consequently attracted significant recent attention for a wide variety of applications, including functional materials [204], energy generation and storage [52-54, 205] drug delivery [206, 207] and organic electronics, where control of the dispersion state of particles in a host polymer is required.

Recently, we reported a method for creating stable polymer–functionalized nanoparticles that exhibit complex fluid rheology, including a simple Newtonian flow regime, in the absence of a suspending medium [40, 42, 182]. The interactions between the nanoparticle cores in such self–suspended suspensions have also been studied using density functional theory [47]. A new entropic force, set by the requirement that the tethered polymers fill the intervening space between particles, was found to control the equilibrium structure of the particles and produces an equilibrium structure factor that vanishes in the limit of low scattering vectors. This means that these systems exhibit colloidal stability even in the absence of a polymer host (see Figure 7a), which makes them good model systems for understanding the role of entropic forces in stability of nanoparticle dispersions in polymers.

3.2. Experimental Methodology

Results reported in this article focus on silica (SiO_2) nanoparticles (diameter d = 10 ± 2 nm) functionalized with 5 KDa poly(ethylene glycol) (PEG) chains (Figure 7b) at grafting densities Σ (= σb_{Kuhn}^{-2}) ranging from 0.8 to 2 chains/nm^2. Here, σ and b_{Kuhn} correspond to the dimensionless grafting density and Kuhn step length of the polymer, respectively. The two–step chemistry

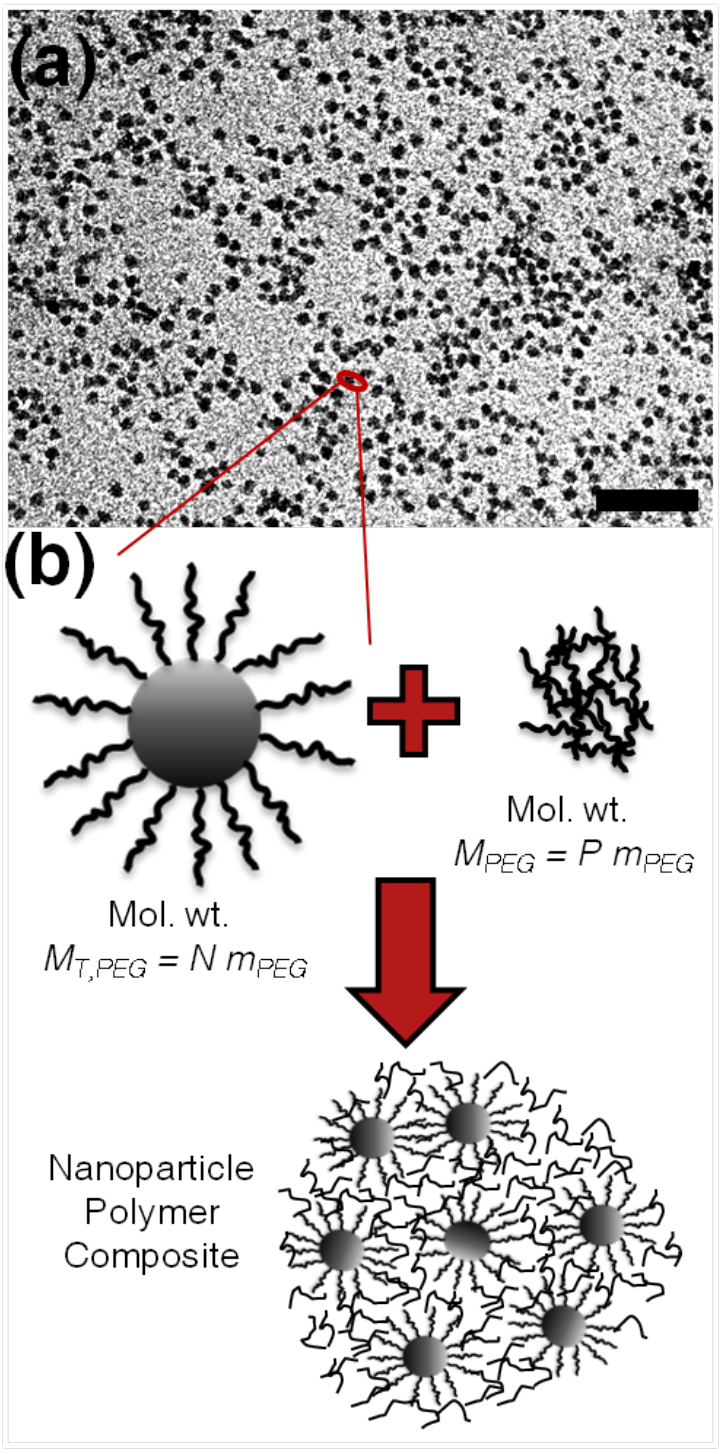

Figure 7 a. A TEM image showing well–dispersed PEG tethered nanoparticles with no external solvent (Σ = 0.8 chains nm^{-2}, $M_{T,PEG}$= 5000 Da). The scale bar is 100 nm. **b.** A schematic depicting the synthesis scheme.

employed in the synthesis allows for creation of densely grafted nanoparticles with precise control of the grafting density and tethered polymer molar mass, $M_{T,PEG} = Nm_{PEG}$, as well as the flexibility in the polymer and core chemistries that can be used [40, 42, 182]. Polymer−particle composites were synthesized by dispersing the PEG−SiO_2 nanoparticles at a fixed weight fraction, φ = 10%, in PEG hosts of varying molar masses ($M_{PEG} = Pm_{PEG}$), as shown in the schematic in Figure 7b. Here N, P, and m_{PEG} are respectively the degree of polymerization of the tethered chain, the degree of polymerization of the host chain, and repeat unit molar mass of the tethered/host chains. Following evaporation of the co–solvent, the PEG−SiO_2/PEG composites were annealed for at least 12 h at temperatures above the melting point of PEG to allow the system to reach equilibrium. By systematically varying the molecular weight of the host polymer and the grafting density, we find that it is possible to develop a comprehensive understanding of the phase behavior of particles in nanocomposites.

SAXS studies were carried out in–house using a benchtop SAXSess instrument (Anton Paar) with a block camera and line collimated X–ray beam at a wavelength of 0.1542 nm. All measurements were performed at 70°C using customized paste sample holders with kapton windows. Desmearing of the scattering data was performed by using the generalized indirect Fourier transformation (GIFT) method with a hard sphere structure factor model using the Percus−Yevick closure relation [208].

3.3. Results and Discussion

Figure 8 shows transmission electron micrographs (TEMs) of PEG−SiO_2/PEG nanocomposites with a range of P/N values from 1 to 19 and two different grafting densities. The nanocomposite with P/N ratio of 19 will be shown later to be phase separated; however, particle clustering is absent even in this case as evident from the images. Thus, application of the conventional

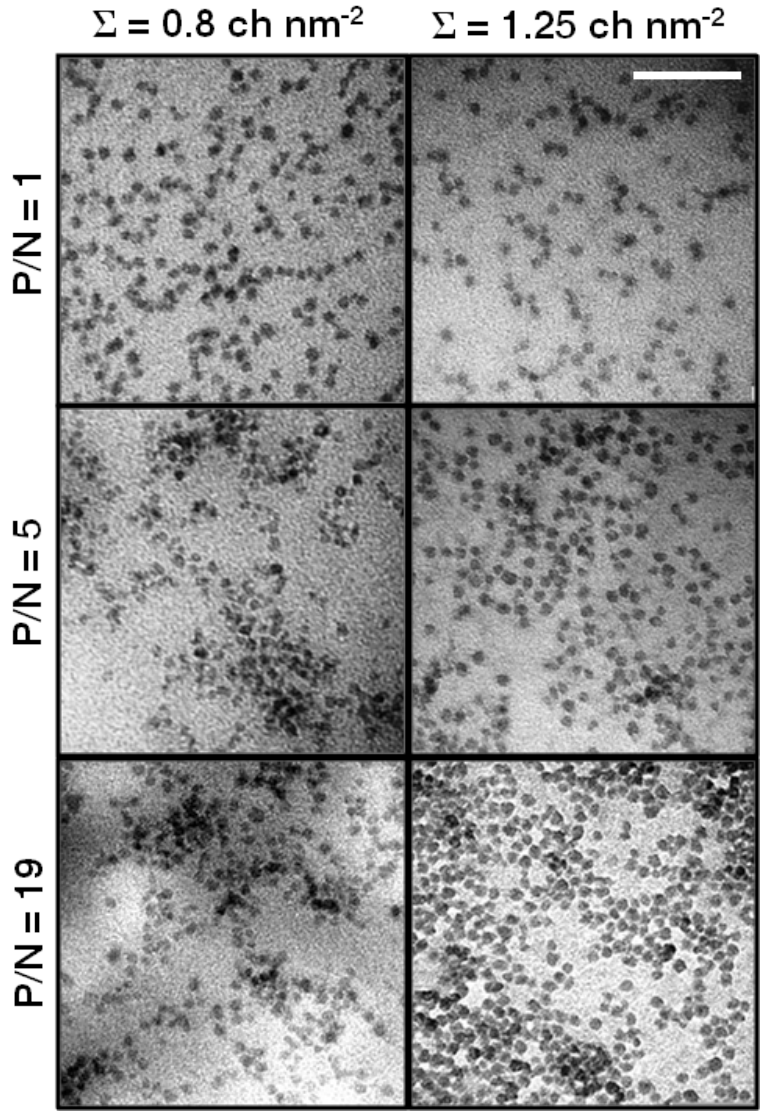

Figure 8 TEM images showing well dispersed PEG tethered nanoparticles of two different Σ in PEG hosts with varying P/N. The scale bar is 100 nm.

practice of associating agglomeration of nanoparticles with the advent of phase separation in polymer nanocomposites implies that, contrary to earlier studies [209, 210], all of the PEG−SiO_2/PEG nanocomposite systems are well dispersed. It is understood, however, that a strictly TEM–based analysis scheme is disadvantageous for characterizing dispersion of nanoparticles in polymers given that only a small volume of the material is interrogated, and additionally, the influence of various interfaces (nanocomposite−air and nanocomposite− carbon coated TEM grid) cannot be easily ruled out.

Small–angle X–ray scattering (SAXS), on the other hand, provides complementary, bulk information about the average interparticle spacing, which we will show provides a facile approach for characterizing the dispersion state of polymer– functionalized particles in polymeric hosts. Figure 9a shows the experimental data (open symbols) of the scattering intensity ($I(q)$) vs. the scattering vector (q) profile and the corresponding fits (solid lines) for two PEG−SiO_2/PEG systems with P/N ratios of 5 and 6, respectively. The scattering intensity can be expressed as the product of a form factor $P(q)$, which captures single particle characteristics, including shape and dimensions, and a structure factor $S(q)$, which contains information about particle−particle structure and interactions. Figure 9b shows the normalized $p(r)$ vs. r plots for the two nanocomposite systems in Figure 9a, where $p(r)$ is the pair distance distribution function (PDDF: $p(r) = 4\pi r^2 V_c \gamma_0(r)$), for an ensemble of particle scatterers and is related to $P(q)$ through a Fourier transform. Here, V_c is the volume of a single particle and $\gamma_0(r)$ is the probability of a point at distance r from a given point inside the particle. Consistent with the results from TEM analysis, the average radius of the particles is found to be around 6 nm.

The interparticle interactions are captured in the structure factor, which is related to the radial distribution function ($g(r)$) of the particles as

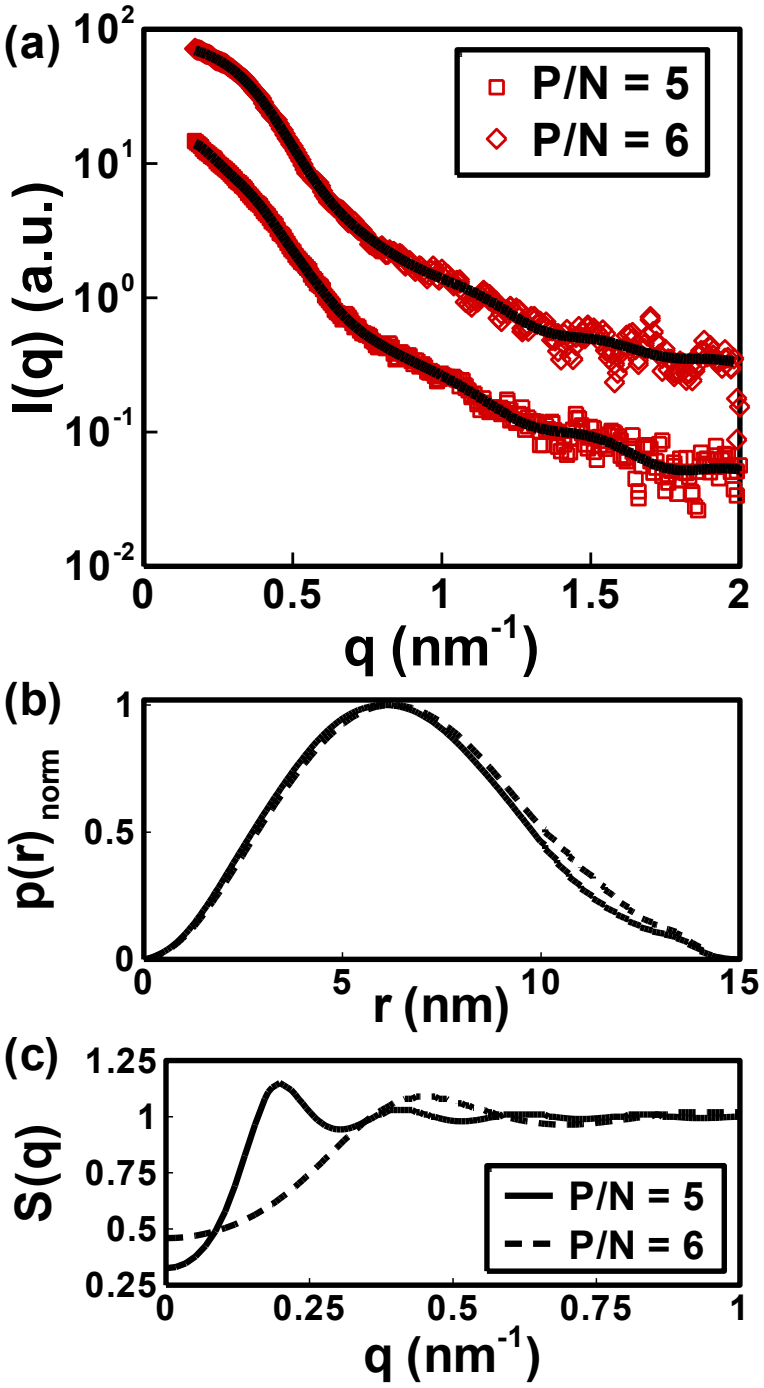

Figure 9 a. $I(q)$ vs. q for PEG NIMs (Σ = 1.25 chains nm^{-2}, $M_{T,PEG}$ = 5000 Da) suspended in PEG host (P/N = 5 and 6) at φ = 10%. Open symbols are experimental measurements and the solid lines denote the fits to the data. **b.** Normalized $p(r)$ vs. r and **c.** $S(q)$ vs. q for the same nanocomposites.

$$S(q) = 1 + \left(\frac{\phi}{V_c}\right)\int_0^{\infty} 4\pi r^2 \left(1 - g(r)\right)\frac{\sin qr}{qr} \quad (1)$$

and provides a direct measure of the average particle distribution in the scattering volume; ϕ is the core volume fraction. Figure 9c reports $S(q)$ vs. q for the two aforementioned nanocomposites. The position of the first peak (q_{max}) in these curves can be related to the average interparticle distance (d_{p-p}) as $d_{p-p} = 2\pi/q_{max}$. It is apparent from the figure that the structure factors for the two materials are qualitatively very different. For the nanocomposite with P/N = 5, d_{p-p} is around 32 nm, while the $d_{p-p} \sim$ 14 nm is significantly smaller for the nanocomposite with P/N = 6. Recalling that the average interparticle distance ($d_{p-p} = d(0.638(1 + (1/\varphi_{silica}-1)\rho_{silica}/\rho_{PEG}))^{1/3} \approx$ 35 nm) depends only on the weight fraction of the nanoparticles in a well–dispersed nanocomposite, such variation in d_{p-p} values should not be expected. Similar measurements on nanocomposites with varying grafting densities and P/N ratio were carried out, and the average interparticle distances are summarized in Figure 10. In all cases, d_{p-p} is found to be around 32 nm for $P/N \leq 5$, which is close to the aforementioned estimate. However, beyond $P/N \leq 6$, there is a sudden drop in d_{p-p}, and it is value approaches 12 nm, which is very close to d_{p-p} measured in the self–suspended SiO_2−PEG particles and shown as the dotted lines in the figure.

Therefore, it can be concluded that, irrespective of the value of the graft density σ, these densely grafted nanoparticles spontaneously phase separate into particle–rich domains where the particle spacing is much lesser than expected for well–dispersed nanoparticles. Even in the phase–separated state, however, the nanoparticles are well separated from each other due to steric stabilization from the densely grafted polymer layer. This feature of the materials is notable for other reasons: First, even in the phase–separated state, the dimensions of particle clusters

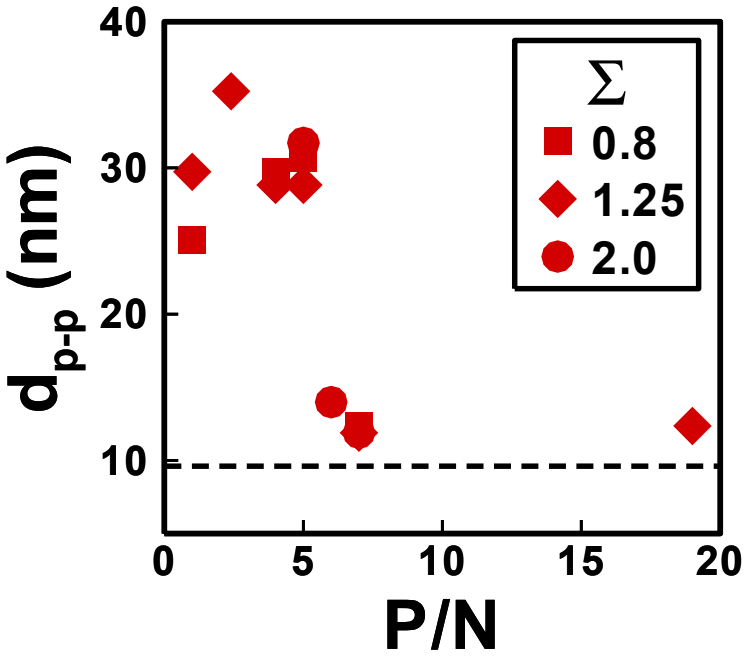

Figure 10 Inter–particle distance d_{p-p} vs. P/N for suspensions of NIMs with varying Σ and φ = 10%.

are bounded, implying that the typical sharp upturn in $I(q)$ at low scattering vectors seen in phase–separated nanoparticle−polymer composites is not observed [41, 102]. Second, it also means that screening of the attractive inter–core interactions by the tethered polymers will result in the phase separation having little if any noticeable effects on the spatial arrangements of particle cores visible from transmission electron microscopy measurements. Thus, electron microscopy cannot provide definite evidence for phase separation in such nanocomposites. A perhaps less obvious consequence is that short–range interactions that lead to strong enthalpic contributions to the system free energy are minimized, which makes our materials good model systems for studying the effects of entropic forces on nanoparticle/polymer phase behavior.

3.4. A Phase Diagram for Tethered Nanoparticle−Polymer Composites

Based on results obtained from SAXS experiments using SiO_2−PEG/PEG nanocomposites, a phase diagram for tethered nanoparticle−polymer composites is constructed as shown in Figure 11. To complete the map, we have also added results (open symbols) from several published studies that use other materials and methodologies for evaluating the state of dispersion of nanoparticles in polymers. To provide comparison with the theories for polymer brushes (degree of polymerization N, grafting density σ) tethered on flat substrates interacting with an external melt (degree of polymerization P), the scaling predictions for wetting−dewetting transition in such cases are shown as a solid line in the figure, which scales as $\sigma\sqrt{N} = (P/N)^{-0.5}$ and $\sigma\sqrt{N} = 1$ on the either side of $P/N = 1$ [100]. Also, the dashed line denotes the transition in the spreading coefficient (S), which scales as $\sigma\sqrt{N} = (P/N)^{-1.5}$ and corresponds to complete expulsion of the melt chains from the brush. In other words, a polymer brush on a flat substrate is completely phase separated from the melt in the region where $S < 0$. As evident from Figure 11, most nanocomposites lie well outside the theoretical wetting regime for flat brushes and, by these

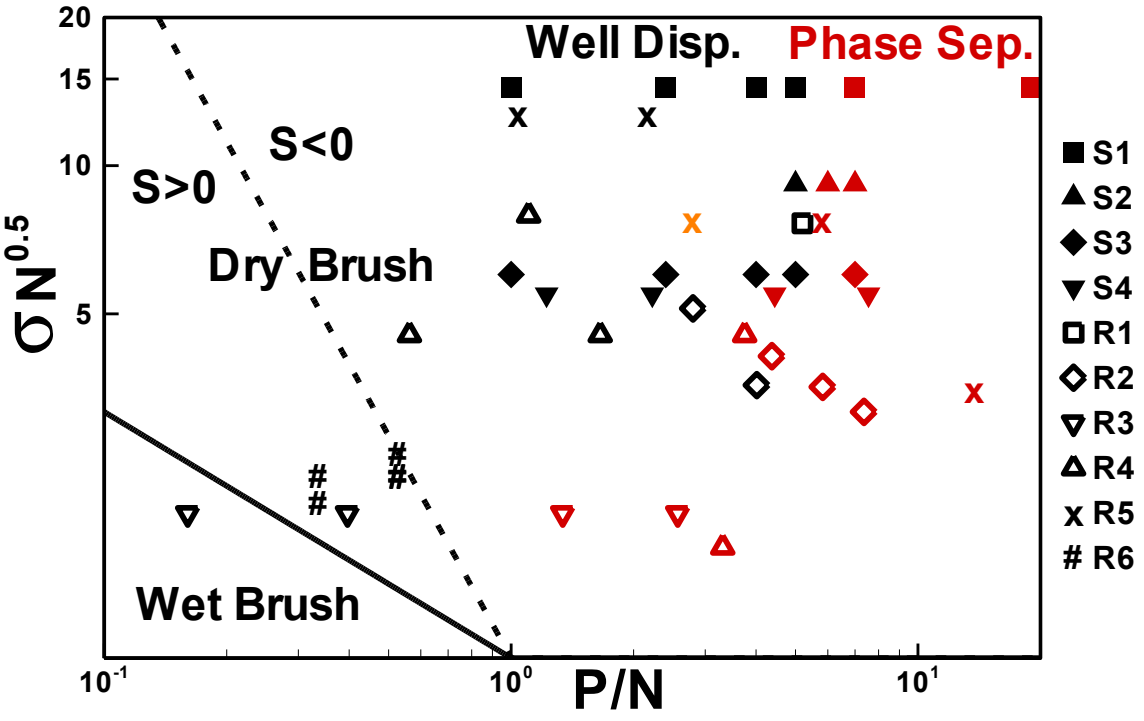

Figure 11 Phase diagram for suspensions of hairy nanoparticles in polymeric hosts. S1, S2 and S3 correspond to nanocomposites with $M_{T,PEG}$ = 5000 Da and Σ = 2.0, 1.25 and 0.8 chains nm^{-2}, respectively. S4 corresponds to nanocomposite with $M_{T,PEG}$ = 450 Da and Σ = 2.5 chains nm^{-2}. R1–R6 correspond to References [101], [102], [41], [103], [104] and [105], respectively. Black symbols represent well–dispersed systems, red symbols denote completely phase–separated systems and orange symbols denote partially phase–separated systems.

physics, should phase separate. However, it is apparent from the figure that well–dispersed systems are consistently observed, by us as well as others, even in the dry brush regime.

The apparent stability of these suspensions strongly points toward curvature effects playing an important role in the dispersion of these systems. Specifically, it is understood that the conformational space available for a chain tethered to a curved surface increases with the distance away from the tethering surface. This conformational freedom will be greatest near the free ends of the attached polymer brush, which should permit interpenetration of the tethered and host polymer chains (wet brush regime), even in cases when the tethered chain is strongly stretched and dry near the tethering surface. These effects are expected to become very prominent when the particle size (d) becomes comparable to the size of the tethered chain (R_g), i.e., $d/R_g \sim 1$. The scaling relations for brushes on flat substrates ($d/R_g \gg 1$), shown in Figure 11 as lines, have been argued to be applicable for curved surfaces by employing the Derjaguin approximation [36, 39, 119] but fail noticeably in the case of strong curvature, as considered here. In contrast, a few attempts have been made to modify the theories for star polymers ($d/R_g \ll 1$), but they correspond to the other extreme situation where the size of the core is negligible in comparison to the size of the corona [200, 202, 211, 212].

3.4.1. Comparisons with the Literature

Recent SCFT calculations [116] which take into account the aforementioned limitations of the flat−brush model, have studied the interpenetration length of nanoparticle tethered polymer brushes as a function of σ and P/N. Results from this study show a phase transition around a certain value of P/N that is largely independent of σ, which is consistent with results reported herein where the phase transition appears at P/N values between 5 and 6. At the same time, the observed critical value of P/N ($5 < P/N < 6$) for the systems studied here ($d/R_g \sim 3.7$) is

marginally higher than the value of 4 reported in a recent experimental study (represented by ◇ in Figure 11) [102] using SiO_2−polystyrene (PS)/PS composite systems with d/R_g larger than 4. The effect of d/R_g is also illustrated in data set S4 (filled ∇) in Figure 11, which was obtained a nanocomposite with $M_{T,PEG}$ = 450 Da, $d/R_g \sim 12$, and a comparable grafting density. S4 also exhibited phase separation at P/N slightly less than 5, which exemplifies the necessity to maintain a small d/R_g to obtain uniform dispersion of nanoparticles. Among the notable exceptions in the presented phase diagram are results from Ackora et al. [41] (∇), which show phase separation in PS systems at much lower P/N ratios accompanied by formation of a variety of morphologies; we ascribe these observations to the very low grafting densities of the polymer on the particles employed and its consequent inability to stabilize the particles from strong short–range surface forces. We likewise attribute the unexpected observations of phase separation in the well–grafted poly(methyl methacrylate) nanocomposite system studied by Xu et al. [104] (×) to longer range magnetic effects due to the cores; evidence for these effects can in fact be seen in the string–like morphologies observed in their systems.

3.5. Conclusions

In summary, we report on the phase behavior of tethered nanoparticle−polymer composites and find that the conditions required for stabilizing a densely tethered nanoparticle in a polymeric host are dependent only on the ratio of particle size to size of the tethered chain, d/R_g, and the ratio of the size of the host and the tethered chain, P/N, and are largely independent of σ and the polymer chemistry. Our observations suggest a few guidelines for dispersing nanoparticles in host polymers: (a) small nanoparticles, to minimize d/R_g and thus maximize curvature effects; (b) polymers tethered on the nanoparticle such that $N > P/5$; and (c) moderate to high grafting densities to ensure complete screening of attractive forces between the nanoparticles.

Additionally, contrary to popular practice in the literature, we find that neither electron microscopy nor the divergence of the intensity of X–rays scattered at small angles is sufficient to identify phase separation in nanocomposites employing well–grafted polymer chains. We show instead that the nearest–neighbor distance deduced from the interparticle structure factor provides a more reliable means for assessing the phase stability of nano– composite materials employing polymer–functionalized nano– structures. Finally, we find that well–grafted nanoparticles form more stable blends in polymer hosts than anticipated from theories based on force models computed for flat brushes. We suggest that the high curvature of nanoparticles facilitates interpenetration of particle–tethered chains by the free polymer chains in nanocomposites, which favors uniform mixing.

CHAPTER 4

STRUCTURE OF SELF–SUSPENDED AND OLIGOMER–SUSPENDED TETHERED NANOPARTICLE SUSPENSIONS

Partly adapted with permission from

S. Srivastava, L. A. Archer, and S. Narayanan, Structure and transport anomalies in soft colloids. *Physical Review Letters* **110**, 148302 (2013).

Abstract

SAXS investigation of nanoparticle arrangements and structure of self–suspended and oligomer–suspended tethered nanoparticles reveal unique features associated with both kinds of suspensions. Tethered nanoparticles with short tethers serve as model soft colloids and when suspended in oligomers exhibit properties ranging from hard sphere–like suspensions in the limit of low particle loadings to a structure anomaly typically associated with jammed materials interacting via soft interaction potentials. Self–suspended nanoparticles exhibit extremely homogenous nanoparticle distributions and long–range correlations among nanoparticles mediated by the tethered chains. The severity of the space filling constrain imposed on the tethered chains is also illustrated through comparison of the self–suspended nanoparticles with suspensions of these nanoparticles in a polymer matrix.

4.1. Introduction

Nanoparticle–organic hybrid materials contain inorganic nanocores surface functionalized by oligomeric chains. At sufficiently high grafting densities and length of the tethered polymer chains, the interparticle van der Waals interactions are completely screened and these tethered nanoparticles exhibit fluid like properties even in the absence of any external solvent [40, 42, 45, 46, 53, 162, 172]. These self–suspended nanoparticles can be viewed as incompressible single–component fluids and their structural properties have been well–described by a theoretical model of monodisperse hard cores, each of which is surrounded by its tethered fluid [47, 167, 168, 171, 173, 213].

In case of small, oligomeric tethered chains, the particles irreversibly agglomerate in the absence of an external solvent. Obtaining fluid like properties then necessitates addition of an external solvent. The properties of these tethered nanoparticle suspensions, obtained when the tethered nanoparticles are suspended in an oligomeric solvent, vary significantly upon changing the volume fraction of the nanoparticle in the suspensions. As will be discussed in subsequent chapters, the flow behavior of these suspensions can vary dramatically going from Newtonian fluids to soft glassy materials over small changes in the particle loadings.

In this chapter, we discuss the structure of tethered nanoparticles both in the presence and absence of an external solvent. Small angle X–ray scattering measurements were instrumental in obtaining the structure factor for the suspensions and reveal unique features in both the cases. The oligomer suspended nanoparticles exhibit a structure factor similar to hard sphere suspensions in the limit of low and moderate volume fractions, while at high volume fractions a maximum in inter–particle correlation is observed, which coincided with the point of jamming in these suspensions and is a direct manifestation of the soft repulsions between the nanoparticles.

At the same time, the self–suspended nanoparticles have long–range interparticle correlations, resulting in unique structure factors with stronger peaks and marked deviations from the corresponding hard sphere structure factors. Section 2 illustrates the experimental methodology followed for synthesis of both the self–suspended and oligomer–suspended nanoparticle suspensions and the SAXS measurements. This is followed by a discussion of the structural features observed in oligomer–suspended nanoparticles and self–suspended nanoparticles in section 3. The chapter ends with a conclusion of our findings in section 4.

4.2. Experimental Methodology

4.2.1. Synthesis of Tethered Nanoparticle – Oligomer Suspensions

Silane functionalized polyethylene glycol chains (PEG450, $M_{w,teth}$ ~ 450 g mol^{-1}, supplied by Gelest Inc.) were tethered to SiO_2 nanoparticles with diameters (d) of 10 nm, 16 nm and 24 nm (LUDOX^{TM} SM–30, HS–40 and TM–50; supplied by Sigma Aldrich) using the methodology reported earlier [32, 52, 53]. Schematics of the tethered PEG450–SiO_2 nanoparticle and the tethering chemistry are shown in Figure 12(a) and (b), respectively. PEG450–tethered nanoparticles were separated from the reaction mixture containing untethered chains by repeated precipitation using ethanol and n–hexane. Thermogravimetric analysis (TGA), carried out on an TA Instruments TGA Q500, of purified nanoparticles revealed an organic content of roughly 36, 26 and 14 wt% with increasing particle size; corresponding to grafting density of approximately 2.2 chains/nm^2, 2.1 chains/nm^2 and 1.6 chains/nm^2, respectively.

Suspensions of the nanoparticles were prepared by mixing appropriate amounts of nanoparticles with methoxy terminated Polyethylene Glycol (PEG, M_w ~ 550 g mol^{-1}, supplied by Sigma Aldrich) in a common solvent (chloroform) followed by removal of the solvent by heating for at least 12 h at 70^{o}C under vacuum, as shown in the schematic in Figure 12c. A range of such

PEG–SiO_2/PEG suspensions were made with weight fraction (φ) of tethered nanoparticles varying from 0.001 to 0.8. TGA was carried out on the suspensions to confirm complete removal of chloroform, as well as to determine the precise composition (φ_w) of the suspensions. The physical appearance of the suspensions varied from low viscosity liquids to high viscosity wax–like solids. The volume fraction of the nanoparticle cores (ϕ) in the suspensions was calculated from the measured φ_w and the ratio of densities of PEG to SiO_2, ρ, as $\phi = \rho\varphi_w/[1+ (\rho - 1)\varphi_w]$.

4.2.2. Synthesis of Self–Suspended Tethered Nanoparticles

The synthesis protocol followed here was similar to already reported procedures [42, 176]. Polyethylene glycol (PEG) chains were tethered on the surface of 10 nm silica (SiO_2) nanoparticles through a two–step process. In the first step, 3–(trihydroxysilyl) 1–propane sulfonic acid (Gelest Inc.) were mixed with SiO_2 nanoparticles (LUDOX^{TM} SM–30, Sigma Aldrich) in a 2:1 ratio by weight and allowed to react at a pH of 2 and 70^oC for 24 hours. The resulting aqueous suspension comprises of SiO_2 nanoparticles with 3–(trihydroxysilyl) 1–propane sulfonic acid tethered on the their surface through siloxane linkage (SiO_2–sulfonic acid) and untethered 3–(trihydroxysilyl) 1–propane sulfonic acid chains, which are removed by repeated dialysis. PEG tethered SiO_2 particles (PEG–SiO_2) samples with different grafting densities were synthesized by reacting the aqueous suspension of SiO_2–sulfonic acid particles in stoichiometric ratios with amino terminated polyethylene glycol methyl ether (PEG–NH_2, M_w = 5000 g/mol, PDI ~ 1.1, Polymer Source), followed by repeated precipitation with chloroform and hexane to remove even trace amounts of unreacted PEG–NH_2 chains. Polyisoprene (PI) tethered SiO_2 particles (PEG–SiO_2) samples with different grafting densities were synthesized by reacting the aqueous suspension of SiO_2–sulfonic acid particles in stoichiometric ratios with a solution of amino terminated polyisoprene (PI–NH_2, M_w = 5000 g/mol, PDI ~ 1.1) in

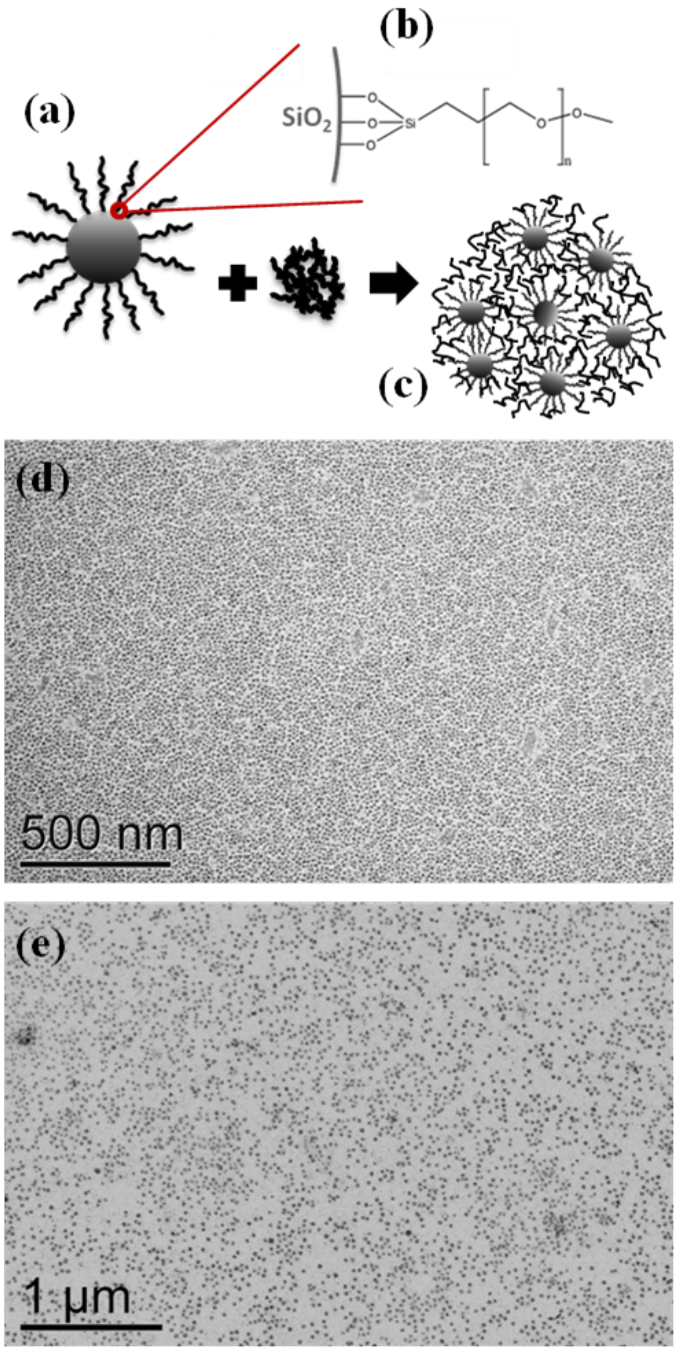

Figure 12 a–c. A schematic depicting the tethering chemistry and the synthesis scheme of the suspensions. **d and e.** Transmission electron micrographs of PEG–SiO_2/PEG suspension with d = 10 nm cores, ϕ_c = 0.15 and d = 24 nm cores, ϕ_c = 0.09.

tetrahydrofuran (THF), followed by repeated precipitation with chloroform and methanol to remove even trace amounts of unreacted PI–NH_2 chains.

4.2.3. Small Angle X–ray Scattering Measurements: Particle Size Distribution and Structure Factor Calculation

Small angle X–Ray scattering (SAXS) measurements were carried out at beamline 12–ID–B, sector 12, Advanced Photon Source at the Argonne National Laboratory. Measurements were carried out in custom–built sample holder at 70^{o}C using a point–collimated beam. The exposure times were limited to typically 0.5 seconds to minimize X–ray damage to the samples. In addition to the self–suspended and oligomer–suspended tethered nanoparticles, SAXS measurements were also carried out on a dilute aqueous suspension of PEG450 tethered nanoparticles and SiO_2–sulfonic acid particles using quartz capillary sample holders.

X–ray scattering intensity $I(q,\phi)$ for a suspension of particulate scatterers is known to depend on the scattering vector (q) and the particle volume fraction (ϕ) as

$$I(q,\phi) = \phi V_c \Delta\rho_e^2 P(q) S(q,\phi) \tag{2}$$

Here V_c, $\Delta\rho_e$, $P(q)$ and $S(q,\phi)$ represent the volume of a single particle, the difference in the electron density between the particle and the surrounding medium, the particle form factor and the inter–particle structure factor. The particle form factor depends only on the size and shape of the particles, and for spheres is given as

$$P(q) = \left[\frac{3(\sin qR - qR\cos qR)}{(qR)^3} \right]^2 \tag{3}$$

Here R is the radius of the spherical particle. The inter–particle structure factor for dilute suspensions in the absence of any inter–particle correlations is approximately 1, thus the

scattering patterns from a dilute suspension of spherical particles can be utilized to get the particle size as well as size distribution. SiO_2 particle size and size distribution were determined by fitting the scattering data from the dilute suspension of SiO_2–sulfonic acid particles using the size distribution technique included in the IRENA package for analyzing SAXS data [214].

Figure 13a shows the particle size distribution for SiO_2–sulfonic acid particles as the fraction of particles corresponding to a particular size, estimated in terms of both number fraction and volume fraction. As mentioned earlier, these size distribution estimates are calculated by maximum entropy method using the IRENA package [214]; the inset in the figure shows the experimental scattering intensity data for the dilute aqueous suspension of SiO_2–sulfonic acid and the fit obtained using the package. The size distribution based on particle volumes exhibits slightly larger particle sizes, which should be expected. It also reveals the presence of small amounts of particle doublets and a miniscule amount of particle triplets, which are absent in the size distribution based on particle number. These can be expected owing to the fact that some of the SiO_2–sulfonic acid particles might form doublets and triplets in the aqueous medium, which will subsequently break apart during the reaction with PEG–NH_2. The mean particle diameter (d_{mean}) and the standard deviation in particle diameter (σ_{dia}) were obtained by fitting the particle size distributions (f) with Gaussian function of the form

$$f = f_0 + A\exp-\left[\frac{\left(d - d_{mean}\right)^2}{2\sigma_{dia}^2}\right] \tag{4}$$

Here f_0 and A are arbitrary fitting parameters. The fits to both the distributions are shown in figure as black solid lines, and it can be clearly seen that the particle size is described fairly well by a Gaussian distribution. The parameters for the fit based on number fraction are (mean ± standard deviation): $d_{\text{mean}} = 9.416 \pm 0.019$ nm, $\sigma_{\text{dia}} = 2.034 \pm 0.020$ nm, $f_0 = 0.000 \pm 0.000$ and A

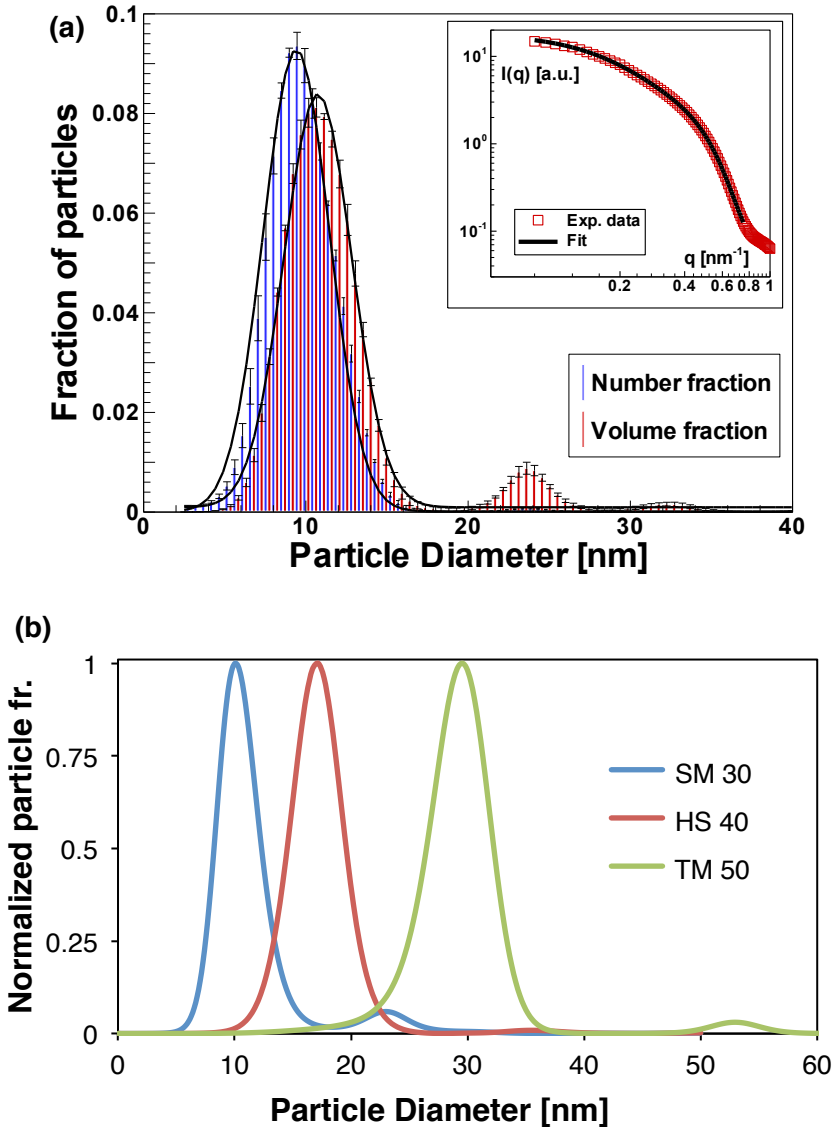

Figure 13 a. Size distribution function of the SiO_2–sulfonic acid particles as determined by SAXS shown as number fraction (blue) and volume fraction (red). The solid lines denote the Gaussian fits to the data. *Inset*: The experimental scattering intensities ($I(q)$ vs. q) for SiO_2–sulfonic acid particles (red symbols) and the fit to the data (black line). b. Normalized size distribution of nanoparticles in aqueous suspensions of PEG450–SiO_2 for three different particles sizes.

= 0.093 ± 0.001. The corresponding parameters for the volume fraction based fits are: d_{mean} = 10.738 ± 0.027 nm, σ_{dia} = 2.084 ± 0.029 nm, f_0 = 0.001 ± 0.000 and A = 0.083 ± 0.001. Thus for practical purposes, we can assume the particle diameter to be 10 ± 2 nm.

Particle size distribution for the PEG450–SiO_2 particles is also shown in Figure 13b. Similar to the results obtained for the SiO_2–sulfonic acid particles, the particles size distribution exhibits a primarily monomodal distribution, with a small population of doublets. The mean particle sizes for the LUDOX™ SM–30, HS–40 and TM–50 particles is obtained to be 9.8nm, 16.6 nm and 28.8 nm, which are in fair agreement with the particle sizes obtained from electron microscopy, which are 10 nm, 16 nm and 24 nm, respectively. The deviation in the two estimates of sizes for the largest particles can be ascribed to the restricted range of $P(q)$ accessible through the SAXS measurements.

The structure factor for concentrated suspensions or suspensions of correlated particles can be estimated by normalizing the scattering intensity data for the suspension ($I(q,\phi)$) with scattering intensity data for dilute suspension ($I_{dil}(q,\phi_{dil})$). Thus,

$$S(q,\phi) = \frac{I(q,\phi)}{I_{dil}(q,\phi_{dil})}\frac{\phi_{dil}}{\phi} \tag{5}$$

Here, ϕ_{dil} is the volume fraction of the particles in the dilute suspension. Alternatively, it is known that the structure factor for low volume fraction suspensions is approximately 1 for $qd \geq 10$. Thus, the value of ϕ_{dil}/ϕ can be estimated to be equal to the scaling factor required for normalizing the $I(q,\phi)$ and the $I_{dil}(q,\phi_{dil})$ data in the region near $qd \sim 20$. Figure 14 shows the scattering intensities for a self suspended PEG–SiO_2 particle system with ϕ_b = 0.085 as well as for the dilute aqueous suspension of SiO_2–sulfonic acid particles, as determined experimentally (filled diamonds) as well as the normalized scattering intensity (open diamonds) with the

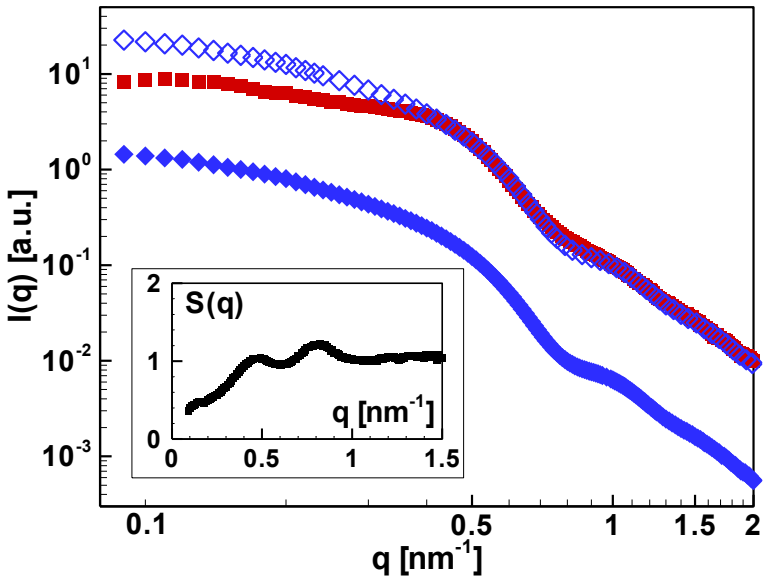

Figure 14 Scattering intensities ($I(q)$ vs. q) for SiO_2–PEG NOHMs (ϕ_b = 0.085, filled squares), SiO_2–sulfonic acid particles (filled diamonds) and the normalized scattering intensities for SiO_2–sulfonic acid particles (open diamonds). *Inset* shows the resultant structure factor for the ϕ_b = 0.085 SiO_2–PEG NOHMs ($S(q)$ vs. q).

normalization being carried out in the region $q > 20/d$. The resultant structure factor obtained by dividing the SiO_2–PEG NOHMs $I(q)$ with the scaled SiO_2–sulfonic acid $I(q)$ is shown in the inset of the same figure. Similar procedure was followed for all the other material systems as well.

4.3. Results and Discussion

4.3.1. Structure of the PEG–SiO_2/PEG Suspensions: Anomalous Structure

The theory of wetting/dewetting transitions in melt–polymer brushes on flat substrates has been shown to be conditionally applicable for tethered nanoparticle–polymer blend systems [39, 191, 201] and, as pointed out earlier, predicts phase separations for $\alpha > 1$. The PEG–SiO_2/PEG system used in the present study is comprised of 450 g mol^{-1} PEG tethered to SiO_2 dispersed in a 550 g mol^{-1} PEG host, thus $\alpha \sim 1.2$ and the systems are outside the stability range predicted by theory. However, recent experimental studies show that tethered nanoparticle–polymer systems can exhibit stability for $\alpha < 5$, attributing the enhanced stability to strong curvature effects that arise when the tethered chain and particle substrate are of comparable size [101, 102, 107, 113, 116]. Typical transmission electron micrographs (TEM) for the suspensions are illustrated in Figure 12d–e and the homogeneous distribution of primary particles apparent from the figure is consistent with a single–phase, stable fluid. Scattering intensity curves, $I(q)$ vs. q, for various d = 24 nm nanoparticle suspensions summarized in Figure 15 provide more rigorous confirmation of this point. There are various noteworthy features exhibited in these curves: (i) the $I(q)$ does not exhibit any upturn at the low q values and appears to attain a plateau for low volume fraction suspensions, directly indicating towards the absence of any large scale particle aggregates and decidedly points towards well–dispersed particles, (ii) appearance of a maximum in the intermediate q range with increasing ϕ, pointing towards the increasing contribution of interparticle correlations towards scattering with increasing ϕ, (iii) strong oscillation that are

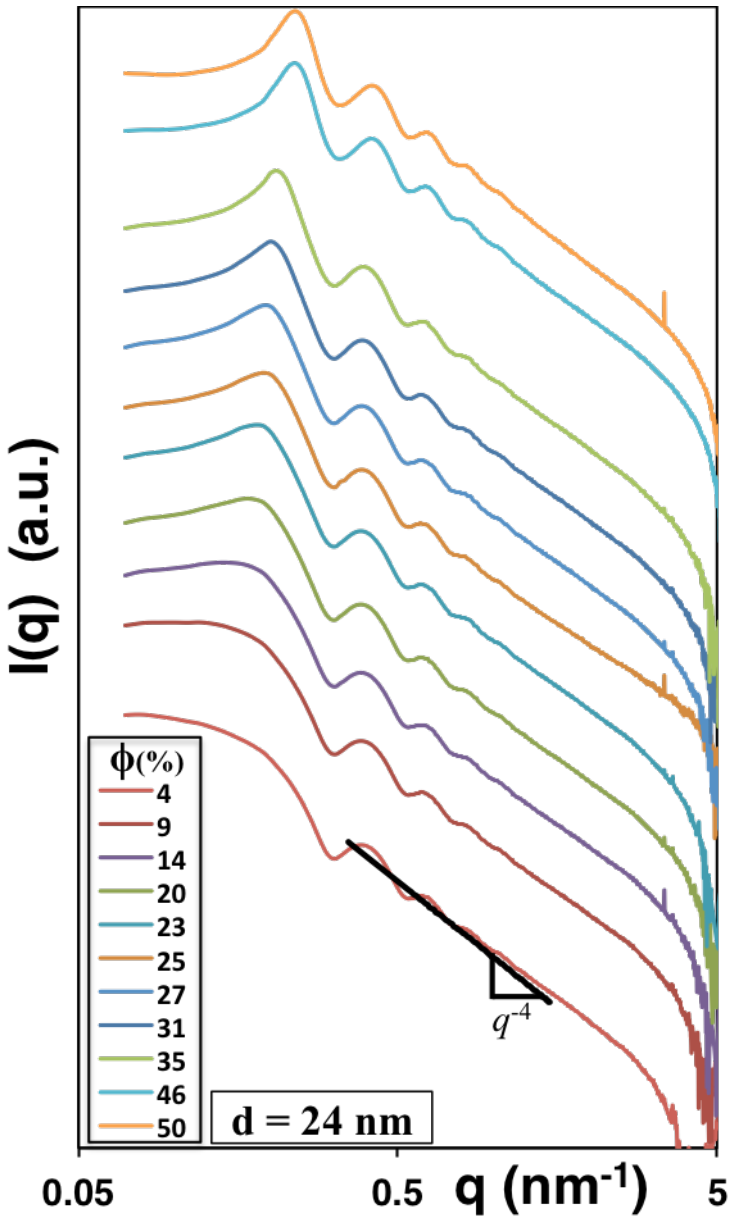

Figure 15 SAXS intensity profiles for suspensions of tethered nanoparticles in oligomers for different core volume fractions.

vestiges of the particle form factor damped out because of polydispersity effects in the large q region, and (iv) the q^{-4} scaling of the $I(q)$ in the large q region as indicated in the figure, pointing towards the scattering occurring from predominantly spherical objects.

The relation between these qualitative features and the structural properties of the suspensions are explored in Figure 16. Figure 16a and b report the evolution of the structure factor $S(q)\left(= I(q)/\lim_{\phi\to 0} I(q)\right)$ with increasing ϕ for suspensions comprising of SiO_2 core particle with diameters d = 10 nm and 24 nm. *S(q)* is the Fourier transform of the particle correlation function *g(r)* and the height of the first peak of the structure factor, S_1 is a direct experimental measure of the degree of nearest neighbor correlations among the scatterers. S_1 continuously increases with ϕ for a suspension of hard spheres until the jamming transition, however, it is evident from Figure 16a–c that S_1 exhibits a pronounced maximum at a specific, particle diameter dependent particle volume fraction $\phi = \phi_S(d)$ (as indicated by dashed lines in Figure 16c), indicating that particles become increasingly uncorrelated with increasing ϕ above ϕ_S.

The observed increase in S_1 for $\phi < \phi_S$ has been observed in a wide range of systems with soft interaction potentials, including a variety of soft colloidal systems [65, 215-225] and can be interpreted using standard arguments for hard–sphere suspensions. At low to moderate particle loading, particles explore the entire configurational space and minimize the overall system energy while managing to avoid energetically expensive overlaps, leading to enhanced particle–particle correlations as ϕ rises. In contrast to a system of hard sphere particles, however, the extra degrees of freedom associated with the particle softness facilitates introduction of new particles even beyond the onset of particle–particle contact at $\phi = \phi_S$, corresponding with the upturn in η (Figure 16c). Such particle accommodation doesn't necessarily enhance correlations between the particles and additionally, non–uniform compression of the flexible PEG oligomer corona

tethered to the particle cores leads to a progressive loss of correlation among particles with increasing ϕ.

The degree of homogeneity in these suspensions can also be estimated by observing the trends in S_0 ($=\lim_{q\to 0} S(q)$), which is related to the isothermal compressibility of a suspension. The minimum q achievable with the current instrument is 0.08 nm^{-1}, and we define *S(q)* at this value as S_m. Figure 16d shows that S_m continually decreases for $\phi < \phi_S$ and subsequently approaches a constant for $\phi \geq \phi_S$. The dashed lines in the figure are the expected trends for a suspension of hard spheres, and the trends in S_m as well as S_1 for suspensions of the PEG450–SiO_2 nanoparticles are evidently quite different from expectations for hard sphere suspensions. Notwithstanding these differences, the inter particle separation ($d_p = 2\pi/q_{S_1}$) is found to continually decreases with increasing ϕ and coincides fairly well with the theoretical estimates for a suspension of hard spheres, $d_p = d(0.63/\phi)^{1/3}$, as shown in Figure 16e with closed and open symbols, respectively. The SAXS data is found to be fairly consistent with the theoretical estimates and the power law coefficients from the fits to the data are found to be around –0.33 and –0.3, close to the theoretical value of –1/3. The d_p values drop from around 15 nm and 35 nm for the two suspensions and saturate around 10 nm and 25 nm, respectively, pointing towards the availability of large conformational space for the tethered chains in low ϕ_c suspensions, in contrast to the tight packing of the nanoparticles and highly compressed tethered chains in the high ϕ suspensions. This result also means that the anomalous reduction in particle–particle correlations beyond ϕ_S is not a result of large–scale variations in the particle arrangement but rather a manifestation of non–uniform particle deformation. Further discussion on these anomalous observations as well as the impact of non–uniform particle deformation on the relaxation dynamics of the suspensions will be undertaken in Chapter 8.

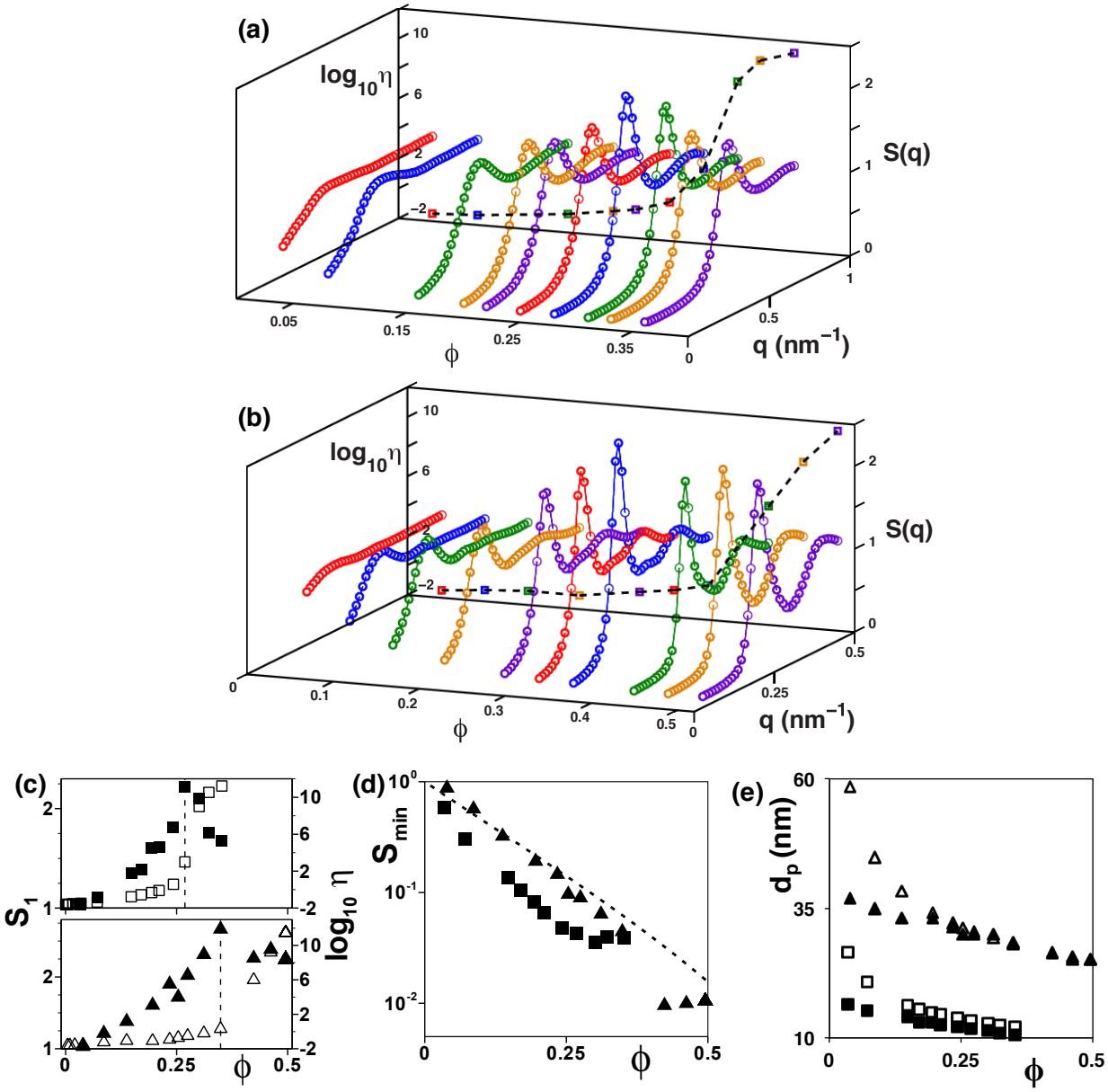

Figure 16 a. b. Structure factor *S(q)* and zero shear viscosity η vs. particle volume fraction ϕ, **c.** the maximum in *S(q)*, S_1 and η vs. ϕ (closed and open symbols, respectively), **d.** the minimum value of *S(q)*, S_m and **e.** the interparticle distance estimates d_p from SAXS and theory (closed and open symbols, respectively) vs. ϕ for suspensions with d = 10 nm (squares) and 24 nm (triangles) particles. In **a** and **b**, η vs. ϕ is depicted on the back panels. Dashed lines are a guide to the eye in **a** and **b**, denote the position of maxima in S_1 in **c** and S_m for hard sphere systems in **d**.

4.3.2. Structure of the Self–Suspended Nanoparticle Fluids

The single component self–suspended nanoparticle fluids can be considered to be a special case of the suspensions considered in the previous section in the limit of no external solvent being added to the nanoparticles. Such systems have been shown to exhibit fluid like behavior when the tethered chains are large enough to completely screen the interparticle interactions [42, 69, 172, 226]. However, the absence of an external solvent leads to strong correlation among the nanoparticle cores mediated by the tethered chains [47, 168]. The equilibrium arrangement of nanoparticles in such self–suspended nanoparticles is illustrated through the static structure factor $S(q)$ in Figure 17 for a representative set of the 5KDa PI–SiO_2 systems; $S(q)$ is a direct indicator of the degree of correlation among particle positions. In the absence of solvent, the tethered polymer chains must fill the interstitial space between the nanoparticle cores in a one–component fluid and are thus interdigitated and entropically frustrated [46]. The nanoparticle arrangement, as mediated by the tethered chains, is thus predicted to: (i) be significantly different from the corresponding arrangement for hard sphere suspensions (as shown in the inset), for which a molecular solvent fills the inter–particle space; (ii) be extremely homogenous, because all elements in the fluid are identical; and (iii) lead to significantly reduced values of $S(q)$ in the low q region, as expected in incompressible molecular fluids [47]. The increased degree of correlation among particles is expected to lead to higher primary and secondary peaks, although the primary peak is strongly masked in the present case by the rapid decline of the $S(q)$ in the low q region; it in fact appears as a slight shoulder in the smaller ϕ system. Finally, the results show temperature has at most a minimal effect on $S(q)$, indicating strongly that the arrangement of the nanoparticle cores are determined exclusively by entropy.

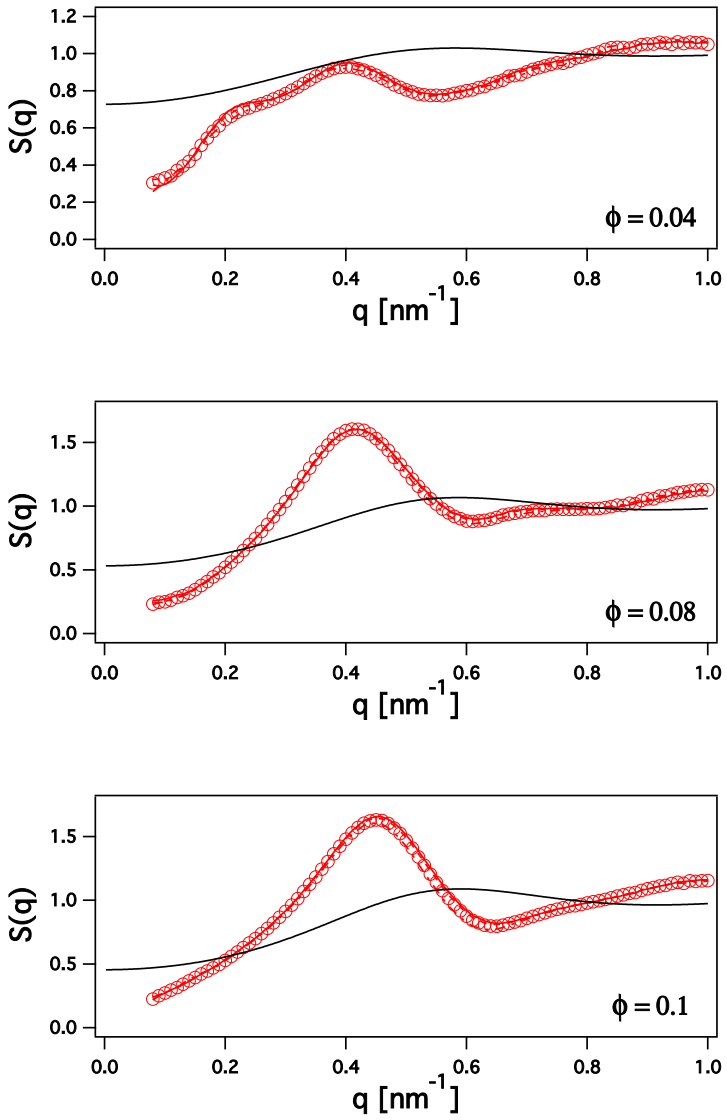

Figure 17 Structure factor $S(q)$ for various 5 KDa PI–SiO_2 self–suspended nanoparticle fluids with different particle loadings at T = 30°C (solid line), 50°C (dashed line), 70°C (symbols) and 100°C (dashed–dot line). The similarity of $S(q)$ across a range of T in each case points towards a completely temperature independent particle arrangement. The black solid line in each case represents the corresponding hard sphere structure factor.

The effect of the space–filling requirement imposed on the chains on the overall structure of the self–suspended nanoparticles is further illustrated in Figure 18, which depicts the trends in $S(q)$ upon addition of small amounts of free 2 KDa PEG in self–suspended 5KDa PEG–SiO_2. The self–suspended system, with $\phi = 0.088$, exhibits largest S_1 (height of the first maxima of $S(q)$) and smallest S_m (the minimum value of $S(q)$ in the limit of $q \sim 0$) and interparticle distance, d_p. This experimental setting is very similar to that described in the previous section on oligomer–suspended nanoparticles. However, a few key differences appear as discussed below.

Addition of free PEG chains into the self–suspended particles relaxes the space filling constraints imposed on the tethered chains and the effects of free PEG addition are evident even in the case of addition of 1 wt% free PEG. Significant changes in the values of both S_1 and S_m are observed even at addition of 1 wt% of free PEG, which corresponds to a change in ϕ from 0.088 to 0.087, and exhibit a monotonic decreasing and increasing trend with increasing free PEG component. These highlight the fact that addition of free PEG chains leads to a continual loss of correlation among nanoparticle cores and ever increasing compressibility of the suspensions, both of which indicate in turn that the nanoparticle arrangement becomes increasingly disordered with increasing free PEG content. At the same time, the interparticle distance d_p seems to decrease initially before increasing rapidly with increasing free PEG content. We expect that this initial decrease in d_p is an experimental artifact. Table 1 shows the corresponding ϕ values for each of the cases along with the expected interparticle distances and the experimental observations. All these observations are in accord with expectations for continuous dilution of a colloidal system. However, the structure factors for the self–suspended nanoparticles as well as the suspensions of these nanoparticles differ markedly from the corresponding hard sphere structure factors, as illustrated in Figure 19. These deviations are distinct in the low q behavior of $S(q)$ as well as the

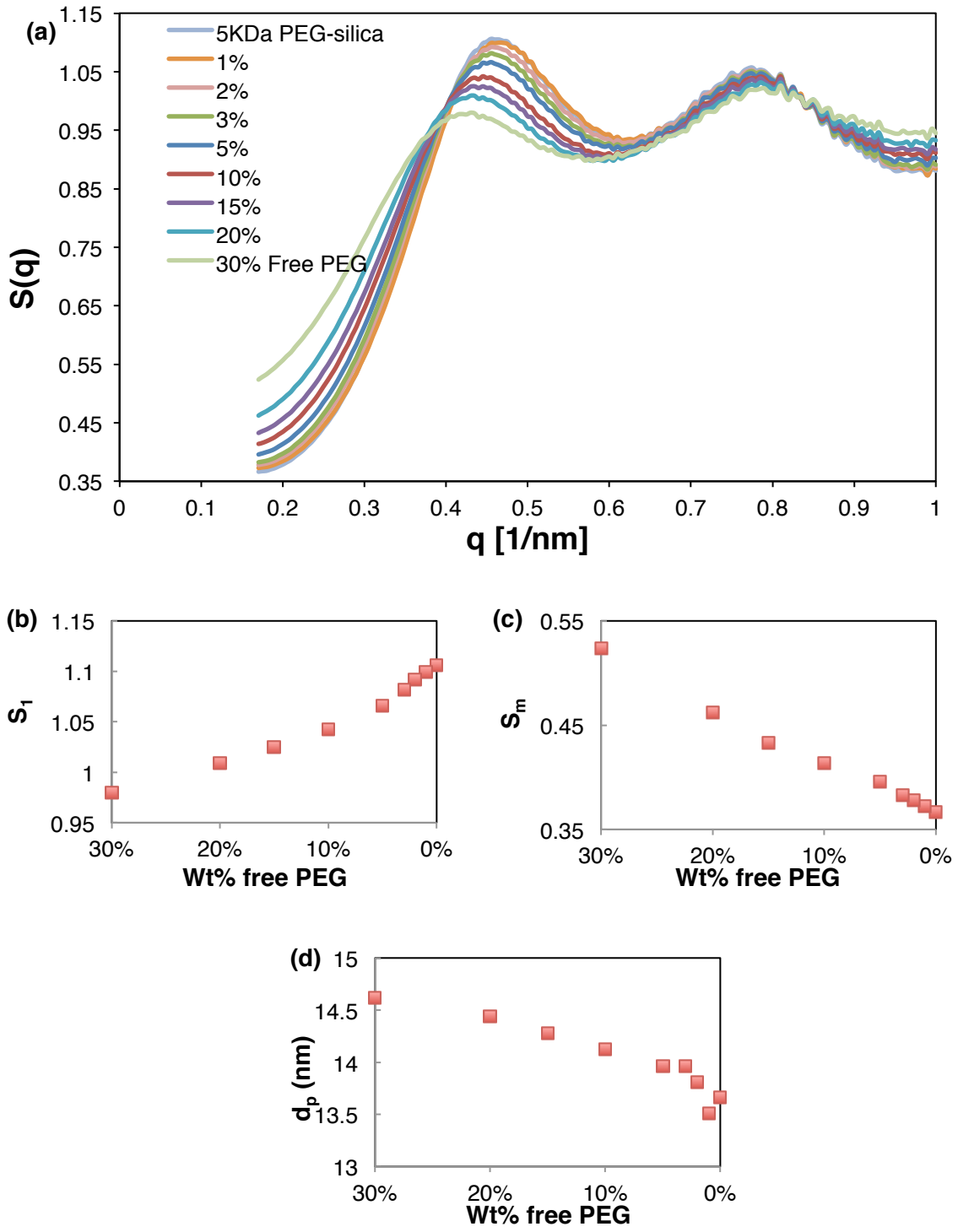

Figure 18 a. Structure factor evolution upon dilution of self–suspended PEG–SiO_2 nanoparticles with 2 KDa PEG. The % values indicate the wt% of free 2KDa PEG added in the suspension. **b – d.** Evolution of S_1, S_m and d_p with increasing amount of 2KDa PEG.

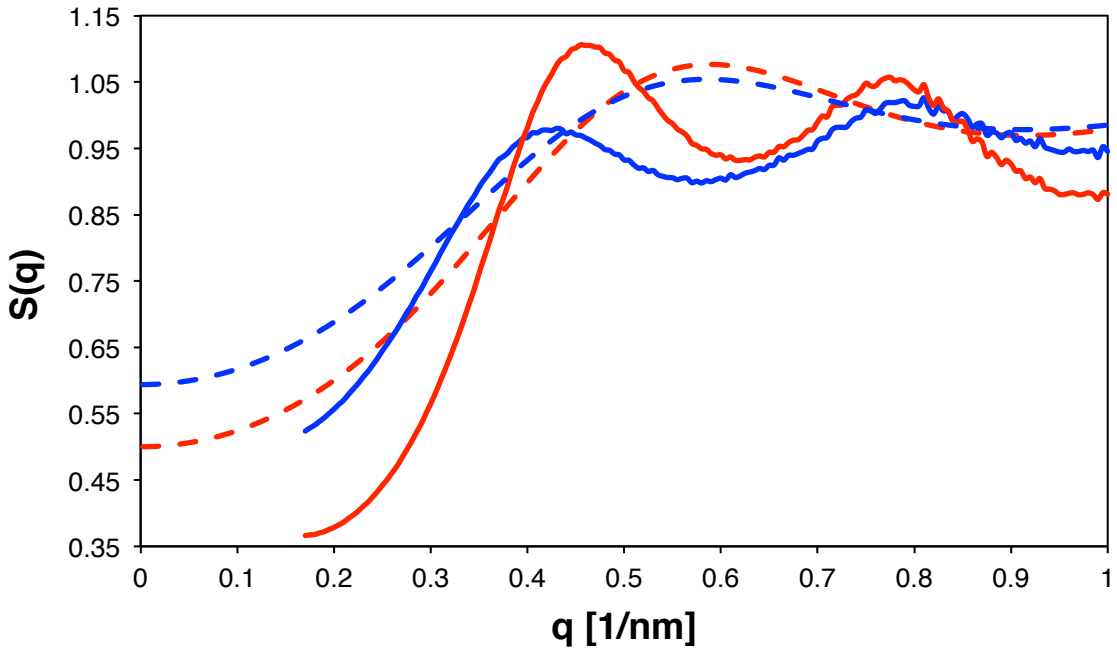

Figure 19 Comparison of the structure factor $S(q)$ for the self–suspended PEG–SiO_2 nanoparticles (ϕ = 0.088, red line) and self–suspended PEG–SiO_2 nanoparticles with 30 wt% 2KDa PEG (ϕ = 0.066, blue line). The dashed lines denote the corresponding hard sphere structure factors.

Table 1: Volume fractions and interparticle distances for 5 KDa PEG–SiO_2 self–suspended nanoparticles and its suspensions in 2 KDa PEG.

Wt% 2KDa PEG added to 5KDa PEG–SiO_2	**Particle volume fr. ϕ**	**Interparticle distance estimates from theory [nm]**	**Interparticle distance estimates from SAXS [nm]**
0	0.088	19.36	13.66
1	0.087	19.43	13.51
2	0.086	19.50	13.81
3	0.085	19.57	13.96
5	0.083	19.71	13.96
10	0.079	20.04	14.12
15	0.076	20.36	14.28
20	0.072	20.68	14.44
30	0.066	21.27	14.61

position of the primary peaks, even in the case of 30 wt% dilution by 2 KDa PEG (blue lines), and strongly point towards the fact that tethered chains in self–suspended nanoparticle fluids are under severe constraints arising from the space filling requirements imposed on the chains, and in turn strongly affect the inter–particle correlations and homogenize the particle distribution. Interestingly, in contrast to the oligomer–suspended nanoparticles, no evidence of a structural anomaly is observed in this case, which may be ascribed to the fact that the entropic gains associated with disordered nanoparticle arrangements are not too strong to lead to asymmetric compression/extensions of the tethered polymers the self–suspended systems.

4.4. Conclusions

The results presented in this chapter on the structure of tethered nanoparticle–polymer composites in the limit of well–dispersed nanoparticles unveil distinctive features associated with these tethered nanoparticles. Nanoparticles with short tethers act as soft nano–colloids with completely screened inter–particle interactions, and exhibit a loss in inter–particle correlations upon the jamming transition. This anomalous trend has been observed in other similar systems and is ascribed to a non–uniform deformation of the polymer tethers. These non–uniform deformation and subsequent loss in particle correlation also manifests as faster relaxation dynamics in these systems upon the glass transition, and will be a topic of discussion in chapter 7. Self–suspended nanoparticles display properties at the other end of the spectrum wherein the particles are strongly correlated despite a complete screening of the inter–particle van der Waals interactions. The space filling requirement imposed on the tethered chains can be directly associated with these unusual features through a comparison of the structure observed in these systems with corresponding hard sphere systems. Further, a moderation of these constraints is found to manifest as significant changes in the nanoparticle arrangements.

CHAPTER 5

RHEOLOGY OF NANOPARTICLE–POLYMER SUSPENSIONS

Adapted with permission from

S. Srivastava, J. H. Shin, and L. A. Archer, Structure and rheology of nanoparticle–polymer suspensions. *Soft Matter* **8**, 4097 (2012).

Abstract

Flow behavior of oligomer–tethered nanoparticles suspended in low molecular weight polymeric host is investigated at various particle sizes and loadings. Strong curvature effects introduced by the small size of the nanoparticle cores are found to be important for understanding the rheology of the materials. At high particle loadings, the stabilizing oligomer brush is significantly compressed and produces jamming in these suspensions. The jamming transition is accompanied by what appears to be a unique evolution in the transient suspension rheology, along with large increments in the zero–shear, Newtonian viscosity. The linear and nonlinear flow responses of the jammed suspensions are discussed in the framework of the Soft Glassy Rheology (SGR) model, which is shown to predict many features that are consistent with experimental observations, including a two–step relaxation following flow cessation and a facile method for determining the shear–thinning coefficient from linear viscoelastic measurements. Finally, we show that the small sizes of the particles have a significant effect on inter–particle interactions and rheology, leading to stronger deviations from expectations based on planar brushes and hard–sphere suspension theories. In particular, we find that in the high volume fraction limit,

tethered nanoparticles interact in their host polymer through short–range forces, which are more analogous to those between soft particles than between spherical polymer brushes.

5.1. Introduction

Well–controlled dispersions of nanoparticle additives in polymer hosts can be used to impart unique mechanical, electrical, and optical properties to the host. Such nanoparticle–polymer composites are promising materials targets for applications in diverse fields, ranging from electronics, computing, data storage and communications to energy storage, environmental remediation, and defense [1, 53, 195, 196]. Achieving uniform dispersions of stable nanoparticles in polymers is advantageous in many of these applications and methodologies for promoting particle dispersion are of longstanding scientific and technological interest [1, 32, 53, 194-196, 227]. The high surface area to volume ratio of nanoparticles and their concomitant ability to influence the host polymer segmental dynamics are considered important for achieving large property enhancements at low particle loadings [1, 195]. Unfortunately, these same attributes lead to strong, attractive van der Waals and polymer mediated depletion attraction forces between particles, which weakens control over their dispersion state and has detrimental effects on physical properties [1, 53, 194-196, 227].

Nanoparticles can be stabilized against aggregation in a host polymer using a variety of approaches [194, 227]. The most reliable involve electrostatic stabilization by a surface charge layer or steric stabilization as a result of repulsive excluded volume interactions between ligands/polymers attached to the particles. Of the two methods, steric stabilization is the more important for nanoparticle–polymer composites because it is applicable in a variety of environments (aqueous/non–aqueous) and is largely insensitive to the concentration of particles [194, 227]. Traditionally, physically adsorbed polymer chains were used to achieve steric stabilization of nanoparticles. With a few notable exceptions [32], this method is generally not preferred because chain desorption leads to bald patches on the particles, which destabilizes the

dispersions [194, 227]. Chemical attachment of polymer chains to particles via covalent or associated ionic bonds provides a more promising route for achieving stable dispersions of nanoparticles in polymers. With the increasing availability of thiol and silane linking chemistries for functionalizing metallic and metal oxide nanoparticles, this approach has been growing in popularity.

The stability of polymer–tethered nanoparticle–polymer composites has been studied using simple models where the hairy particles are modeled as spherical polymer brushes suspended in a polymeric media; the degree to which the host polymer and particle–tethered polymer chains interpenetrate provides a good indication of the phase stability of the system [36, 39, 101, 102, 107, 110, 113, 115-117, 119, 191, 199-202, 228]. Theories for polymers grafted onto flat substrates interacting with free polymer chains have been shown by experiments to adequately describe the phase stability of tethered nanoparticle–polymer systems in the limit of large particles and low grafting densities [39, 119, 191, 201]. For a host polymer of molecular weight, M_w, and a tethered polymer of molecular weight, $M_{w,teth}$, phase separation of the host polymer and particles is anticipated above a critical molecular weight ratio, $\alpha = M_w/M_{w,teth} \sim 1$. However, when the size of the nanoparticle becomes comparable to the radius of gyration of the tethered chains, curvature has a nontrivial effect on chain conformations in the brush and a few recent experimental studies show that tethered nanoparticle–polymer mixtures with a as high as 5 can be stable against phase separation [101, 102, 107]. At the same time, recent theoretical calculations that take into account the effect of curvature effects in such systems [113, 115, 116] find that phase separation of moderate to densely grafted particles occurs at a constant value of a that is largely insensitive to the variations in grafting density [116].

Many experimental works have investigated the rheology of soft spherical particles, including star polymers [229-234], diblock copolymer micelles [234-243], cross–linked microgel spheres [244], foams [245] and sterically stabilized nanoparticles [32, 36, 39, 53, 82, 102, 110, 191, 199, 201, 246-252] suspended in simple fluids. It is generally found that theories for colloidal suspensions with appropriate considerations for the contribution from the stabilizer layer on the particle size are adequate for describing the rheology of such materials. Tethered nanoparticles dispersed in low molecular weight oligomeric or polymeric hosts of the same chemistry are ideal for studying the rheology of colloidal suspensions owing to the small size of the particles, the repulsive inter–particle interactions, and minimal role of enthalpic interactions between the polymer stabilizer and suspending fluid. Rheology of suspensions of soft particles in polymeric hosts is more complex, but less studied [32, 102, 110, 191, 199, 201]; and even fewer studies have considered such suspensions in the limit of small particle sizes [32, 102, 191, 199], where large curvature effects and considerable variations in the effective particle size with increasing particle loading are anticipated.

In this chapter, we report the effects of curvature on the rheology of densely grafted nanoparticle suspensions comprised of sterically stabilized nanoparticles with sizes comparable to the tethered polymer chain length. The studied system comprised of polyethylene glycol (PEG) tethered silica (SiO_2) nanoparticles suspended in a PEG host is stable over a wide range of compositions, allowing us to investigate rheological behaviors in the simple fluid and jammed suspension states where the material exhibits soft glassy rheology. We also compare the linear and nonlinear rheology data for jammed suspensions with expectations based on simple brush models for the interparticle interaction profiles and predictions from the Soft Glassy Rheology (SGR) model.

5.2. Experimental Methodology

5.2.1. Tethered Nanoparticle Suspensions: Synthesis and Characterization

The suspensions studied here are the same for which structure characterization through SAXS was reported in the previous chapter. Briefly, silane functionalized polyethylene glycol chains (PEG, $M_{w,teth} \sim 450$ g mol^{-1}, supplied by Gelest Inc.) were tethered to SiO_2 nanoparticles with diameters (d) of 10 nm, 16 nm and 24 nm (LUDOX^{TM} SM–30, HS–40 and TM–50; supplied by Sigma Aldrich). Thermogravimetric analysis (TGA), carried out on an TA Instruments TGA Q500, of purified nanoparticles revealed an organic content of roughly 36, 26 and 14 wt% with increasing particle size; corresponding to grafting density of approximately 2.2 chains/nm^2, 2.1 chains/nm^2 and 1.6 chains/nm^2, respectively.

Suspensions of the nanoparticles were prepared by mixing appropriate amounts of nanoparticles with methoxy terminated Polyethylene Glycol (PEG, $M_w \sim 550$ g mol^{-1}, supplied by Sigma Aldrich). A range of such PEG–SiO_2/PEG suspensions were made with weight fraction (φ) of tethered nanoparticles varying from 0.001 to 0.8. The volume fraction of the nanoparticle cores (ϕ_c) in the suspensions was calculated from the measured φ_w and the ratio of densities of PEG to SiO_2, ρ, as $\phi_c = \rho\varphi_w/[1+ (\rho - 1)\varphi_w]$.

5.2.2. Rheology Measurements

Oscillatory shear rheology of the suspensions was characterized at 50^{o}C using a strain–controlled ARES–LS rheometer (Rheometric Scientific) outfitted with various cone and plate geometries (10 mm diameter; 0.1 cone angle, 25 mm diameter; 0.02 cone angle and 50 mm diameter; 0.02 cone angle). To study the linear viscoelastic properties of the materials, variable–amplitude oscillatory measurements at a fixed oscillation frequency $\omega = 10$ s^{-1} and frequency–dependent

oscillatory measurements at fixed strain amplitude $\gamma = 0.5\%$ were employed. Variable–amplitude oscillatory shear measurements were also used in conjunction of startup of steady shear flow, and flow cessation measurements performed with the ARES to evaluate the nonlinear viscoelastic and flow properties of the suspensions. For the most concentrated suspensions, these measurements were augmented by stress–sweep measurements carried out using a stress–controlled Physica MCR 501 rheometer (Anton Paar) outfitted with cone and plate fixtures (10 mm diameter and cone angle 0.035 rad). The steady–state values of the stress deduced from transient shear stress measurements during flow start–up experiments were used along with the stress–sweep measurements to construct flow curves for high volume fraction suspensions. For suspensions with lower nanoparticle loadings, start–up measurements were augmented with steady shear rate sweep experiments at shear rates in the range $0.1 \leq \dot{\gamma} \leq 1000\ s^{-1}$ to construct flow curves. At each shear rate studied, a measurement time of at least 100 s was used in the rate sweep experiments to ensure that the stresses attained steady–state. Data reported from the startup and cessation measurements are averages obtained over two experiments with opposite direction of shear. In the rate sweep measurements, all samples were pre–sheared and no waiting time was allowed, while for the stress sweep experiments, measurement at each stress values was carried out for 2000 s and the samples were pre–sheared by performing a dynamic amplitude sweep prior to the measurements.

5.3. Soft Glassy Rheology Model Calculations

The Soft Glassy Rheology (SGR) model proposed by Sollich has been shown in previous studies [67, 68, 172] to provide a good framework for studying the rheological behavior of jammed materials. An extension of Bouchad's trap–model, the SGR model allows for strain activated structural relaxation in these soft glassy materials. The model assumes an exponential

distribution of yield energies as $\rho(E) = e^{-E}$ and the stress in the material $\sigma(t)$ at any time t is related to the strain at all previous times, $\gamma(t')$;$0 < t' < t$ as,

$$\sigma(t) = \gamma(t) - \int_0^t dt' \Gamma(t') \gamma(t') G_\rho\left(Z(t,t')\right) \tag{6}$$

$\Gamma(t)$ denotes the yielding rate of the elements and is defined as

$1 = G_0\left(Z(t,0)\right) + \int_0^t dt' \Gamma(t') G_\rho\left(Z(t,t')\right)$ with the functions

$G_0(z)\left(= \int_0^1 dE P_0(E) \exp\left(-z \exp(-E/x)\right)\right)$ and

$G_\rho(z)\left(= \int_0^1 dE \rho(E) \exp\left(-z \exp(-E/x)\right)\right)$ representing the *survival probabilities*. Finally, $Z(t, t')$ is the effective time interval and is defined as $Z(t,t') = \int_{t'}^t dt'' \exp\left(\left(\gamma(t'') - \gamma(t')\right)^2 / 2x\right)$.

The only system parameter in this model is the effective noise temperature x, which describes coupled motion of individual elements in the material [68, 172]. The SGR model was solved numerically using MATLAB for comparison with the results from our flow startup and flow cessation experiments.

5.4. Results and Discussion

5.4.1. Steady State Flow Curves and Relative Viscosity

The flow curves for suspensions with d = 10 nm nanoparticles at different volume fraction are reported in Figure 20 (viscosity vs. shear rate) and Figure 21 (shear stress vs. shear rate). The filled symbols denote data obtained from controlled shear rate measurements, while the open symbols denote data from stress sweep measurements. The behaviors seen in this plot are

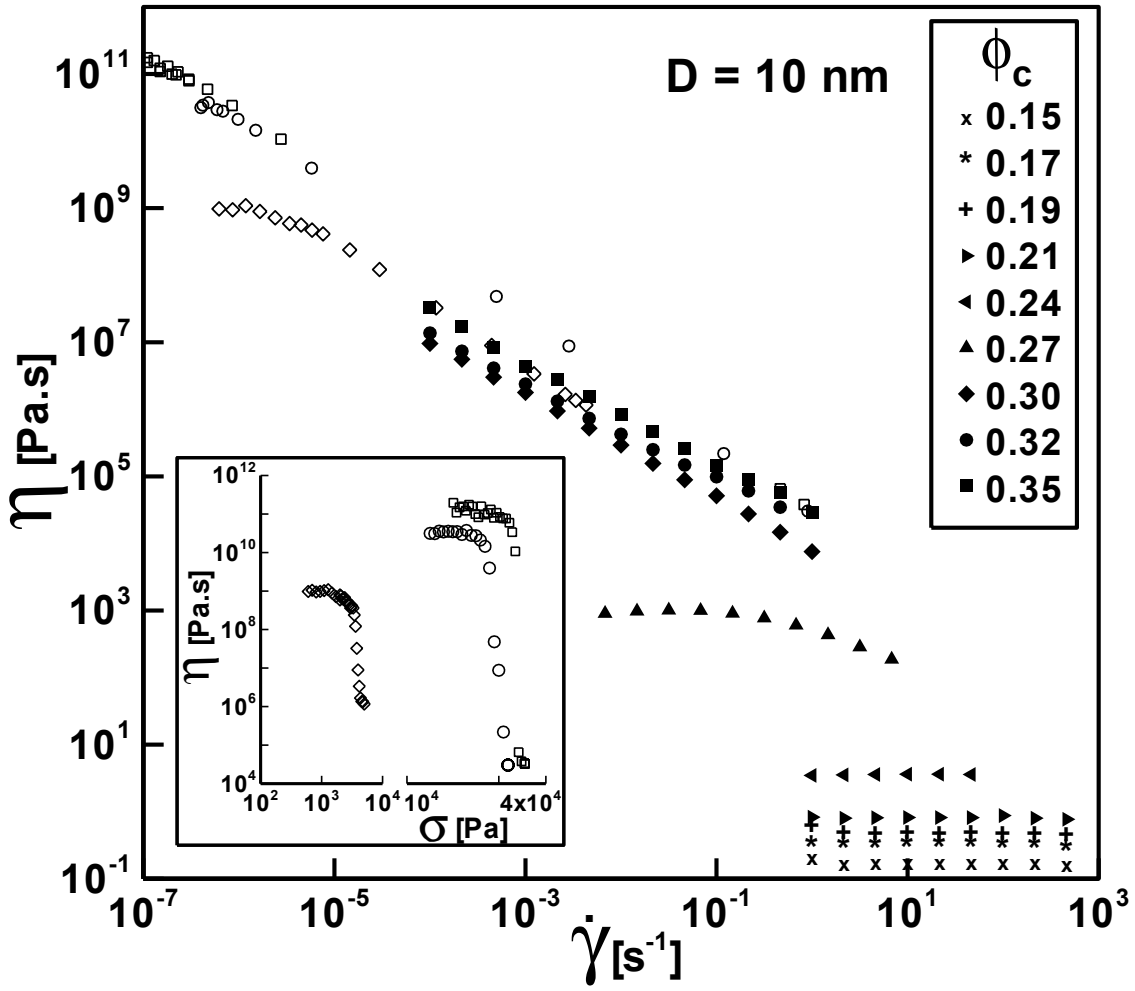

Figure 20 Viscosity vs. shear rate for PEG–SiO_2/PEG suspensions with d = 10 nm cores and ϕ_c as indicated in the figure. Filled and open symbols correspond to measurements from constant shear rate and constant stress measurements, respectively. *Inset*: viscosity vs. shear stress from the corresponding stress sweep measurements for the jammed PEG–SiO_2/PEG suspensions. The shear stress axis has adjusted scaling.

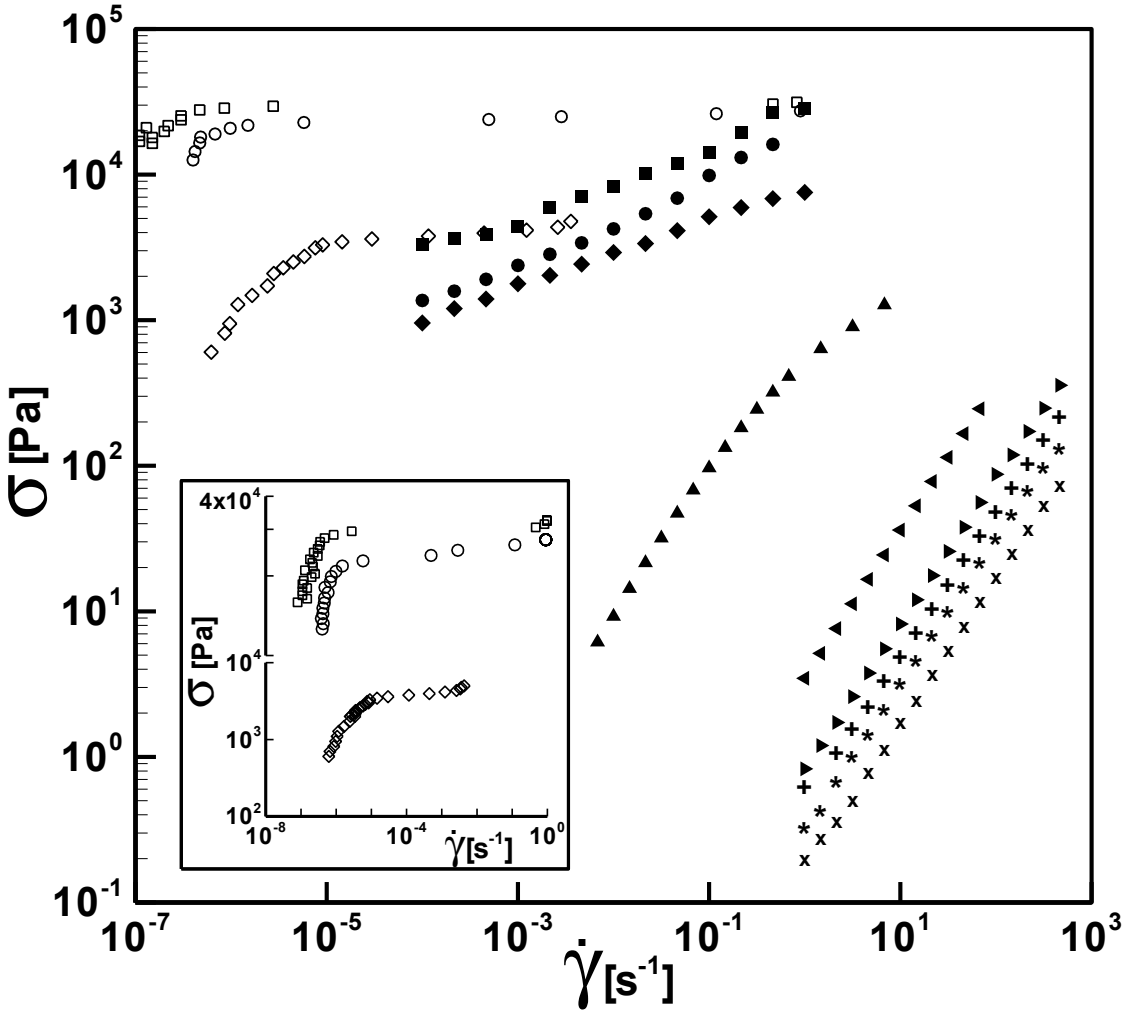

Figure 21 Shear stress vs. shear rate for PEG–SiO_2/PEG suspensions with d = 10 nm cores and ϕ_c as indicated in the Figure 20. Filled and open symbols correspond to measurements from constant shear rate and constant stress measurements, respectively. *Inset*: shear stress vs. shear rate from the stress sweep measurements for the jammed PEG–SiO_2/PEG suspensions with adjusted scaling.

representative for the PEG–SiO_2/PEG suspensions we have studied. Easily the most striking feature of these curves is the range of viscosities and flow characteristics that are accessible in a single suspension system through small variations in the particle volume fraction.

Specifically, the suspensions can be categorized into three distinct groups on the basis of their flow behaviors: (i) For ϕ_c = 0.15 – 0.24, the suspensions are simple Newtonian liquids over the entire shear rate range explored; (ii) For ϕ_c > 0.24 the suspensions are shear thinning fluids, with viscosity exhibiting a Newtonian plateau at low shear rates followed by a shear thinning region with continually decreasing viscosity at higher shear rates (ϕ_c = 0.27); and (iii) For ϕ_c > 0.30 the suspensions are jammed fluids with extremely high viscosities and a power law dependence of viscosity on shear rate at high rates. It is notable that even though the systems are jammed, a Newtonian flow regime is still present at very low shear rates accessible by controlled–stress, creep rheometry. As illustrated in the inset to Figure 20, the Newtonian regime is seen over a large–enough range of shear stress values to make its presence quite noticeable from controlled–stress measurements. The shear rate at which the Newtonian regime ends ranges from 2×10^{-6} to 5×10^{-7} s^{-1} for the suspensions, which means that the dynamic processes that drive the quiescent relaxation of the jammed materials are more than ten orders of magnitude slower than those responsible for relaxation of the host or tethered PEG chains.

The Newtonian and the shear thinning behavior observed at low and moderate ϕ_c can be understood in the framework of current theories for hard–sphere colloidal suspensions [253]. The tethered chains have ample space for relaxation at these volume fractions and hence the tethered nanoparticles behave as effective hard spheres. At low volume fraction, the particles are also spaced too far apart to bring about any structural changes under shear and the suspensions behave as Newtonian fluids. Increasing particle density leads to the potential for structural

changes under shear with particles possibly forming sheet like structures in the direction of the flow as reported in recent experiments [254]. The large variations in zero shear viscosity, spanning over eight decades, observed as ϕ_c is increased from 0.24 to 0.30 are understood to arise from the onset of collectivity associated with the jamming transition. For all systems studied, we find that an increase in ϕ_c by only 10% produces an increase in the zero shear viscosity by a factor of 10^7 Pa.s or more. This transition is evident at much lower volume fractions than in typical hard sphere suspensions because of the strong compression and interdigitation of the tethered polymer chains.

To facilitate comparisons with suspension rheology models, the relative zero shear viscosities (η_r) of various PEG–SiO_2/PEG suspensions are reported in Figure 22(a) as functions of ϕ_c. The solid line in the plots is the best fit obtained using the Krieger– Dougherty equation,

$$\eta_r = \left(1 - \frac{\phi_c}{0.638}\right)^{-0.638[\eta]} \tag{7}$$

[η] is the intrinsic viscosity, in this case 2.5, corresponding to hard spheres. This relation has been shown to predict the relative viscosity of hard sphere suspensions over a wide range of particle volume fraction and has been used extensively in the literature [253]. It is apparent from Figure 22(a), however, that η_r for the PEG–SiO_2/PEG suspensions exhibit significant deviations from this relation, even at particle volume fractions as low as 0.1. A straightforward explanation of these deviations is that at moderate particle loadings, the tethered PEG and SiO_2 particle act in concert as an effective hard core, which leads to a higher effective volume fraction of the suspended phase. This situation is not as straightforward as it might at first seem because even at the high grafting densities studied here, the tethered polymers are compressible, meaning that only a fraction of the attached chain might actually augment the SiO_2 particle in excluding

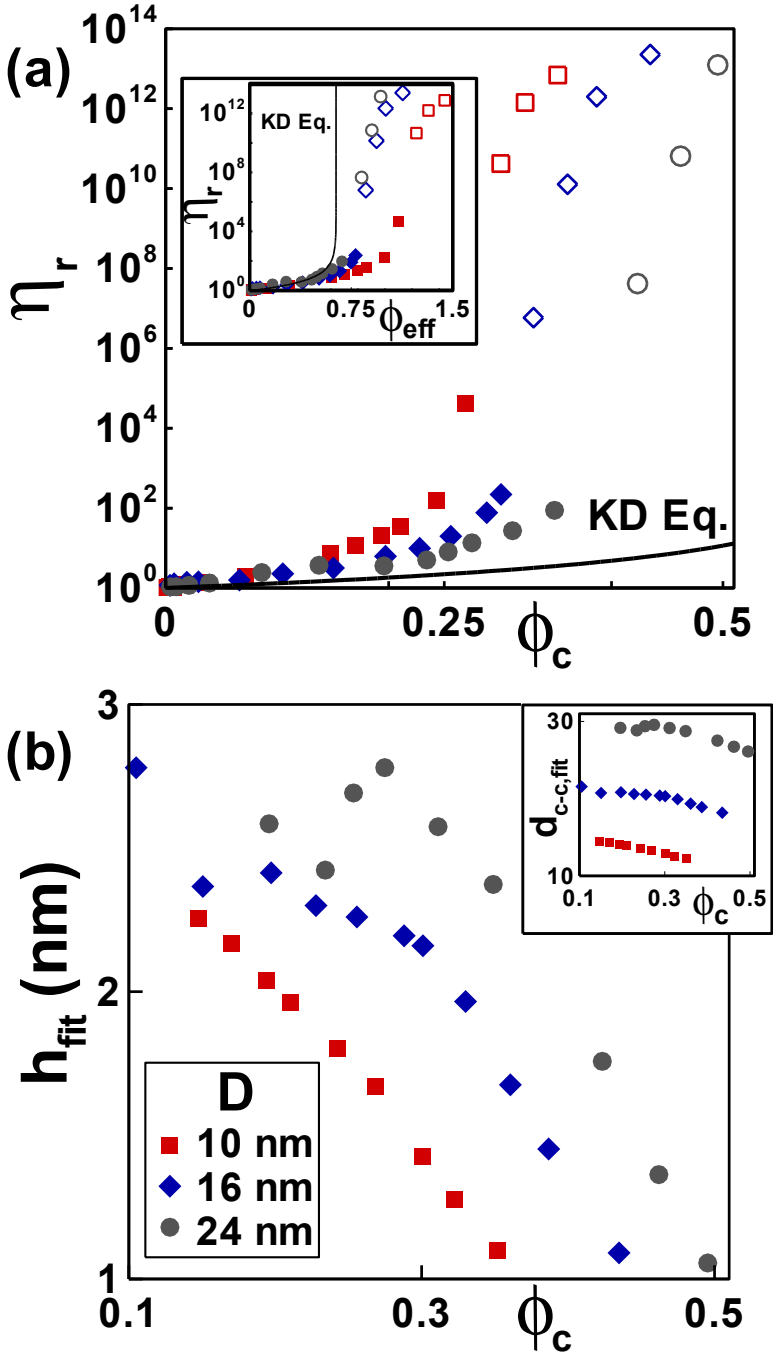

Figure 22 a. η_r vs. ϕ_c for different PEG–SiO_2/PEG suspension. The *inset* shows η_r vs. ϕ_{eff} plots for the same suspensions. Filled and open symbols correspond to measurements from constant shear rate and constant stress measurements, respectively. **b.** h_{fit} vs. ϕ_c for different PEG–SiO_2/PEG suspension. The *inset* shows $d_{c-c,fit}$ vs. ϕ_c plots for the same suspensions.

solvent and neighboring particles. Significant support for this possibility comes from Figure 22(a), which shows that the critical volume fraction at the onset of jamming progressively decreases with decreasing particle size and that the magnitude of the viscosity jump at the onset of jamming rises with decreasing particle size. The tethered polymers then contribute the most towards the effective volume of the particles for smaller particle cores. At the same time, the availability of the conformational space away from the surface of the particle is the maximum for particles with largest curvature, leading to greater chain interpenetration at the interface, more effective reinforcements (‘‘entanglements’’) between the tethered chains and a more dramatic increase in properties.

To estimate the effective volume fraction (ϕ_{eff}), we first calculate the brush height (h) by fitting the viscosity data for the very low volume fraction suspensions to the modified Einstein relation as,

$$h = \frac{D}{2}\left(\left(\frac{\eta_r - 1}{[\eta]\phi_c}\right)^{1/3} - 1\right); \text{ small } \phi_c \tag{8}$$

ϕ_{eff} corresponding to any ϕ_c is then calculated using the formula $\phi_{eff} = \phi_c(1+2h/d)^3$. The brush height determined in this manner is found to be close to the contour length of the tethered chain (~2.9 nm) for all systems studied, indicating that the tethered polymers are extremely stretched in the low volume fraction suspensions. As seen in the inset to Figure 22(a), the correction for volume of the nanoparticles using ϕ_{eff} indeed leads to a better fit of the data to the Krieger–Dougherty equation. However, beyond $\phi_{eff} = 0.5$, this strategy leads to overestimation of volume fractions, consistent with the earlier point that the tethered polymers are compressed at higher core volume fraction. Alternatively, the KD relation can be assumed to exactly describe the viscosity behavior of our suspensions and the measured relative viscosity used to calculate a new

brush height (h_{fit}), which provides an estimate of the degree of compression of the tethered chains as,

$$h_{fit} = 0.5D\left(\left(0.638\left(1-\eta_r^{-1/0.638[\eta]}\right)/\phi_c\right)^{1/3} - 1\right) \quad (9)$$

Figure 22(b) shows that h_{fit} follows a decreasing trend with increasing ϕ_c for all the three suspensions studied; a result that is again consistent with the idea that the tethered chains are compressed and confined at high ϕ_c. The inset of Figure 22(b) also reports the values for $d_{c-c,fit}$ (= $2h_{fit} + d$) with increasing ϕ_c, which is seen to follow a very similar trend and provides direct comparison with the d_{c-c} values estimated from the SAXS measurements presented in Chapter 4. Interestingly, the h_{fit} values are found to be smaller for smaller particles at a given volume fraction, which also follows directly from the notion that larger curvature leads to more relaxed chains near the interface between particles.

5.4.2. Flow Startup and Flow Cessation

Results from the step rate flow startup and flow cessation measurements for a representative high volume fraction, jammed PEG–SiO_2/PEG suspension (d = 10 nm cores and ϕ_c = 0.30) are shown in Figure 23. Figure 23(a) shows the transient stress profile with $\dot{\gamma}$ varying from 10^{-4} s^{-1} to 1 s^{-1}, from bottom to top. The time–dependent stresses are remarkably similar across the entire range of $\dot{\gamma}$ studied. Specifically, at early times the material responds as an elastic solid and an almost linear growth of the stress with time is observed. At later times, the stress deviates from linearity and exhibits a pronounced maximum (σ_{max}) or overshoot at all shear rates. At even later times, the stress exhibits a time–invariant plateau (σ_{ss}) or steady–state regime, corresponding to an ideal viscous response. The appearance of the stress overshoot during flow startup has been observed for a variety of materials and the point of deviation from linearity and point of the stress

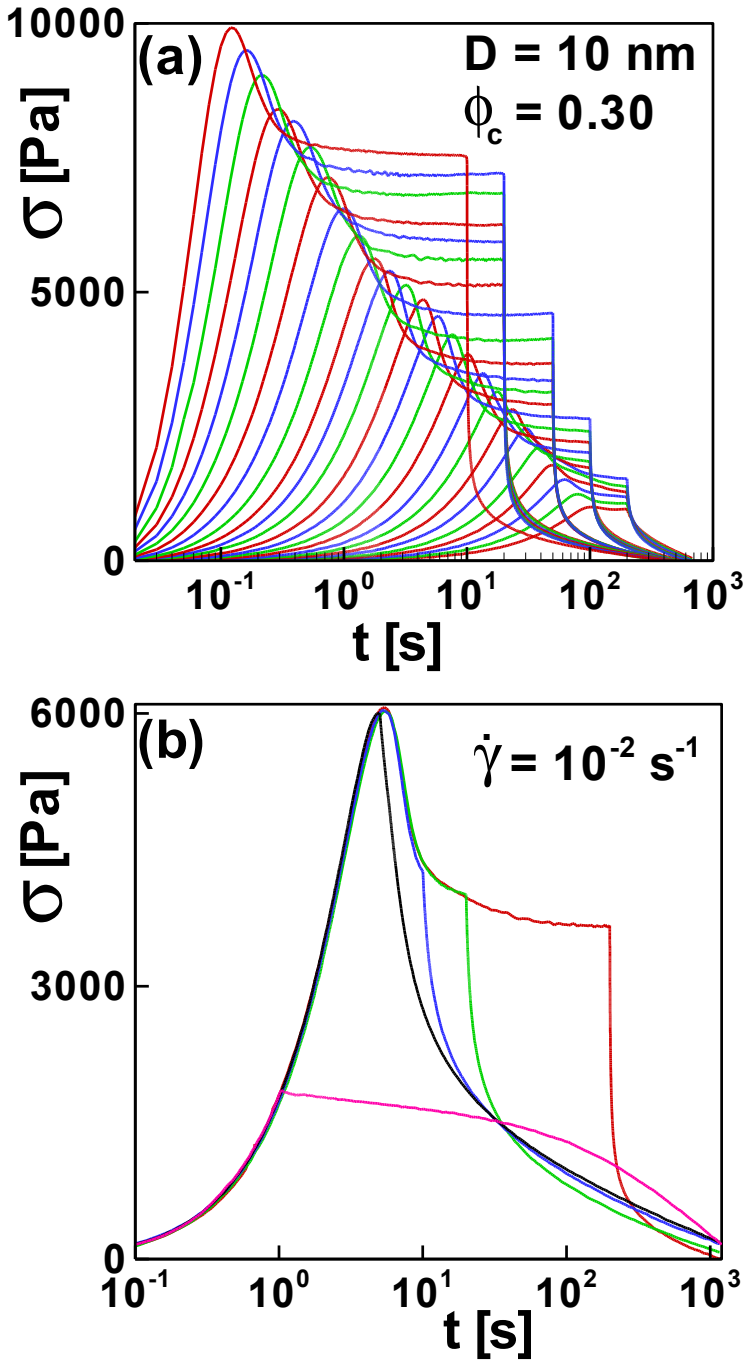

Figure 23 Stress profiles in flow startup and flow cessation for a PEG–SiO_2/PEG suspension with d = 10 nm and ϕ_c = 0.30 sheared at **a.** various rates increasing from 10^{-4} s^{-1} to 1 s^{-1} going from bottom to top and **b.** rate of 0.01 s^{-1} and t_{cess} = 200 s, 20 s, 10 s, 5 s and 1 s going from right to left.

maximum have been attributed to the transitions from elastic to plastic and plastic to viscous behavior, respectively [82, 244, 255, 256]. The stress value at the point of deviation from linearity and the stress maximum are thus often referred to as the elastic and the dynamic yield stress.

The elastic to viscous transition in the flow response under constant shear are further elucidated by studying the stress profiles in the event of flow cessation ($\dot{\gamma} = 0 \forall t > t_{cess}$), where the stress is seen to follow a two–step relaxation with a sudden decay followed by a gradual relaxation to the zero value. Stress decay profiles are studied as a function of flow cessation times, t_{cess}, on either side of the time corresponding to the maxima in the stress, at a constant $\dot{\gamma}$ as shown in Figure 23(b). The relaxation profile varies from a prominent two step decay when the flow is stopped at 200 s, after the appearance of the maxima (t_{cess} = 200 s) to a gradual one step decay when flow cessation occurs before the appearance of the maxima, as observed for t_{cess} = 1 s. The two–step relaxation is therefore firmly connected to the microstructural changes that produce the stress overshoot. It can be understood to be composed of a fast relaxation mode and a slow relaxation mode, corresponding to the relaxation of viscous stresses and structure of the system. These points will be explored in greater detail later with the help of the SGR model.

Figure 24(a) reports normalized time–dependent shear stresses ($\sigma_n(t) = \sigma(t)/\sigma_{ss}$) during shear startup for PEG–SiO_2/PEG suspensions with volume fractions on either side of the jamming transition. The suspensions with volume fractions below the jamming transition display a continuous buildup of shear stress up to the steady state value and the stress overshoot occurs only for the jammed suspensions. Thus, this plot clearly identifies the overshoot with jammed matter. The figure also shows that the magnitude of the overshoot initially increases strongly with the particle volume fraction, and then saturates. The shape of the overshoot, however,

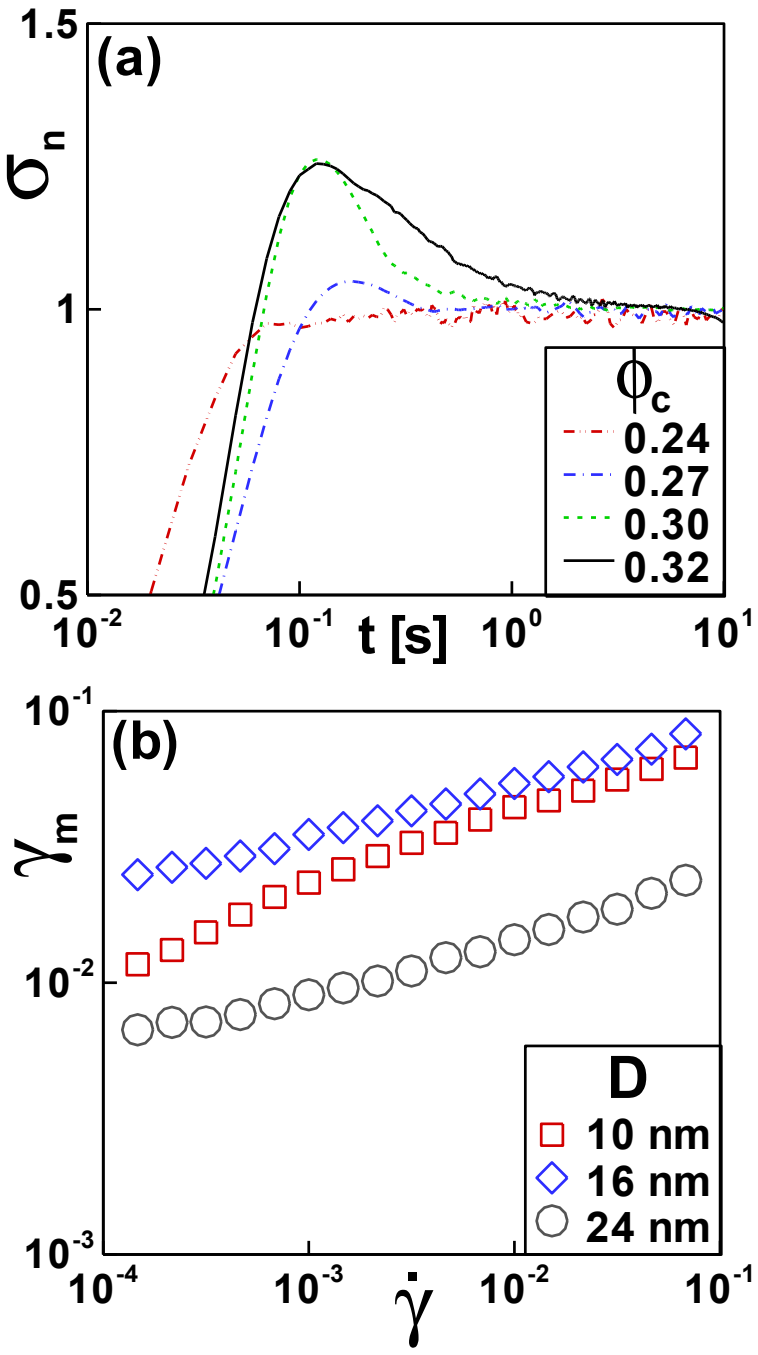

Figure 24 a. Normalized transient shear stress profiles during flow startup at a fixed shear rate of 1 s^{-1} for PEG–SiO_2/PEG suspensions with ϕ_c = 0.24, 0.27, 0.30 and 0.32, from bottom to top. **b.** Shear strain at the shear stress maximum vs. rate for jammed suspensions with d = 10 nm, 16 nm and 24 nm cores and ϕ_c = 0.3, 0.36 and 0.46, respectively.

becomes progressively sharper as ϕ_c increases, indicating that the jammed material effectively becomes more brittle as the particle content rises. The shear strain, γ_m, at which the stress maximum is observed is reported in Figure 24(b) for three different SiO_2 particle sizes, three different particle volume fractions, and at a range of shear rates. In agreement with previous studies [82, 244], it is also notable that γ_m is a weak, increasing function of shear rate and is at most a weak function of d and ϕ_c over the range of these parameters studied.

5.4.3. Oscillatory Shear Rheology

Figure 25(a) and (b) report the dynamic storage and loss moduli, *G'* and *G"*, of a typical jammed suspension measured using oscillatory shear experiments performed at variable shear strain amplitude and shear frequency, respectively. The most noticeable feature from the amplitude sweep measurements in Figure 25(a) is that the material is transformed from a dominantly elastic (*G'* » *G"*) to a dominantly viscous (*G"* » *G'*) state when the strain is increased beyond a certain value. It is also noticed that at shear strains near the transition, the loss modulus exhibits a pronounced maximum, indicating that a highly dissipative (disruptive) process is underway in the material's microstructure. All of these behaviors are consistent with expectations from experiments using a variety of jammed systems and are considered to be a signature of jamming, with the height of the maxima indicative of the extent by which shear can un–jam the system [68, 172]. The frequency–dependent measurements reported in Figure 25(b) reveal additional important characteristics of our materials. The figure not only shows that elasticity dominates in the linear viscoelastic regime, but that both moduli are only weak functions of frequency, which is considered to be another signature of jammed matter. As discussed in the next section, all of these features are predicted by Sollich's SGR model [68], which makes the model a good tool for understanding the continuum–scale physical processes that produces the rheological

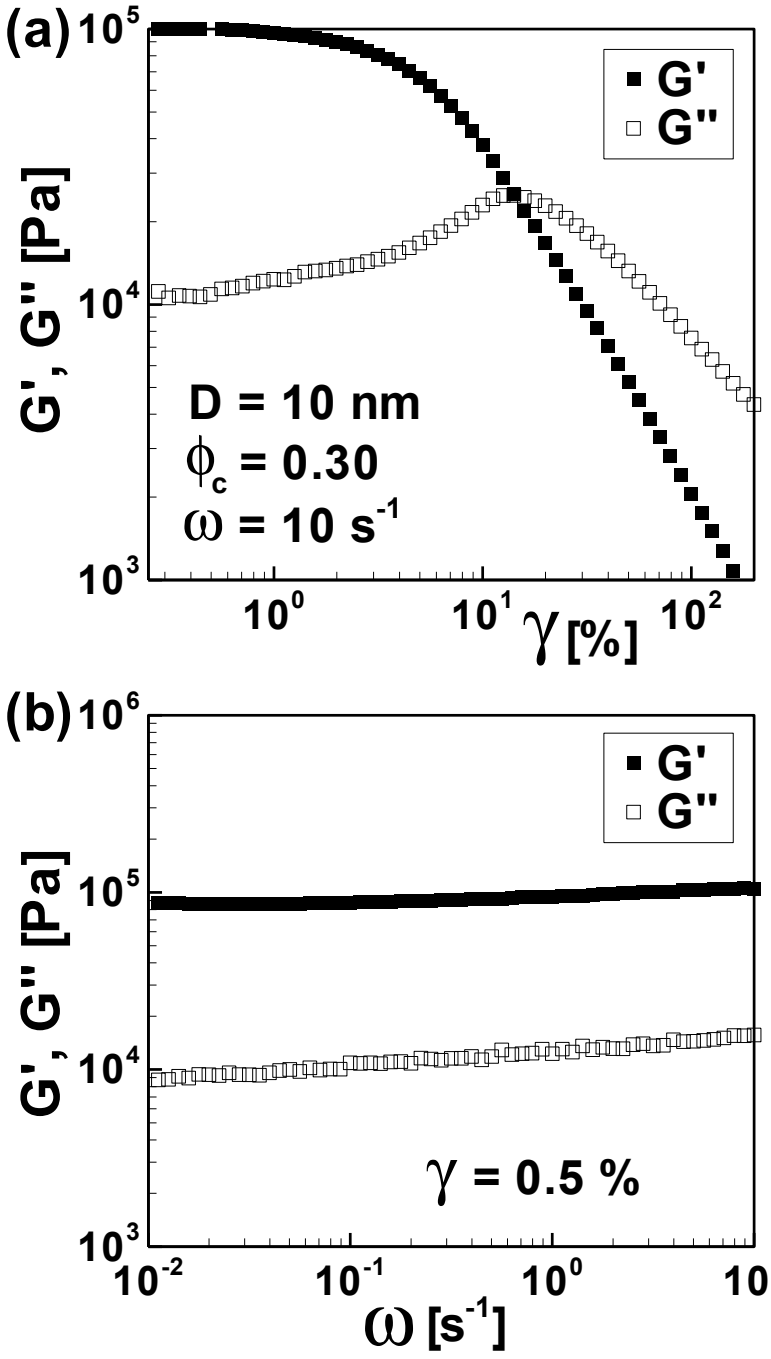

Figure 25 a. *G'* and *G"* vs. rate at $\omega = 10\ s^{-1}$ and **b.** *G'* and *G"* vs. ω at $\gamma = 0.5$ % for a PEG–SiO_2/PEG suspension with $d = 10$ nm cores and $\phi_c = 0.30$.

behaviors seen in experiments.

5.4.4. Comparison with the SGR Model

Figure 26 are the transient stress profiles predicted by the SGR model for the corresponding scenarios in Figure 23. The shear thinning exponent *m* extracted from the flow curve, $\sigma \sim \dot{\gamma}^m$, is predicted by the SGR model to scale as $x - 1$. Therefore, the equations presented in Section III were solved for $x = 1.24$ corresponding to $m = 0.24$ deduced from the data presented in Figure 23(a). The stress profiles during flow start–up and flow cessation for $x = 1.24$ and different $\dot{\gamma}$ shown in Figure 26(a), are remarkably similar to those observed from experiments (see Figure 23(a)). The elastic to viscous transition of the stress response in the SGR model is understood to originate from the complete disruption of the equilibrium structure (yielding) in glassy materials beyond a critical yield strain, which is preceded by continuous rearrangement of the cages/traps formed by neighboring structural elements around a test element. The cage relaxation by activated hopping is slower than the build up of the stress in the cages, leading to a higher overall stress before yielding occurs, hence the stress overshoot. Shearing at higher rates leads to faster build up of stress and consequently produces larger magnitude of overshoots compared to the shear stress magnitude at steady state. These features are all in accord with observations from flow start–up measurements. Other features of the model, such as the weak dependence of the critical strain at the stress maximum upon the shear rate and particle loading (roughly analogous to *x*, see discussion below) and the growth in the size of the stress maximum with distance from the jamming transition (*x*), are also qualitatively similar to what is revealed by experiments. The SGR model can also be used to gain insight into the response of our materials following flow cessation. Specifically, the two–step response following flow cessation is the result of superposition of a fast viscous response, corresponding to stress relaxation in the completely

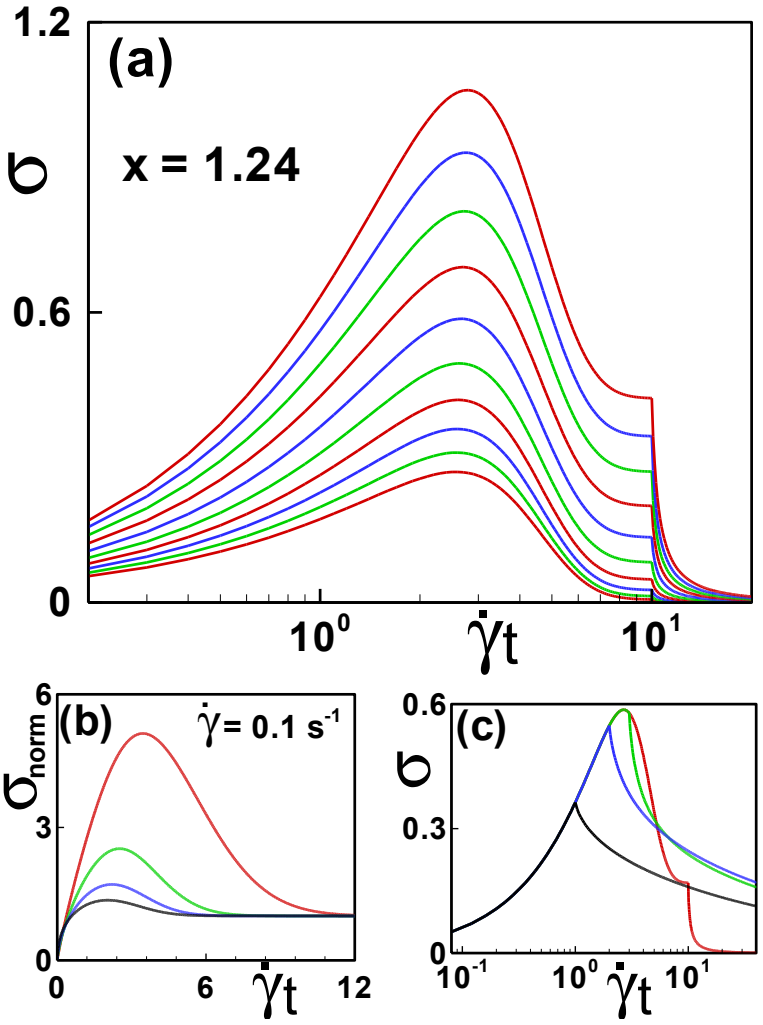

Figure 26 a. Stress profiles in flow startup and flow cessation calculated using the SGR model with x = 1.24 at various rates increasing from 10^{-3} s^{-1} to 10^{-1} s^{-1} going from bottom to top. **b.** Normalized stress profiles calculated using the SGR model at a rate of 10^{-2} s^{-1} and x = 1.7, 1.5, 1.3 and 1.1 going from bottom to top. **c.** Stress profiles in flow startup and flow cessation for the same case as **a.** at a rate of 10^{-2} s^{-1} and γ_{cess} = 10, 3, 2 and 1 going from right to left.

disrupted systems, and a slower structural response due to gradual restoration of the cage structure. Further, the cage rigidity of the material is directly related to the extent of jamming in the system and consequently, the magnitude of the stress overshoot increases with decreasing x, which corresponds to increasing jamming in the system and is shown in the Figure 26(b). On the other hand, the stress profiles for steady shear flow ceased at different times, similar to the experiments presented in Figure 23(b) are shown in Figure 26(c) and demonstrate clearly that smaller deformations, which do not bring about absolute structural disorder, lead to a slow, one step, elastic–like stress relaxation response.

Figure 27 provides a more quantitative comparison between our experimental observations and the SGR model. As mentioned earlier, the shear thinning exponent m is predicted by the SGR model to scale as $x - 1$. Values of m corresponding to various values of x were found by performing the calculations at various $\dot{\gamma}$ at the given x. The loss tangent $\tan\delta$ ($= G''(\gamma)/G'(\gamma)$) in the linear viscoelastic regime is also related to x through the formula, $\tan\delta = \tan\pi(x-1)/2$ [172]. Suspensions with higher volume fractions exhibit a higher degree of jamming and correspondingly exhibit smaller values of $\tan\delta$ as well as m as shown in the experimental data points (filled symbols) in the Figure 27. Also, the data reveals an approximately linear relation–ship between $\tan\delta$ and m with $\tan\delta = 0.7m$ (dashed line). This potentially provides a simple method of estimating the shear–thinning coefficient from oscillatory rheology measurements performed in the linear viscoelastic regime. However, the experimentally determined scaling deviates noticeably from the scaling relation proposed by theory (open symbols). It is understood, though, that even these differences may stem from simple sources, e.g. insufficient knowledge of the energy landscape between elements in a soft glass and of the constant pre–factors used in the SGR model to describe how the landscape can change in response to shear.

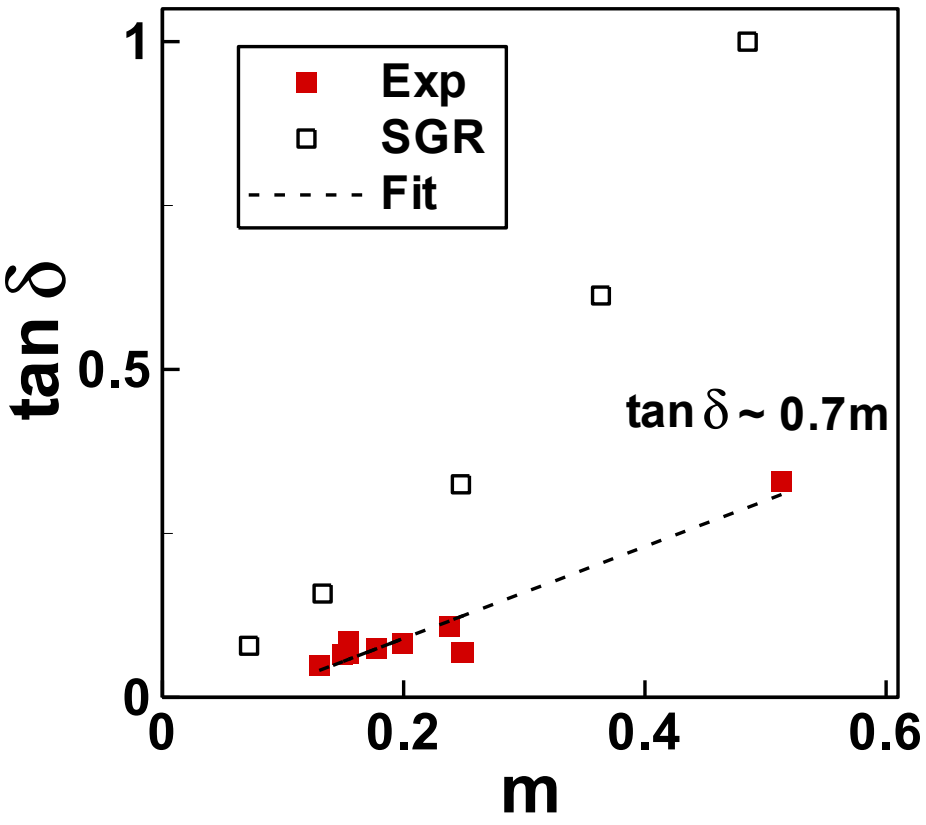

Figure 27 tan δ vs. m for PEG–SiO_2/PEG suspensions and the predictions from the SGR model. The dashed line is a linear fit to the data.

5.4.5. Rheology and Inter–Particle Interactions

In this section, we attempt to estimate the form of the inter–particle interaction forces in PEG–SiO_2/PEG suspensions from their bulk rheology. Repulsive inter–particle interactions are understood to produce the elastic forces in jammed suspensions and are responsible for the frequency–independent, storage modulus ($G'_{\infty}(\omega)$) in the limit of high frequency. The storage modulus, G, has consequently been shown to be related the inter–particle potential ($U(r)$) through the Mountain–Zwanzig equation [253] as:

$$G = \rho k_B T + \frac{2\pi}{15}\rho\int_0^{\infty} dr g(r)\frac{d}{dr}\left(r^4\frac{dU(r)}{dr}\right) \tag{10}$$

with ρ, k_BT and r being the particle number density, product of Boltzmann constant and temperature and the inter–particle distance, respectively. In the limit of high particle volume fractions, the radial distribution function can be assumed to exhibit features analogous to crystalline materials, with sharp well–defined peaks. In this case the above expression can be simplified to give [249]

$$G = \frac{1}{5\pi}\frac{n\phi_m}{r}\frac{d^2U(r)}{dr^2} \tag{11}$$

The interaction potential for the particles has been approximated by applying the Derjaguin approximation to the potential calculated by Milner [99] for interaction between two flat grafted surfaces, to arrive at $U(r) \sim U_0$ (ln $1/y + O(y^2)$), where U_0 is a constant pre–factor and y is the particle surface–to–surface separation non–dimensionalized with the brush height [36]. Using this modified Milner potential in equation (11) leads to,

$$G(r) \sim \frac{U_0}{h^2(hy + D/2)}\left(y^{-2} + O(y)\right) \tag{12}$$

Figure 28 shows the variation of scaled shows the variation of scaled $\bar{G}'_{\infty}\left(=G'_{\infty}h^2\left(hy+D/2\right)U_0^{-1}\right)$ and scaled $\bar{G}_0\left(=G_0h^2\left(hy+D/2\right)U_0^{-1}\right)$ with y, where G_0 is the bulk modulus observed in the limit of small strains in the shear startup experiments presented in Figure 23(a), $G_0=\lim_{t\to 0}\sigma/\dot{\gamma}t$. The data for the three different particle sizes used in the study collapse nicely onto each other, indicating that there is indeed a universal relationship between $\bar{G}'_{\infty}$, $\bar{G}_0$ and the inter–particle spacing. However, as shown in the figure, a scaling of –9.5 is observed as opposed to –2 predicted by the model (shown as solid and dashed lines in the figure), which leads to $G\sim y^{10.5}$, and thus $U\sim r^{7.5}$. It should be noted that while the –7.5 scaling of U with r is far removed from the –ln r scaling predicted by the modified Milner potential and also from the scaling of –1.2 reported for sparsely tethered nanoparticles [191], it is fairly close to the value of –11.7 reported for soft core–shell nanoparticles [252]. That the interaction potential is a much stronger function of particle separation is perhaps expected for the highly curved nanostructures considered here. We tentatively attribute our observations to: (a) failure of the Derjaguin approximation in the case of strong curvature as is the case presented here; and (b) inadequacy of Milner potential to describe the interaction between highly compressed brushes. In either scenario, applicability of the modified Milner potential appears limited in these high volume fraction suspensions of densely grafted, stable nanoparticles where the tethered polymer chains are highly confined.

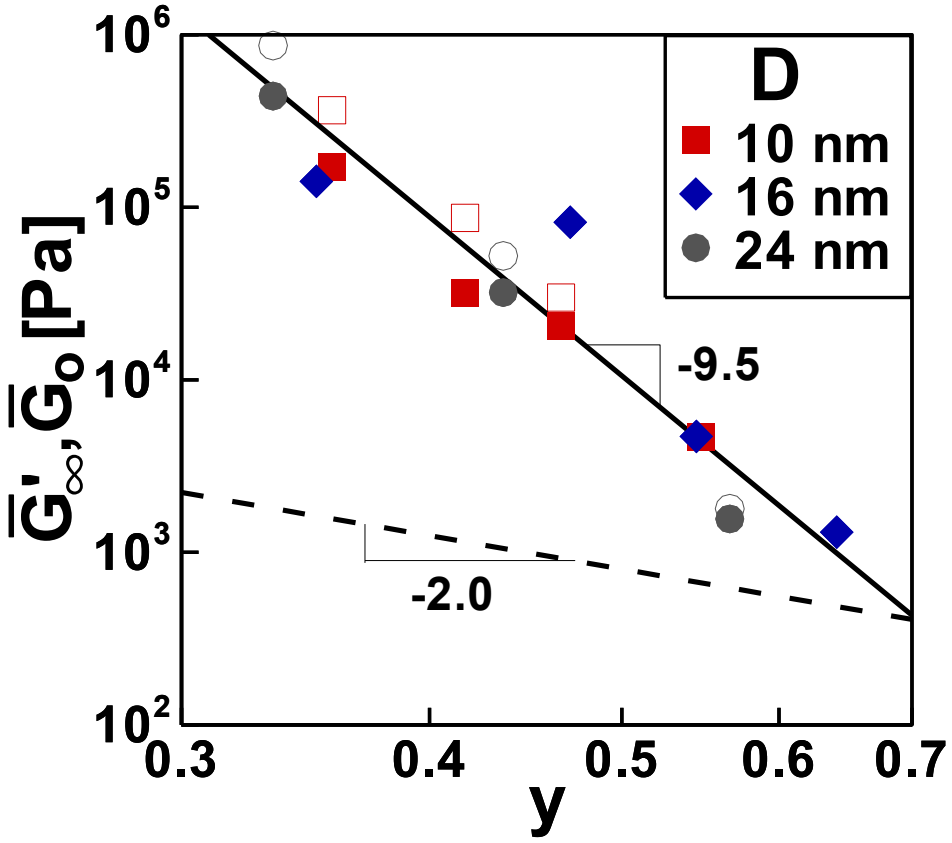

Figure 28 Scaled moduli vs. *y* for three PEG–SiO_2/PEG suspension. The solid line is the fit to data with power law scaling of –9.5 while the dashed line is a guide to the eye with a power law scaling of –2.0.

5.5. Conclusions

We have studied the structure and rheology of model nanoparticle–polymer suspensions created by blending densely grafted PEG–SiO_2 particles in a low molecular weight PEG host. By varying the particle size and volume fraction in the suspensions, we are able to investigate the effect of particle geometry on phase stability of the mixtures and on the rheology of the suspensions over a wide range of nanoparticle loadings. We are also able to facilely tune the degree of jamming and the so–called noise temperature, x, of the suspensions allowing detailed comparisons with theory for jammed matter. From small angle X–ray scattering (SAXS) and transmission electron microscopy (TEM) analysis we conclude that all systems studied exhibit enhanced phase stability relative to expectations from theory. We tentatively attribute this behavior to the strong curvature of the polymer brushes imparted by their nanometer–sized substrates. We also find that tethering polymers to particles produce important insight into how physical variables influence rheological response. Specifically, we report that (i) through small changes in the particle volume fraction, rheological properties of nanoparticle/polymer suspensions can be tuned over a wide range–from simple Newtonian fluids to jammed, shear–thinning waxes; (ii) the rheology of suspensions comprised of smaller particles show larger deviations from expectations based on theories for hard–core colloidal suspensions due to larger contribution by the tethered polymers towards the effective particle size; (iii) the jamming or glass transition in PEG–SiO_2/PEG suspensions occurs over small increments in the core particle volume fraction, leading to very sharp growth in the viscosity of the suspensions; (iv) the viscosity jump at the jamming transition is larger for smaller particles (larger curvature), which leads us to conclude that higher curvature leads to higher extent of chain interdigitation and

consequently jamming; and (v) larger particle curvature leads to smaller tethered polymer brush heights owing to availability of larger conformational space for the tethered chains.

Additionally, we characterized the viscous and viscoelastic properties of jammed PEG–SiO_2/PEG suspensions using various shear flow experiments and theory. These measurements clearly show that the qualitative rheological characteristics of the materials place them firmly in the universal class of soft glassy materials. The stress response during flow startup as well as flow cessation revealed an elastic to viscous transition in the suspensions under shear which is understood to be brought about by the complete disruption of the structure (breaking of the cages) during shear. Furthermore, the shear thinning coefficient and the loss tangent in the linear viscoelastic regime are found to be proportional to each other, providing a convenient method for estimating the shear–thinning coefficient from simple, small–amplitude oscillatory shear measurements. Lastly, the inter–particle interaction force is found to be a stronger function of particle separation than anticipated from theories for interacting polymer brushes grafted to planar substrates. In this regard, the high volume fraction suspensions, with highly compressed tethered chains are quite similar to suspensions of soft particles.

CHAPTER 6

TIME–STRAIN SUPERPOSITION IN SOFT GLASSES: ACCESSING EXTREMELY SLOW RELAXATIONS THROUGH RHEOLOGY

Abstract

This chapter reports a novel time–strain superposition (TSS) procedure for determining the long time, linear viscoelastic response of soft glassy materials. Dynamic shear measurements performed over a limited range of time or shear frequencies, and at discrete shear strains can be overlaid to create master curves, which span more than sixteen decades in time. For shear strains above the yield strain, the strain–dependent shift factor required to achieve superposition in oligomer–suspended as well as self-suspended nanoparticle glasses are of identical form to that represented by the Williams–Landel–Ferry (WLF) equation typically employed for time–temperature–superposition (TTS) in polymers above their glass transition. By comparing TSS behavior observed in the experiments with predictions based on Sollich's soft glassy rheology (SGR) model, we further show that this behavior is in fact a generic feature of all soft glasses described by this model.

6.1. Introduction

The glass transition has been termed the richest and most important unsolved problem in condensed matter physics. One of the simplest models for a glass is a dense collection of hard spheres in a liquid dispersant. Substantial progress in understanding glasses and glassy fluid dynamics has been achieved using this model in conjunction with mode–coupling theory (MCT) [257], and experiments employing suspensions of monodisperse colloidal particles [62, 258] and densely–branched polymeric stars [229]. Because of their jammed and metastable structure, more complex suspensions of polydisperse particles [259], pastes [260], microgels [244, 261] and emulsions [262], collectively termed soft glassy solids [67], have also attracted significant attention as physical models for understanding natural processes such as ageing and rejuvenation of molecular glasses [260, 263, 264].

These soft glassy materials are characterized by extremely long relaxation time scales, which are typically outside the window of experimental observations. In this chapter we report a simple time–strain superposition (TSS) procedure that can be used to create rheological maps of soft glasses that cover unprecedented time–scales ($\omega^{-1} \approx 10^{15}$ s). Frequency sweep measurements carried out over various discreet strain values are shown to be superimposable through simple shifting procedures, resulting in master curves which provide a unique continuous description of the long-time viscoelastic behavior of the soft glassy materials. We present experimental verification of this procedure on sterically stabilized, *soft* nanoparticles that were created by dense, covalent attachment of polyethylene glycol (PEG) oligomers to the surface of silica (SiO_2) nanoparticles. These tethered nanoparticles, as well as their suspensions in PEG oligomers, yield and flow like typical soft glasses, yet are able to relax to equilibrium over long time scales (Chapter 5). Consistent with the report by Agarwal et al. [42], we find that a simple time–strain

superposition (TSS) procedure can be used to create rheological maps of suspension dynamics that cover unprecedented time–scales. We also find this procedure to be applicable to material response predictions provided by Sollich's soft glassy rheology (SGR) model, providing strong support for the applicability of the TSS procedure on a wide range of soft glassy materials.

6.2. Experimental Methodology: Nanocomposite Synthesis

Short ($M_w \approx 450$ g/mol) polyethylene glycol–grafted silica (SiO_2) nanoparticles ($d = 10 \pm 2$ nm) were synthesized using a standard organosilane–based grafting chemistry [43, 53, 265, 266]. Untethered organosilane molecules were removed by repeated precipitation of nanoparticles in a partial solvent (a mixture of ethanol and n–hexane). Polyethylene glycol oligomers ($M_w \approx 550$ g/mol) were added to the purified suspensions of nanoparticles in chloroform and the resulting PEG–SiO_2/PEG suspensions were rigorously dried in vacuum at room temperature for several days. The material produced by this process has a waxy consistency at room temperature. Thermal gravimetric analysis (TGA) reveals that it is comprised of 25.5 vol. % silica, and, as reported previously [43], examination by electron microscopy indicates that the silica is in the form of a disordered array of well–dispersed nanospheres, with no evidence of aggregation. The grafting density of the PEG chains was estimated to be around 2.8 chains/nm^2 from thermogravimetric analysis. The dense grafting of the PEG chains ensures complete screening of the attractive van der Waals interactions between the SiO_2 nanoparticles and provides for homogenous dispersion of the nanoparticles in the host polymer.

6.3. Results and Discussion

Dynamic storage, *G'*, and loss, *G"*, moduli for PEG–SiO_2/PEG suspension were measured at 50^{o}C in small–amplitude oscillatory shear ($\gamma(t) = \gamma_0 \sin[\omega t]$). The frequency sweep results for a suspensions with $\phi = 0.26$, are reported in Figure 29a and show that at low strains γ_0, *G'* (closed

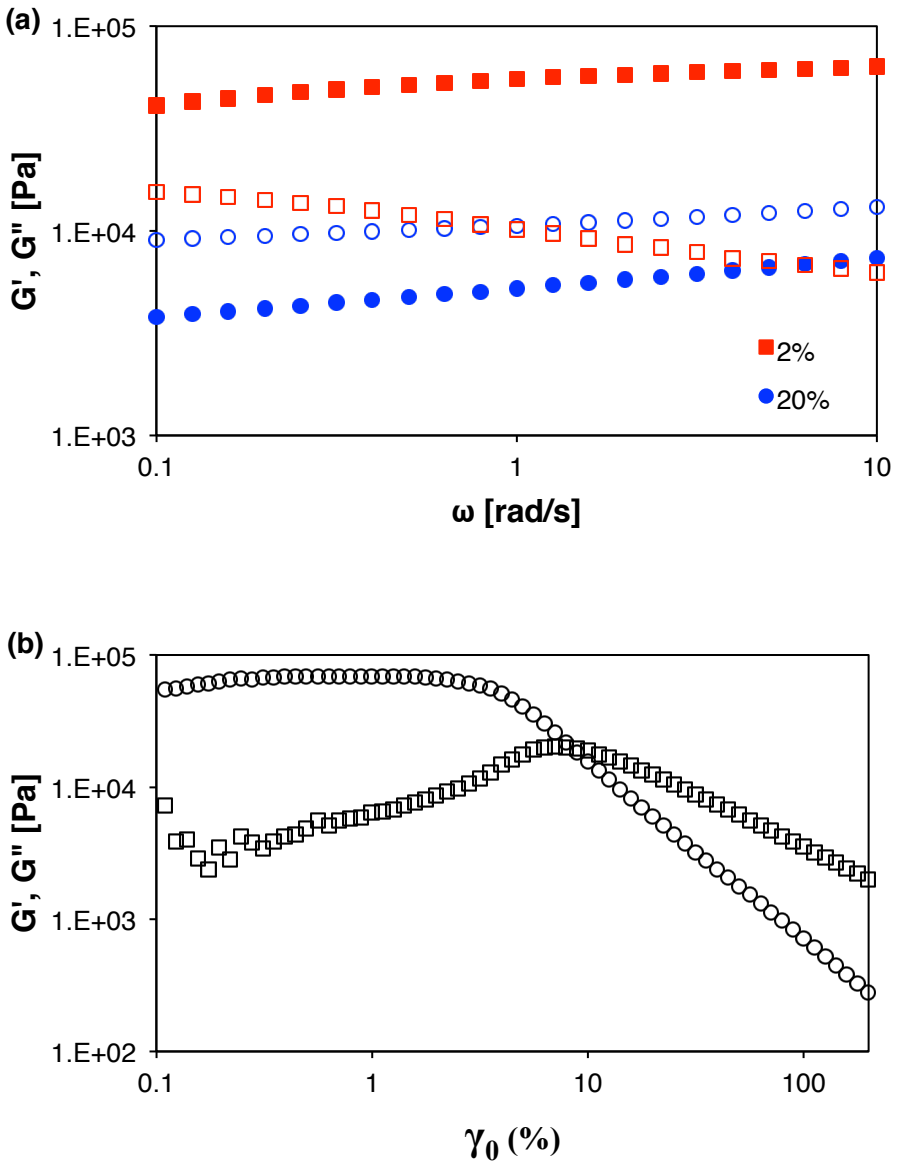

Figure 29 Dynamic rheology measurements for tethered nanoparticle suspensions with $\phi = 0.26$. **a.** Storage (G', closed symbols) and loss (G'', open symbols) moduli vs. frequency ω for two different strain amplitudes γ_0. **b.** Storage (G', circles) and loss (G'', squares) moduli vs. strain amplitudes γ_0 at ω = 10 rad/s.

symbols) dominates G'' (open symbols), and is a weak functions of frequency ($G' \sim \omega^{0.1}$). At high γ_0, disruption of the cage structure results in a non–linear response of the material concomitant with $G'' > G'$ and a stronger dependence of both G' and G'' on ω ($G' \propto G'' \sim \omega^{0.15}$). Figure 29b reports the corresponding strain–dependent dynamic moduli at various strains and temperatures. At low strains, the elastic modulus is again seen to be larger and both moduli are independent of γ_0. The elastic modulus for the ϕ = 0.26 SiO_2–PEG/PEG suspension is $G_e \sim 7 \times 10^4$ Pa, which is substantially larger, by a factor of at least 10^3, than the modulus of the suspending fluids PEG–550 or the tethered PEG–450 corona, clearly showing that the hard silica cores provide excellent mechanical reinforcement to the suspension. At larger strains, a crossover from solid–like, G'–dominant, to liquid–like, G''–dominant, behavior is observed. This crossover coincides with the appearance of a maximum in $G''(\gamma_0)$ at a shear strain γ_y.

The main results in this chapter are summarized in Figure 30. Surprisingly, we find that $G'(\omega)$ and $G''(\omega)$ obtained from experiments performed at multiple discrete shear strains can be juxtaposed by horizontal and vertical shifting to produce a continuous map of the materials dynamic response over a substantially extended time range. Each individual measurement was performed over a narrow range of oscillation frequencies ($0.1\ s^{-1} < \omega < 10\ s^{-1}$), intentionally chosen to minimize the effect of inertial errors at high frequency during the measurements. The master curve shown in the inset of the figure highlights the goodness of the superposition procedure. This behavior is observed for both the self–suspended [42] and oligomer–suspended particles, indicating that it is not unique to the materials studied here. Termed time–strain superposition (TSS) [42, 267, 268], the approach is analogous to the more widely studied time–temperature superposition (TTS) methodology [269], where in the dynamic range is increased by horizontal (and vertical) shifting of measurements performed at multiple temperatures. Some of

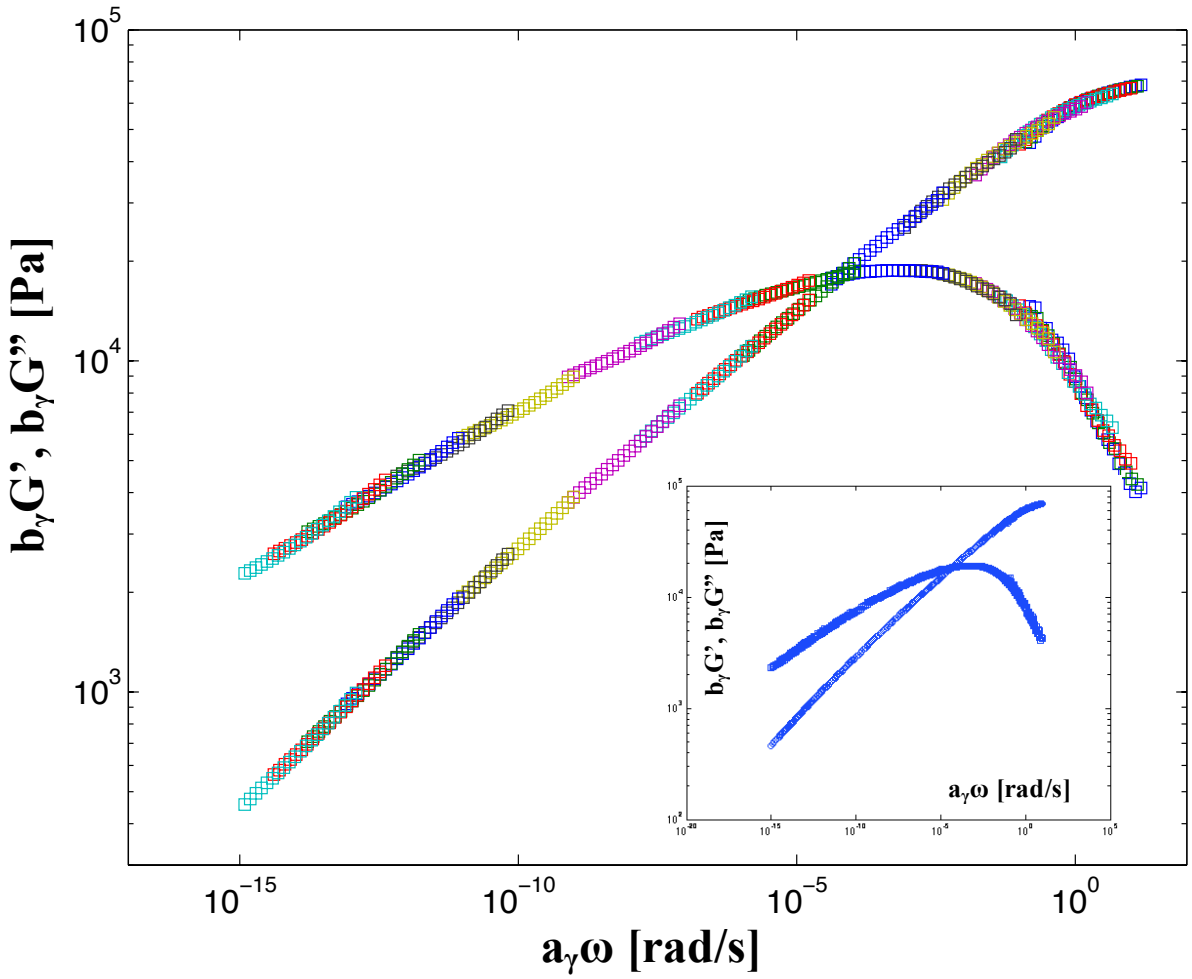

Figure 30 Shifted storage ($b_\gamma G'$, closed symbols) and loss ($b_\gamma G''$, open symbols) moduli vs. shifted frequency $a_\gamma \omega$ for tethered nanoparticle suspensions with ϕ = 0.26. The shifting was carried out with the γ_0 = 1% as the reference measurement. *Inset* shows the master curve obtained after the shifting procedure.

the earliest reported examples of TSS come from the work of O'Connell and McKenna [267, 268] on stress relaxation of polycarbonate glasses, below T_g. In comparison to TTS, TSS has been of limited utility for studying stress relaxation in polymers, and as such has not been widely explored. The general understanding for soft materials is that thermal forces typically play a minor role, at least relative to mechanical ones, in soft glasses, which implies that TSS should be more important in such systems.

Further analogy to TTS appears upon analysis of the strain dependence of the horizontal shift factors. As illustrated in Figure 31, the horizontal shift factors can be described fairly well with functional form given as:

$$\log a_\gamma(\gamma_0) = \frac{-A_1(\gamma_0 - \gamma_{ref})}{A_2 + \gamma_0 - \gamma_{ref}} \tag{13}$$

This functional form is the same as that observed for temperature dependence of the shift factors in TTS. It is interesting to note here that the shifting is required only above γ_0 = 1%, for γ_0 < 1% both the horizontal and vertical shift factors are close to 1, implying that the response of the material is fairly linear in cases when the applied strain is below the yield strain of the material. Also, γ_{ref} obtained from the fitting is found to be 1.6%, which is fairly close to γ_0 = 1%, the reference data set employed for shifting of the frequency sweeps. It is also apparent from the figure that the superposition is obtained primarily by horizontal shifting, and vertical shifting is virtually not required.

The generic rheological features displayed in Figure 29 can be qualitatively retrieved in the framework of the Soft Glass Rheology (SGR) model proposed by Sollich [68, 270]. In this model, any soft glass is represented as a system of independent particles trapped in energy wells (cages) of depth $E(\gamma) = E_0 - k\gamma^2$, produced by interactions with their neighbors. At low strains, E_0

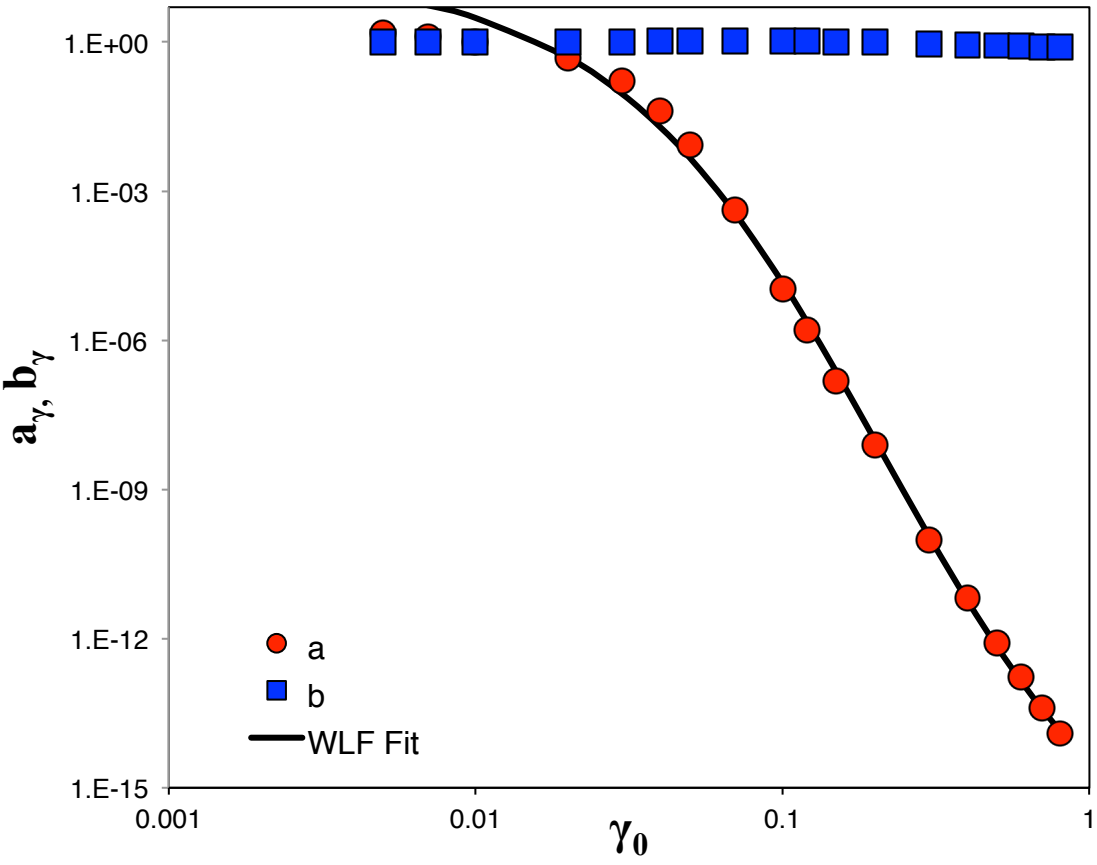

Figure 31 Strain dependence of the horizontal (a_γ) and the vertical (b_γ) shift factors for tethered nanoparticle suspensions with $\phi = 0.26$. The solid line denotes the fit of the WLF form.

is large in comparison to the thermal energy, and the system cannot spontaneously relax to an equilibrium state. The escape probability from the wells is small, proportional to $e^{E(\gamma)/x}$ where x is designated the "effective noise temperature", and plays the role of thermal energy. SGR model therefore produces strain–independent *G'* and *G"* and power–law frequency dependencies at low strains. In the linear regime, the SGR model predicts that *G'* varies as ω^{x-1}. Fitting experimentally determined moduli at low strain with the corresponding SGR model predictions shows that the "effective temperature" for our materials is $x = 1.09$, i.e. close to the glass transition, $x = x_g = 1$. Yielding occurs in the SGR when $E_0 \sim k\gamma^2$, and the cages break–apart under the action of the macroscopic deformation. This leads to a pronounced increase in relaxation processes and hence viscous losses, which as in Figure 29b manifests as a pronounced maximum in $G"(\gamma_0)$. Here we must point out that while this feature is not unique to soft glassy materials, it was first reported in weakly associating polymer gels [271], and reflects enhanced dissipation from strain–induced breakdown of structure and, as such, is analogous to yielding.

The constitutive equations for the SGR model were described in the previous chapter. The stress response from the model to an oscillatory strain of the form $\gamma(t) = \gamma_0 \sin[\omega t]$ was obtained by solving the constitutive equations in MATLAB. Figure 32 shows the behavior of storage and loss modulus as obtained from the calculations for various γ_0 ranging from 1 to 10 for $x = 1.05$. *G'* expectedly decreases with increasing γ_0 and exhibits a stronger dependence on ω, as is observed in the top panel of the figure when going from top to bottom. *G"* exhibits a more complicated behavior with increasing γ_0; at small γ_0 *G"* is nearly independent of γ_0 and increases with increasing γ_0 up till the point when *G'* and *G"* becomes comparable in magnitude. Upon further increase of γ_0, *G"* decreases with increasing γ_0 and exhibits a ω dependence similar to

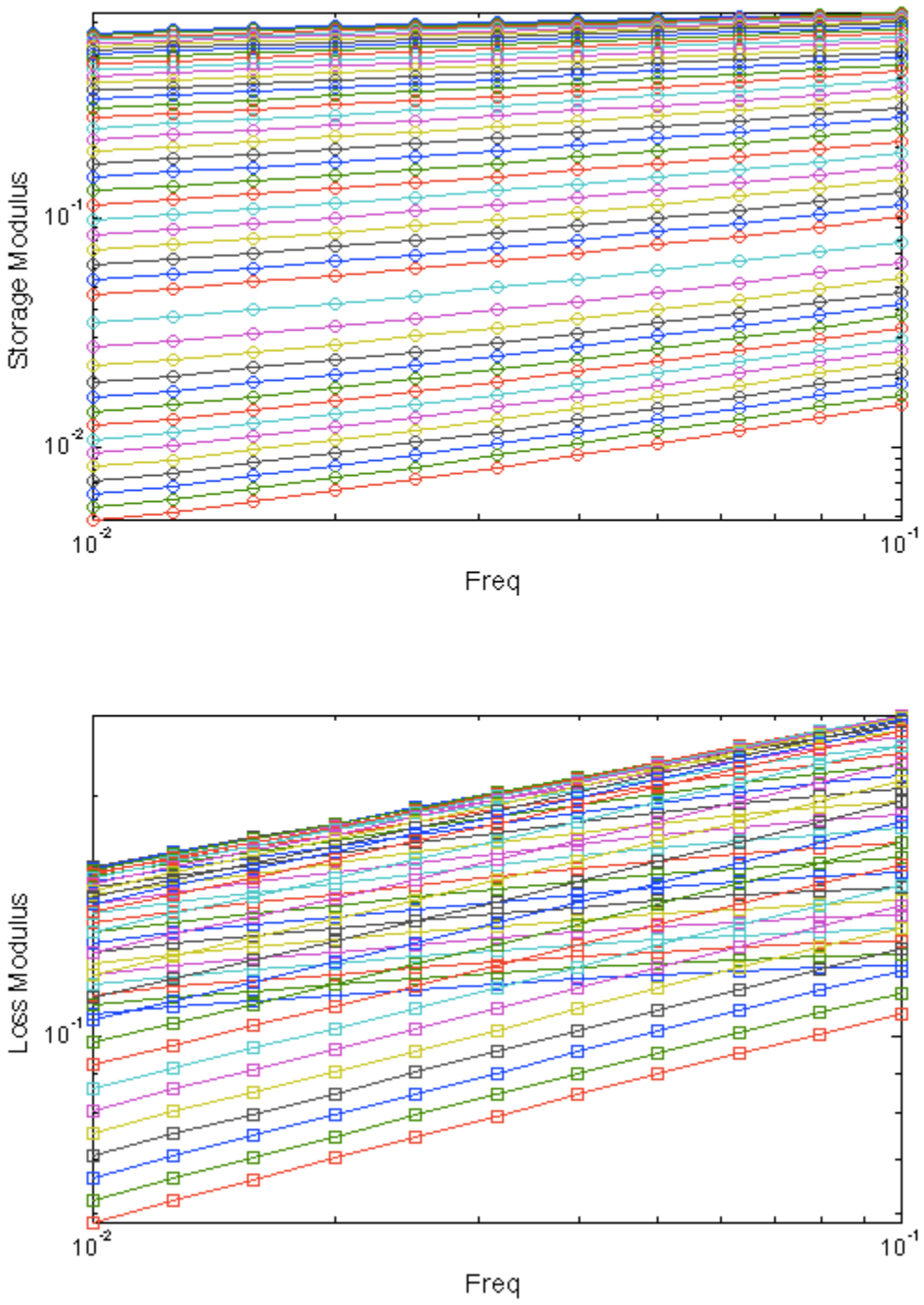

Figure 32 Frequency sweep calculation using the SGR model. Storage (*G'*, top panel) and loss (*G"*, bottom panel) moduli vs. frequency ω for various strain amplitudes γ_0. γ_0 increases from 1 to 10 going from top to bottom in the top panel, *G"* follows a more complicated path with increasing strain as described in text. The calculations were carried out at $x = 1.05$.

that of *G'*. These trends are also in agreement with the maximum that is observed in *G"* in strain sweep measurements close to point of the crossover of *G"* and *G"*, as shown in Figure 29b. Figure 33 shows the shifted storage and loss moduli as obtained from the SGR model calculations for $x = 1.05$. Again, an excellent superposition of the data is obtained by a concomitant horizontal and vertical shifting of the data shown in Figure 32. Figure 34 shows the master curves obtained from the superposition of the *G'* and *G"* data sets for various other x values ranging from 1.1 to 1.9, and all of them are found to exhibit excellent superposition. Lastly, the vertical shift factors a_γ exhibit a WLF like dependence on the strain amplitude as shown by the solid lines in Figure 35a, in accordance with the experimental results illustrated in Figure 31. All these observations decidedly point toward the fact that time–strain superposition is a generic feature that can be described by the SGR model and should be a fundamental feature of all soft glasses describable by the SGR model.

The rheological maps constructed through time–strain superposition can provide insights into the time scale associated with the bulk relaxation processes in the soft glassy materials. The shifting procedure extends the frequency axis to astronomical time scales, and therefore this technique provides for a facile tool to probe the linear response of soft glassy materials at extremely large times. The moduli vs. frequency data were shifted with a reference strain amplitude at which the material response is linear both in experiments and in theory, and therefore the constructed rheological map can be considered to be the linear response of the material across very large time scales. An important time scale that emerges from this superposition is the time corresponding to crossover of the elastic and the loss moduli, which is the inverse of the frequency at which the crossover occurs, $\tau \approx 1/\omega_{cross}$. This time scale is expected to vary strongly with the degree of jamming of the material, and that is indeed observed both in experiments and in the theoretical

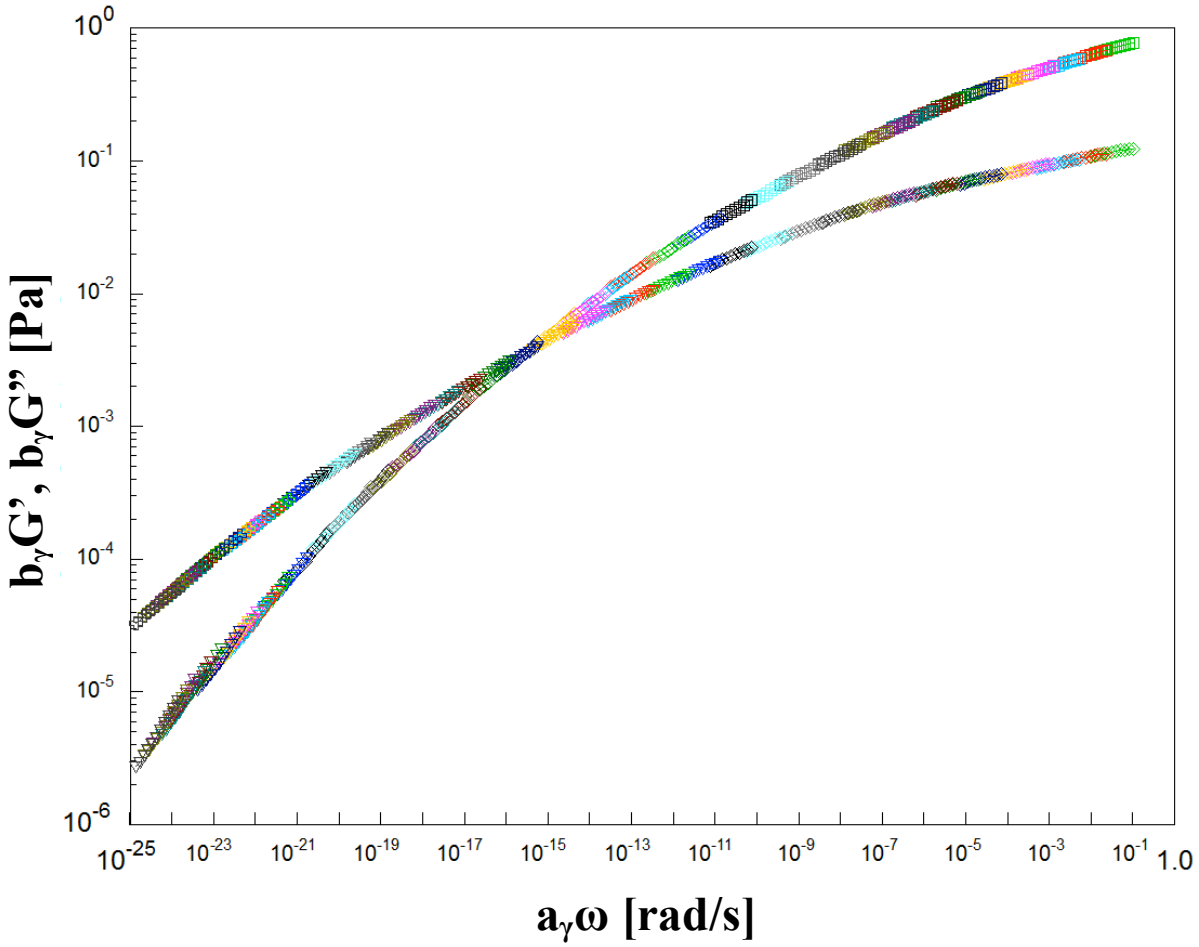

Figure 33 Shifted storage ($b_\gamma G'$, closed symbols) and loss ($b_\gamma G''$, open symbols) moduli vs. shifted frequency $a_\gamma \omega$ as obtained from calculation from the SGR model at $x = 1.05$. *Inset* shows the master curve obtained after the shifting procedure.

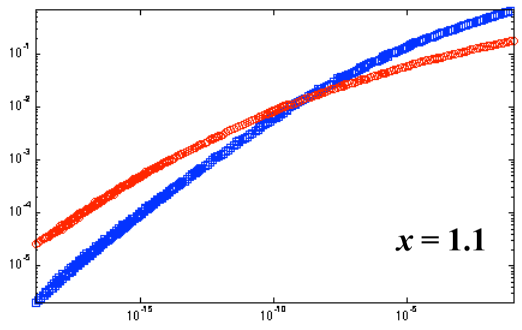
x = 1.1

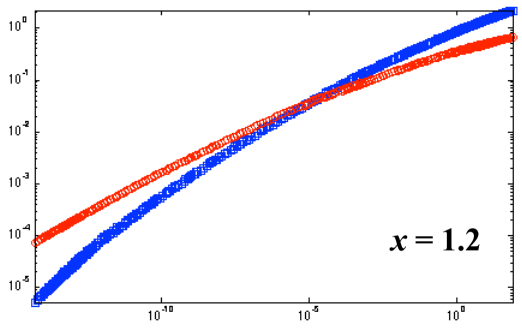
x = 1.2

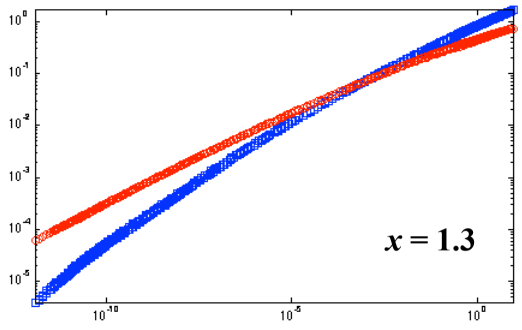
x = 1.3

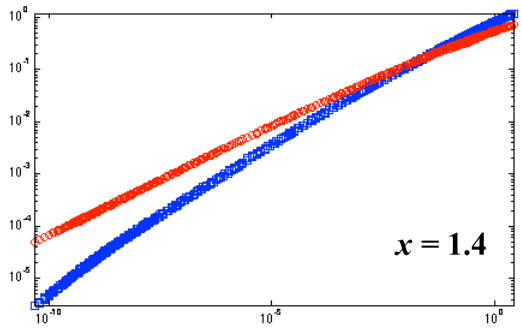
x = 1.4

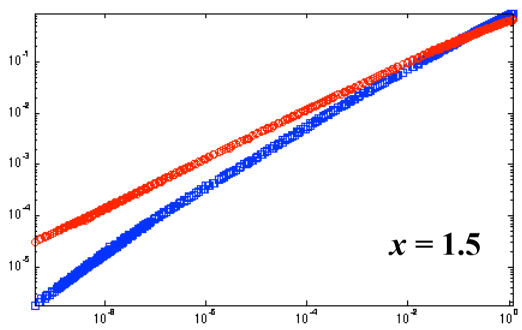
x = 1.5

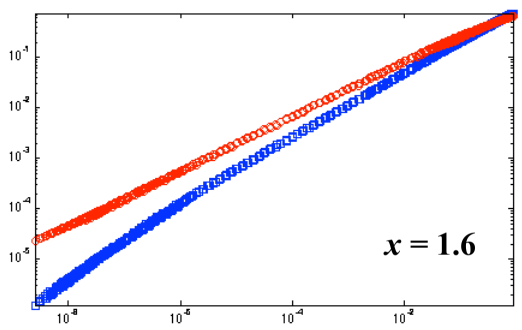
x = 1.6

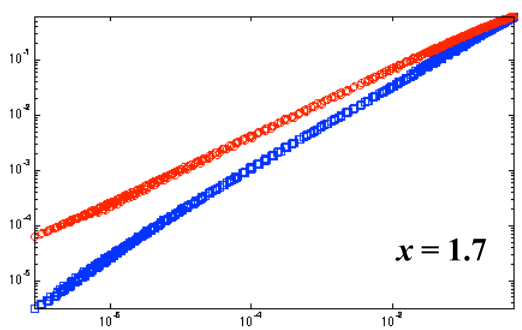
x = 1.7

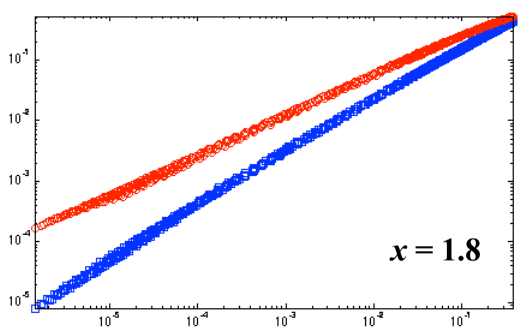
x = 1.8

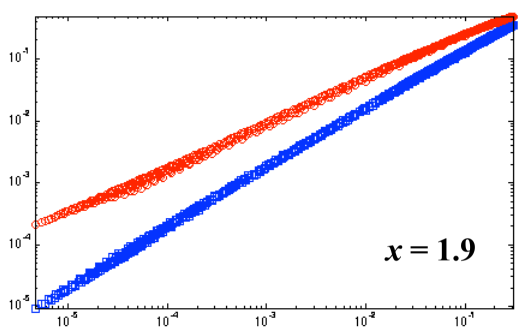
x = 1.9

Figure 34 Master curves obtained after superposition of the shifted *G'* and *G"* data as obtained by solving the SGR model for different values of *x* ranging from 1.1 to 1.9. The vertical axis in all the plots is the shifted $b_\gamma G'$ (blue symbols) and $b_\gamma G"$ (red symbols) and the horizontal axis is $a_\gamma \omega$.

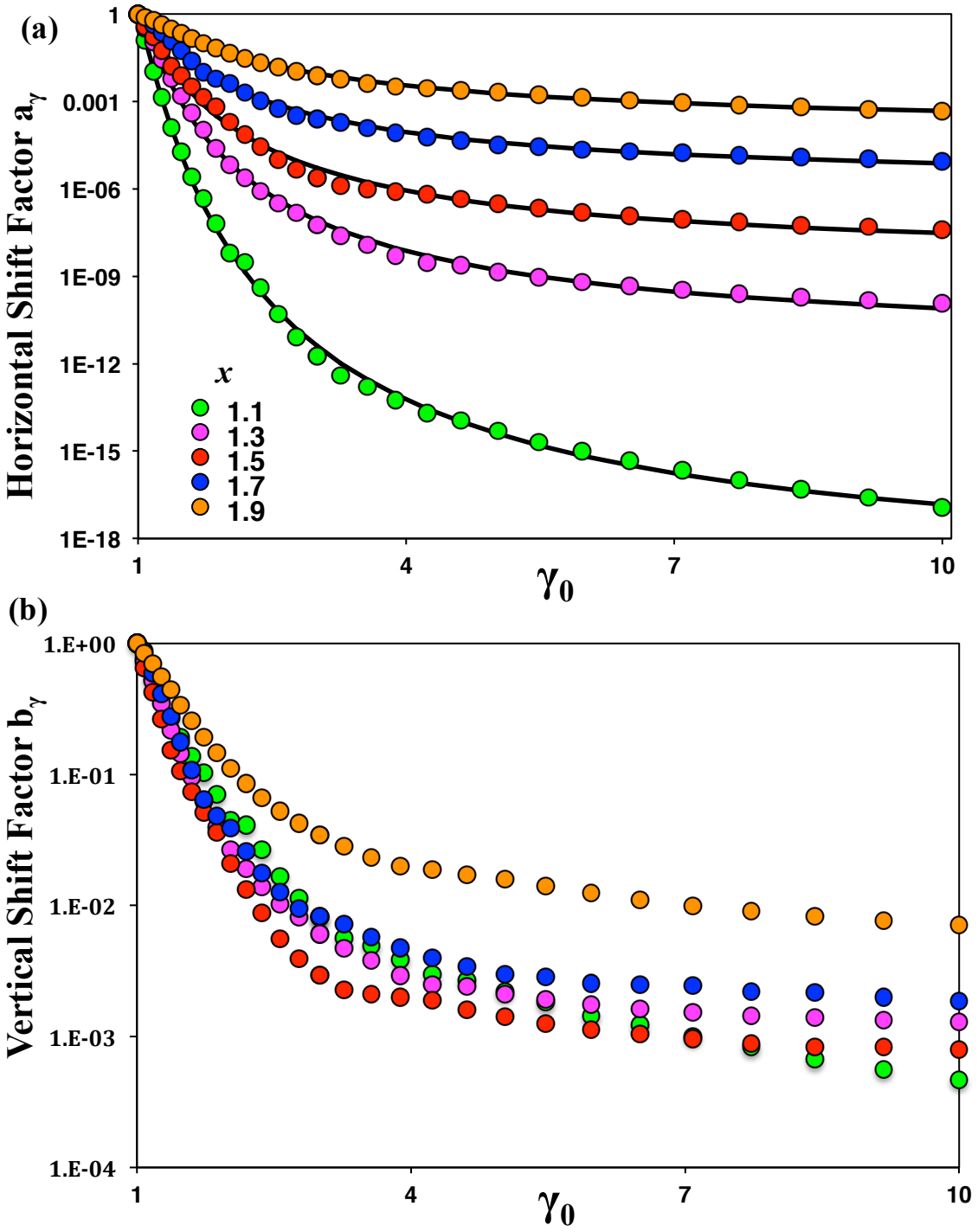

Figure 35 Strain dependence of **a.** the horizontal (a_γ) and **b.** the vertical (b_γ) shift factors for various x values. The solid line denotes the fit of the WLF form in **a.**

calculations. Figure 36 shows the variation of the characteristic time scale τ on the noise temperature x as obtained form the calculation using the SGR model (circles). The noise temperature is a direct indicator of the degree of jamming in a soft glassy material, and therefore the trends in the figure can be understood to reflect upon the fact that glassy materials are expected to exhibit increasingly slower relaxations with increasing degree of jamming (decreasing x). The solid line in the figure indicates the double exponential scaling of τ on x, the origin of this strong scaling is still unclear to us. The figure also includes data from experiments conducted on various other self–suspended nanoparticle fluids [42] as well as oligomer–suspended nanoparticle fluids with varying degree of jamming, and a fair agreement with the theoretical trends is observed for most of the experimental systems.

It is instructive to compare the procedure proposed here with the shear-rate frequency superposition (SRFS) procedure recently reported by Wyss et al. [272]. In SRFS, *G'* and *G"* data obtained for a limited range of frequencies, but at fixed strain rates (instead of shear strains), are superimposed to create master curves covering an extended frequency range. As illustrated in Figure 37a, the master curves obtained using this approach (red curves) are rather different from that obtained from TSS procedure (blue curves). The crossover between *G'* and *G"* occurs at a significantly higher frequency and both *G'* and *G"* exhibit a substantially stronger dependency on shifted ω after the crossover in the SRFS master curves as compared to the TSS master curves. These differences are further highlighted in Figure 37b where a comparison of the complex viscosities ($\eta^* = (G'^2 + G''^2)^{1/2}/\omega$) obtained using both the transformation procedures is presented. It is apparent from the figure that the complex viscosity obtained from SFRS is fairly close to that obtained from the TSS at high frequencies. In the low frequency regime, however, the η^* obtained from SRFS appears to saturate and attain a Newtonian plateau while the η^*

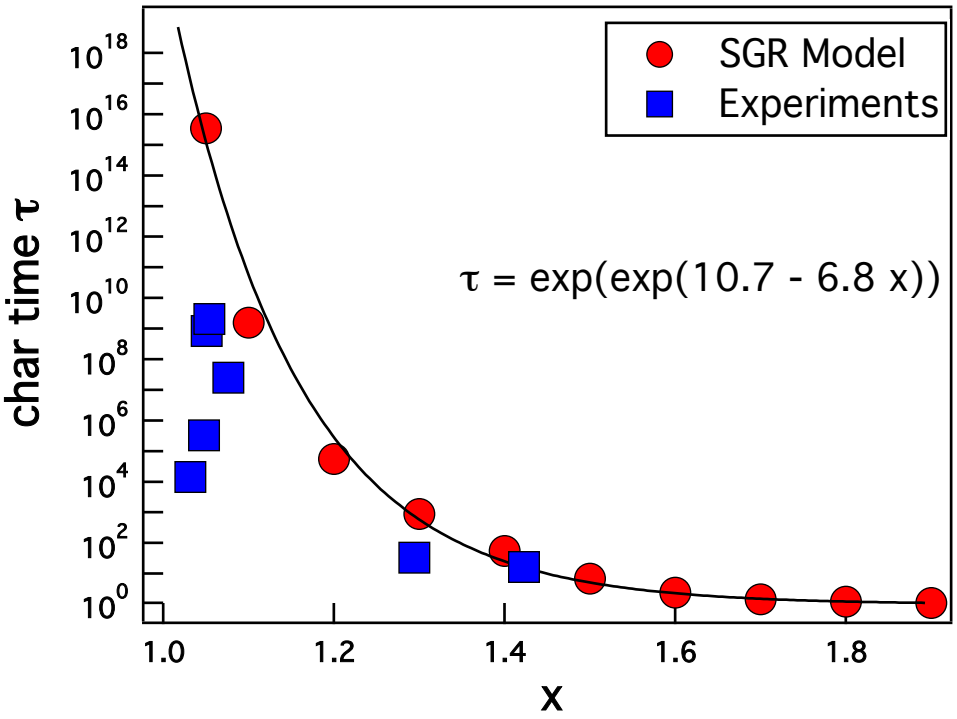

Figure 36 Noise temperature *x* dependence of the characteristic relaxation time τ as obtained from the SGR model and the experiments.

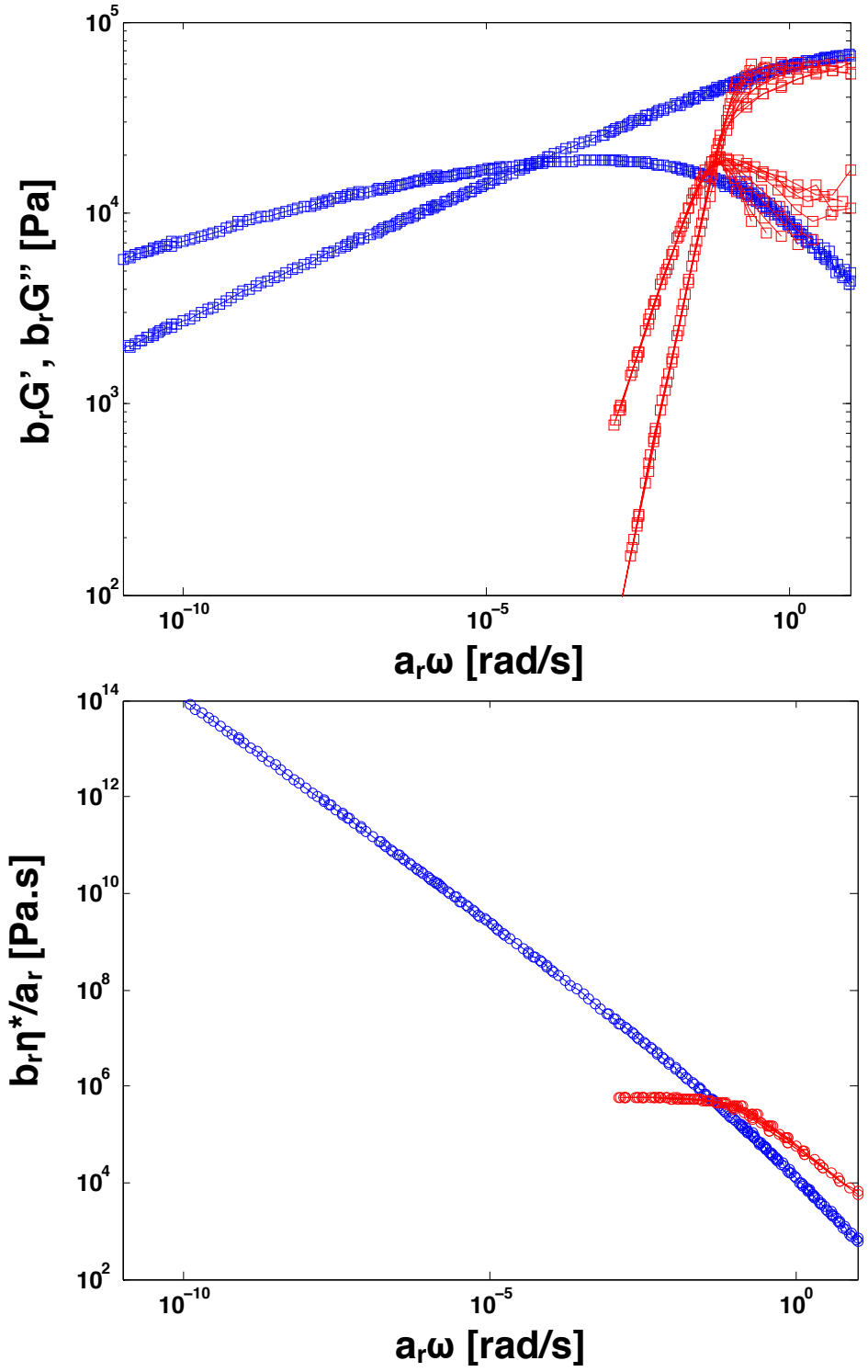

Figure 37 A comparison between TSS (blue symbols) and SRFS (red symbols) shifting procedures. **a.** Shifted storage (b_rG') and loss (b_rG'') moduli and **b.** shifted complex viscosity ($b_r\eta^*/a_r$) vs. shifted frequency $a_r\omega$ for tethered nanoparticle suspensions with $\phi = 0.26$.

obtained from TSS continues to exhibit strong shear thinning trends. These observations underscore the complementary information about a soft glass that can be accessed using SFRS and TSS procedures. Specifically, because yielding is stress-activated, the SRFS measurements facilitate continuous deformation of the materials at stresses above the yield stress; they unsurprisingly produce global yielding, allowing the terminal flow behavior, including the limiting Newtonian viscosity of the soft glass to be quantified. On the contrary, oscillatory measurements carried out at controlled shear strains are unable to maintain large enough stresses in the materials to produce global yielding and alternatively probe the local dynamics within the perturbed cages. Thus, while TSS principle unveils the extended linear viscoelastic response of the soft glassy materials and allows one to recover dynamics in the unyielded reference state, SFRS captures dynamics in a post-yield/un-jammed reference state of a soft glass through extended non-linear viscoelastic measurements.

6.4. Conclusions

Oscillatory rheology was employed to study relaxation dynamics in suspensions of well–dispersed tethered nanoparticle as well as self-suspended tethered nanoparticles. We find that these materials are soft glasses and manifest unusual time–strain superposition (TSS) rheological features. We also show that TSS is a fundamental characteristic of soft glassy solids describable by Sollich's SGR model. Thus, the procedure described here is extremely general and should be instrumental in unveiling the long time response of soft glassy materials. A strong dependence of the relaxation time on the degree of jamming and a comparison with the SRFS technique indicate that the TSS procedure indeed probes the dynamics of the unyielded glassy state, which is nearly impossible to investigate otherwise. Notwithstanding the differences in the vertical shift factors and the role of higher harmonics, the functional form of the horizontal shift factors are found to

bear striking similarities to the WLF equation used in time–temperature superposition (TTS) in amorphous polymers and arguments similar to the free volume arguments used in TTS experiments could be employed to explain the WLF dependence of the shift factors in TSS as well.

CHAPTER 7

POLYMER NANOCOMPOSITES: POLYMER AND PARTICLE DYNAMICS*

Adapted with permission from

D. Kim, S. Srivastava, S. Narayanan, and L. A. Archer, Polymer nanocomposites: polymer and particle dynamics. *Soft Matter* **8**, 10813 (2012).

Abstract

Polymer nanocomposites containing nanoparticles smaller than the random coil size of their host polymer chains are known to exhibit unique properties, such as lower viscosity and glass transition temperature relative to the host polymer melt. These unusual properties are currently hypothesized to result from fast diffusion of the nanostructures in the host polymer, which facilitates polymer chain relaxation by constraint release and other processes. In this study, the effects of addition of sterically stabilized inorganic nanoparticles to entangled *cis*–1,4–polyisoprene and polydimethylsiloxane on the overall rheology of nanocomposites are discussed. In addition, insights about the relaxation of the host polymer chains and transport properties of nanoparticles in entangled polymer nanocomposites are presented. The nanoparticles are found to act as effective plasticizers for their entangled linear hosts, and below a critical, chemistry and molecular–weight dependent particle volume fraction, lead to a reduced viscosity, reduced glass transition temperature, lesser effective number of entanglements, and faster polymer relaxation time. At the nanoparticle length scale, however, the polymer host acts like a simple, ideal fluid and the composites' viscosity rises with increasing particle concentration.

* D. Kim and S. Srivastava contributed equally to this work. D. Kim carried out a part of the sample synthesis and measurements (rheology, dielectric spectroscopy and differential scanning calorimetry) presented in this chapter.

7.1. Introduction

Polymer nanocomposites have attracted consistent research interest for the last few decades. This interest can be traced to the unique material properties such as tensile strength, hardness, refractive index, conductivity, etc. that can be achieved upon homogeneous dispersion of nanoscale fillers into a host polymer of practically any chemistry [1, 32, 35, 41-43, 55, 56, 102, 107, 156, 157, 227, 273]. It is sustained by the broad range of potential applications in diverse fields – electrochemical energy storage, electronics, optics, lubricants, and photovoltaics, that would be enabled by controlled dispersion of nanoparticles in polymers [1, 35, 41, 107, 273]. Uniform dispersion of nanoparticles in polymer hosts is difficult for a variety of reasons, including their affinity towards aggregation owing to attractive van der Waals and polymer mediated depletion attraction forces [227]. A facile approach to mitigate the nanoparticle aggregation is through steric stabilization of the nanoparticles, wherein polymers are absorbed/grafted onto the particle surface, allowing stable dispersions of nanoparticles in versatile media ranging from simple liquids to elastic polymers [41-43, 102, 107].

Recently, nanocomposites containing particles with sizes smaller than the random coil size (R_g), but greater than both the tube diameter (a_T) and the correlation length (ξ) of the entangled polymer host, were reported to exhibit enhanced stability against aggregation [35, 55, 56, 156, 157]. Additionally, these uniform blends of entangled polymers and nanoparticles were shown to exhibit unique properties including *non–Einsteinian* viscous properties, with lower viscosities found in the polymer/particle blends than in the particle–free host polymer, and a decrease in the glass transition temperature (T_g) of the nanocomposite. It has been suggested that the *non–Einsteinian* viscous properties reported in entangled–polymer nanoparticle composites arise from the ability of the diffusing particles to release entanglement constraints between the host polymer

[35, 55, 56]. However, the absence of in–depth investigations of these phenomena, including the effects of nanoparticles on various relaxation processes associated with these systems, has prevented generalization of these ideas.

Herein, we investigate nanocomposites comprised of silica (SiO_2) nanoparticles functionalized with tethered polymer chains and suspended in highly entangled polymer chains with similar chemistry as the tethered polymers. A variety of systems are considered with the tethered/host polymer combinations including *cis*–1,4–polybutadiene (PBD)/*cis*–1,4–polyisoprene (PI), *cis*–1,4–polyisoprene (PI)/*cis*–1,4–polyisoprene (PI) and polydimethylsiloxane (PDMS)/polydimethylsiloxane (PDMS). A range of experimental techniques including mechanical rheology, differential scanning calorimetry (DSC), broadband dielectric spectroscopy (BDS), and X–ray photon correlation spectroscopy (XPCS) are utilized to characterize the effect of the particles on dynamics of their polymer host, and vice versa, in these nanocomposites.

We focus particularly on the SiO_2–PBD/PI nanocomposites for the following reasons: first, PI is a *type–A* dielectric material [46, 274, 275], implying that the polymer has a net dipole moment parallel to its end–to–end vector; PBD in contrast is dielectrically inert. Broadband Dielectric Spectroscopy of these nanocomposites can therefore be used to selectively probe the chain–scale relaxation dynamics of the PI host polymer as influenced by the addition of nanoparticles [46]. Second, the close to zero interaction parameter for a PBD/PI mixture implies negligible enthalpic interaction between the tethered and host polymer [150]. Lastly, higher electron density of the silica core than that of the tethered as well as host polymer allows for facile characterization of the nanoparticle motion through X–ray photon correlation spectroscopy.

7.2. Experimental Methodology: Nanocomposite Synthesis and Characterization

Nanocomposites with precise SiO_2 contents were prepared by mixing tethered SiO_2 nanoparticles with the host polymer. The SiO_2–PBD nanoparticles were synthesized by following a two–step reaction scheme. In the first step, 10 nm SiO_2 nanoparticles (LUDOX^{TM} SM–30, supplied by Sigma Aldrich) were functionalized with sulfonic acid using previously reported procedure [40, 42, 107, 180]. Briefly, an excess of 3–(trihydroxysilyl)–1–propanesulfonic acid (supplied by Gelest Inc.) was added drop–wise at 70ºC to a dilute suspension of the SiO_2 particles in DI water with rapid stirring and the mixture was incubated over night at pH 2. Untethered sulfonic acid molecules were subsequently removed via repeated dialysis of the reaction mixture against DI water and the sodium ions on the particles were removed through ion exchange reactions. The acid functionality of the nanoparticles was determined by titration against standard sodium hydroxide solution.

In the second step, amine–functionalized *cis*–1,4–polybutadiene (PBD) chains (M_w = 3 KDa, M_w/M_n ~ 1.05 and R_g ~ 1.79 nm, supplied by Polymer Source Inc.) were dissolved in tetrahydrofuran (THF) and a stoichiometric amount of sulfonic acid functionalized SiO_2 nanoparticles in DI water was added drop–wise to the solution. The reaction was allowed to proceed over several days to ensure maximal grafting of the chains and the excess PBD chains were then removed by repeated precipitation in a methanol/THF mixture. Finally, the solvents were removed by vacuum drying and the SiO_2 content in the resulting SiO_2–PBD nanoparticles was found to be 11 wt%, as determined by thermogravimetric analysis (TGA) of the nanoparticles (TA Instruments TGA Q500), from which the grafting density (Σ) of the PBD chains was estimated to be 1.9 chains/nm^2. Figure 38a shows a transmission electron micrograph of these SiO_2–PBD particles and it is evident that nanoparticle cores are very well dispersed even

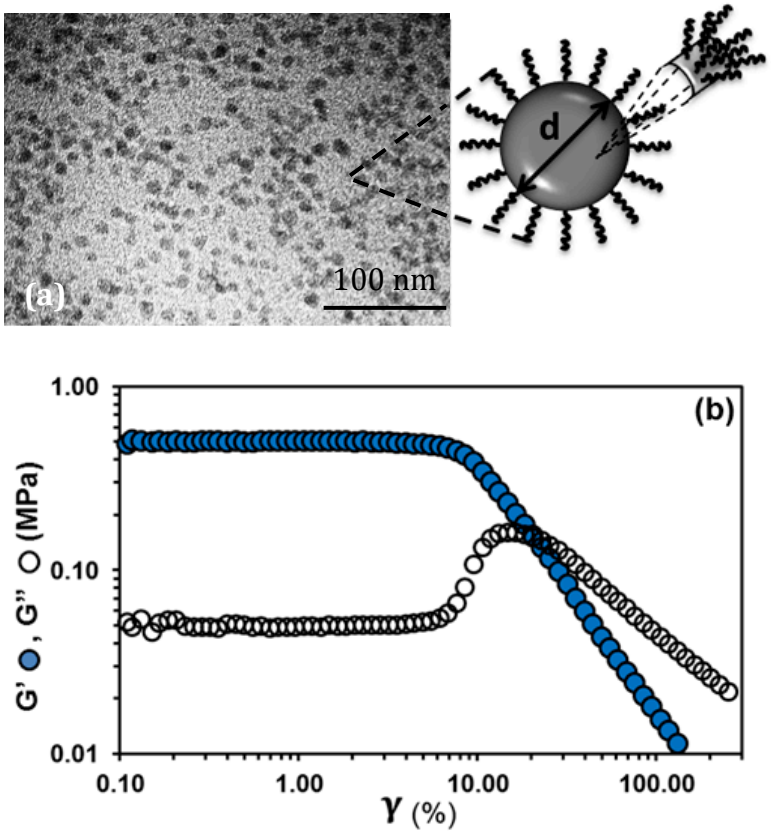

Figure 38 a. Transmission electron micrograph and **b.** Strain–dependent storage, *G',* and loss *G''* moduli for self–suspended SiO_2–PBD nanoparticles at a fixed oscillation frequency $\omega = 10\ s^{-1}$ and temperature = 30°C.

in the absence of any suspending medium. Tethered nanoparticles with such high grafting densities have been shown to be stable against aggregation and exhibit fluid like properties [42, 46, 107]. The strain–dependent rheology of these SiO_2–PBD nanoparticle, as shown in Figure 38b, illustrates the *soft–glassy* behavior of these nanoparticle fluids and further validates the absence of any aggregation in these systems [42, 46]. Further, the low–strain elastic modulus of these nanoparticle fluids is comparable with that of the entangled PI host (not shown here).

SiO_2–PBD/PI nanocomposites were prepared by mixing the suspensions of the SiO_2–PBD nanoparticles in chloroform with *cis*–1,4–polyisoprene (PI) (M_w = 316 KDa, M_w/M_n ~ 1.27, R_g ~ 18.39 nm, supplied by Polymer Source Inc). Chloroform was subsequently removed by vacuum drying to obtain the nanocomposite samples. By adjusting the relative proportion of the two components, nanocomposites with SiO_2 contents ranging from 0.5 wt% to 5.5 wt% were synthesized. Similar procedures were employed to synthesize SiO_2–PI/PI (Σ ~ 2.8 chains /nm^2) and SiO_2–PDMS/PDMS (Σ ~ 1.1 chains /nm^2) nanocomposites with variable nanoparticle contents.

7.3. Results and Discussion

7.3.1. Mechanical Rheology

The effect of nanoparticles on the host polymer viscosity were characterized through steady–shear measurements performed at shear rates performed at shear rates ($\dot{\gamma}$) in the range 5×10^{-4} s^{-1} $\leq\dot{\gamma}\leq$ 5×10^{-2} s^{-1}. These measurements were carried out at 30° C using a Rheometrics ARES rheometer outfitted with 10 mm diameter parallel plate fixtures and were repeated multiple times to obtain better statistics. A Newtonian plateau at low shear rates is observed for all the SiO_2–PBD/PI nanocomposites, as shown in Figure 39a, which ultimately gives way to shear thinning

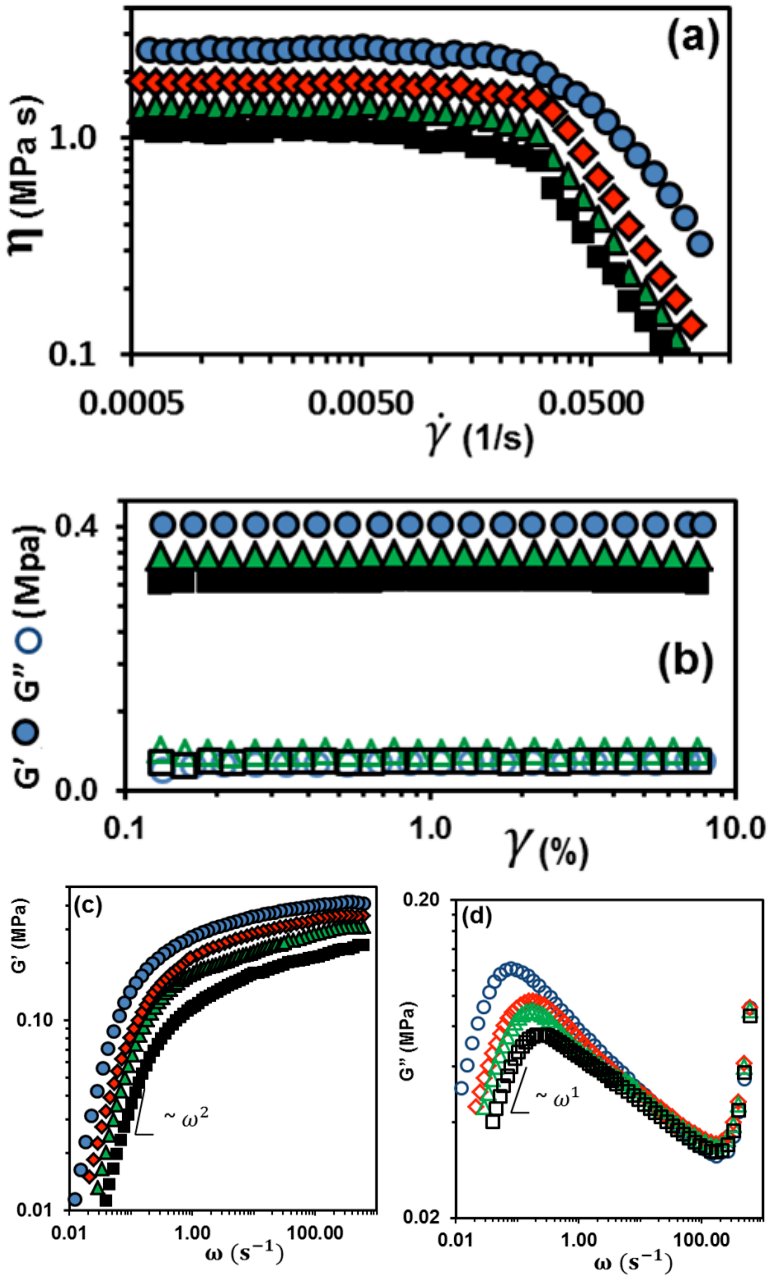

Figure 39 Rheological properties for SiO_2–PBD/PI nanocomposites at various nanoparticle loadings – circles: $\phi = 0$, diamonds: $\phi = 1\%$, triangles: $\phi = 3\%$, and squares: $\phi = 5\%$. **a.** Viscosity versus shear rate; **b.** Storage modulus, *G'*, and loss modulus, *G"* versus strain amplitude γ; **c.** *G'* vs. oscillation frequency ω; and **d.** *G"* vs. ω.

behavior at high rates. Further, in agreement with recent studies [35, 55, 57, 156, 157], Figure 39a clearly shows that the viscosity $\eta(\dot{\gamma})$ of the SiO_2PBD/PI (3K–PBD/316K–PI) nanocomposites decreases as the particle content increases. Figure 40a shows that the relative zero–shear viscosity η_r ($\equiv \eta_{0,NC}/\eta_{0,P}$) of the SiO_2PBD/PI nanocomposites (NC) are not only lower than 1 but also decreases as the SiO_2 core volume fraction (ϕ) rises. This behavior is in complete contrast to the classical predictions by Einstein's [276] and Batchelor's [277], where the relative viscosity of a suspension of particles is predicted to rise at least linearly with the volume fraction of suspended particles.

Figure 40b shows results for various other nanocomposites, all of which show similar *non–Einsteinian* initial depression of the host polymer's viscosity upon addition of nanoparticles. For comparison, η_r vs. ϕ trends for a SiO_2–0.9KPDMS/0.95KPDMS nanocomposite are also included in the figure. For this case, the host polymer is unentangled and its random–coil size (R_g ~ 0.77 nm) is substantially lower than the radius of the SiO_2 nanoparticle cores. This material exhibits a relative viscosity that rises in proportion to the ϕ, consistent with expectations for a suspension of particles. Also, unlike the SiO_2–PBD/PI nanocomposite, for which η_r decreases continuously with ϕ in the range studied, all of the other materials show an initial decrease at low ϕ which is followed by a more conventional *suspension* regime in which η_r increases with ϕ. Further inspection of the results indicate that the nanoparticle composition range where the *non–Einsteinian* behavior is observed shrinks as the molecular weight of the polymer host is reduced and as the effective hardness (SiO_2 particle size/corona thickness) of the nanoparticles becomes greater.

Strain dependent oscillatory shear measurements at a fixed oscillation frequency $\omega = 10\ s^{-1}$ and over a broad range of shear strains (γ) were also performed on the SiO_2–PBD/PI nanocomposite

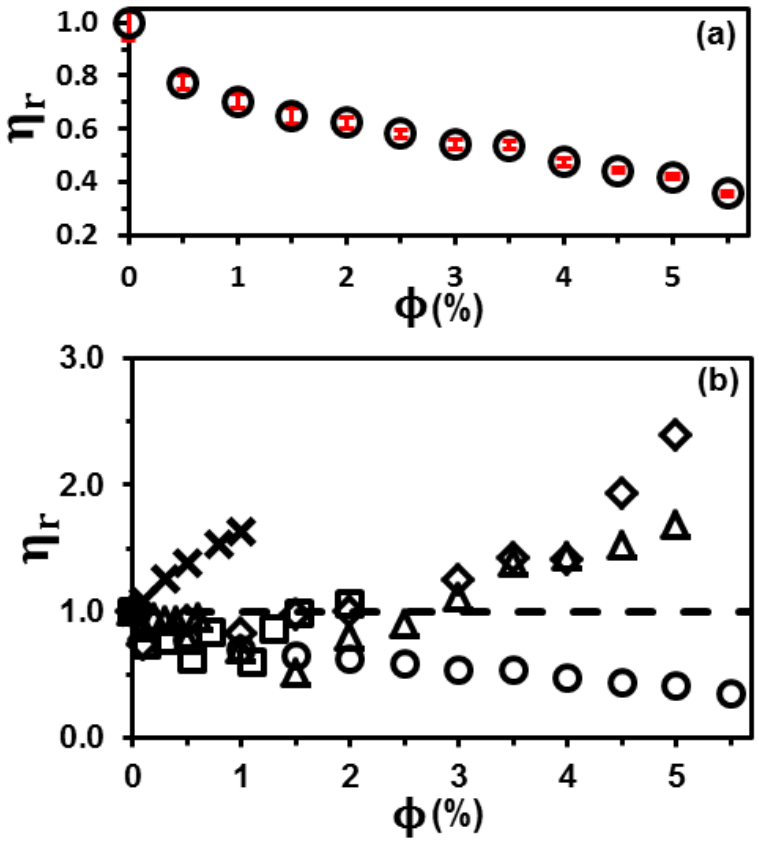

Figure 40 Plot of η_r vs. ϕ for various nanoparticle/polymer composites: (a) SiO_2–3KPBD/316KPI; (b) X: SiO_2–0.9KPDMS/0.95KPDMS; squares: SiO_2–0.5KPI/304KPI; diamonds: SiO_2–C12/304KPI3; triangles: SiO_2–0.9KPDMS/308KPDMS; circles: SiO_2–3KPBD/316KPI.

using an Anton Paar MCR 301 rheometer, as shown in Figure 39b. In conjunction to the *non–Einsteinian* viscosity decrease in $\eta(\dot{\gamma})$, we also observe a significant decrease in the zero– and finite–strain rubbery plateau modulus, $G_{e,0}$ ($\equiv G'_{\gamma\to 0}$) with increasing ϕ. We would like to specifically point out that these observations are in contrast to previous reports on non–Einsteinan trends in viscosity, where negligible changes in G' were reported [55, 56, 157]. These measurements were complemented by frequency–dependent oscillatory shear measurements at low shear strain (γ = 0.01) to obtain the limiting linear viscoelastic properties for the nanocomposites (Figure 39c & Figure 39d). It is noteworthy from Figure 39d that the loss maximum progressively becomes more depressed and drifts to higher frequency with increasing ϕ. Together, these observations suggest that the addition of nanoparticles disrupts / dilates the polymer network and increases the effective entanglement molecular weight M_e ($= \rho RT/G_{e,0}$), as depicted in Figure 41a.

7.3.2. Nanoparticle Effects on Glass Transition

Further insights into the influence of nanoparticles on the entanglement structure of their host was obtained from glass transition temperature (T_g) trends, estimated from Differential Scanning Calorimetry (DSC) (Figure 42). These measurements were carried out at a fixed temperature ramp rate of 5 K/min in a nitrogen environment using a TA Instruments DSC Q2000. As illustrated in Figure 41b, the T_g of nanocomposite decreases progressively with increasing amount of SiO_2–PBD nanoparticle concentration. The T_g for a polymer blend can be estimated using the Fox relation [278], $1/T_g = \Sigma_i\, m_i/T_{g,i}$, where m_i and $T_{g,i}$ are mass fraction and T_g of each of the blend components. The dashed line in the figure is Fox relation estimate under the assumption that all of PBD chains tethered to the particles participate in plasticization of the host polymers. Clearly, the theoretical estimate yields a much larger T_g decrease than what is

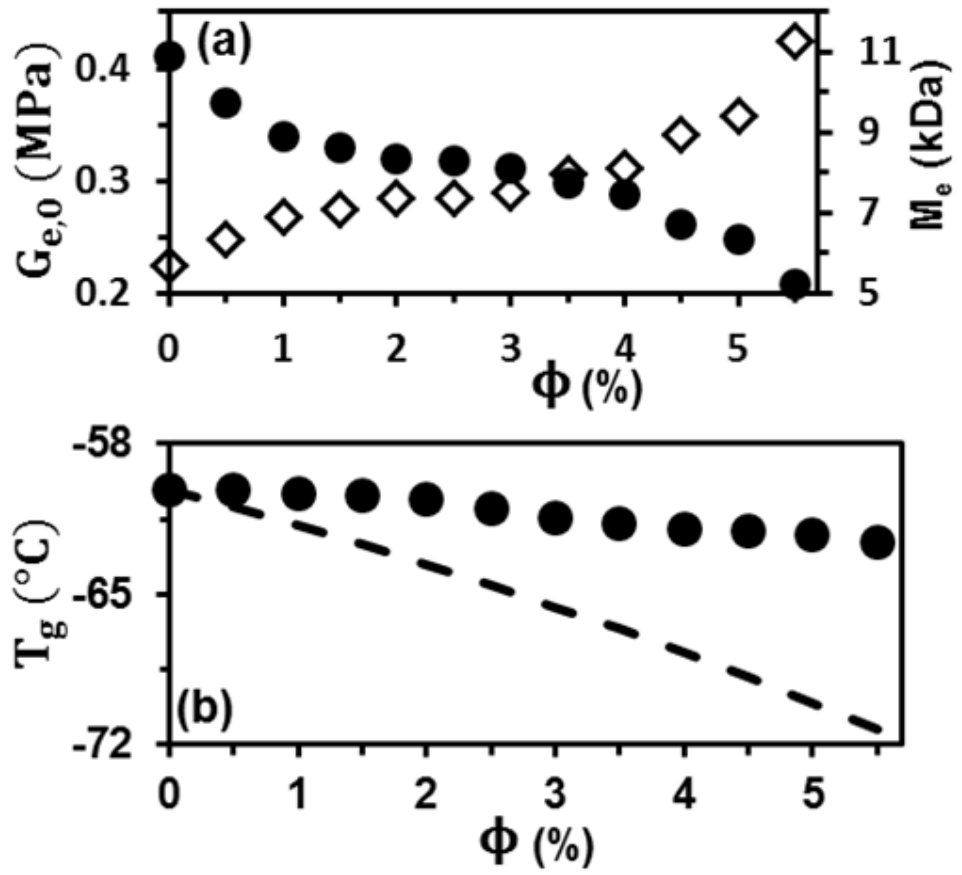

Figure 41 a. Plateau modulus ($G_{e,0}$) and corresponding M_e vs. ϕ (closed and open symbol, respectively) and **b.** T_g vs. ϕ for SiO_2–PBD3k/PI316k nanocomposites. The dotted line denotes the T_g values computed using the Fox relation.

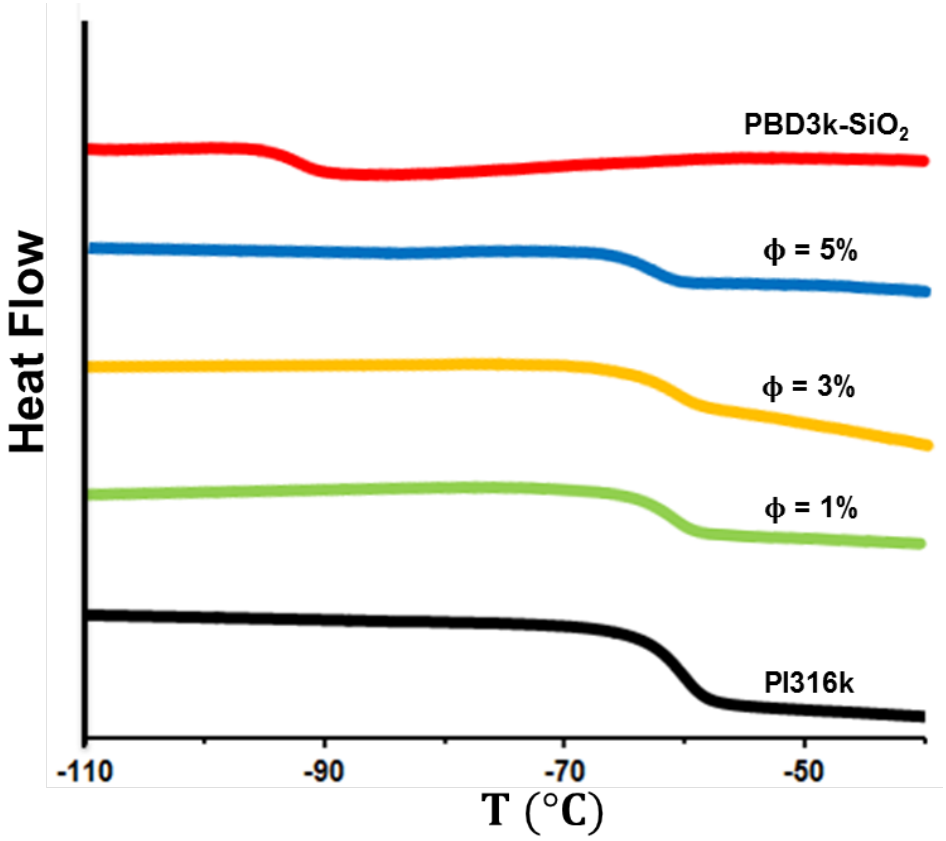

Figure 42 DSC thermograms for PI316k, ϕ = 1%, 3%, 5% SiO_2–PBD3k/PI316k nanocomposites, and PBD3k–SiO_2. Curves are shifted along vertical axis to enhance clarity.

observed in the experiments. This leads us to believe that only a fraction of the PBD chain segments (presumably those near the unattached ends) participate in plasticization of the PI host and are responsible for the majority of the observed effects.

An alternate way to quantify the extent of plasticization in these systems is through the normalized entanglement molecular weight, M_e/M_{e0}, which is calculated from the measured plateau modulus as $M_e/M_{e0} = \rho RT/M_{e0}G_{e,0}(\phi)$. Here M_{e0} is the entanglement molecular weight of the host PI. As illustrated in Figure 43, M_e/M_{e0} rises with increasing ϕ (diamonds), implying progressive disentanglement of the host PI. M_e/M_{e0} can also be compared to theoretical estimates of the normalized entanglement molecular weight computed using the formula, $M_e/M_{e,0} = \varphi^{-4/3}$, φ being the effective polymer volume fraction. The two situations presented in Figure 43 correspond to the cases where φ is computed assuming (i) all PBD chains tethered to the nanoparticles are involved in plasticizing the host PI (circles); and (ii) only a fraction of the tethered PBD chains, computed from applying the Fox relation to the experimental T_g data (squares). It is evident from Figure 43 that although scenario (ii) is in better accord with the estimates from rheology measurements, although the agreement is quite far from being quantitative.

7.3.3. Broadband Dielectric Spectroscopy and Host Polymer Relaxation Dynamics

The novelty of the nanocomposites considered in this study lies in our ability to probe at the normal mode or end–to–end vector relaxation time of host chains systematically as influenced by the addition of the nanoparticles. Normal mode relaxation time (τ_p) of the host PI chains was characterized using a Novocontrol broadband dielectric spectrometer outfitted with sandwich–type gold–plated copper measurement fixtures. Dielectric loss spectra in the frequency range of

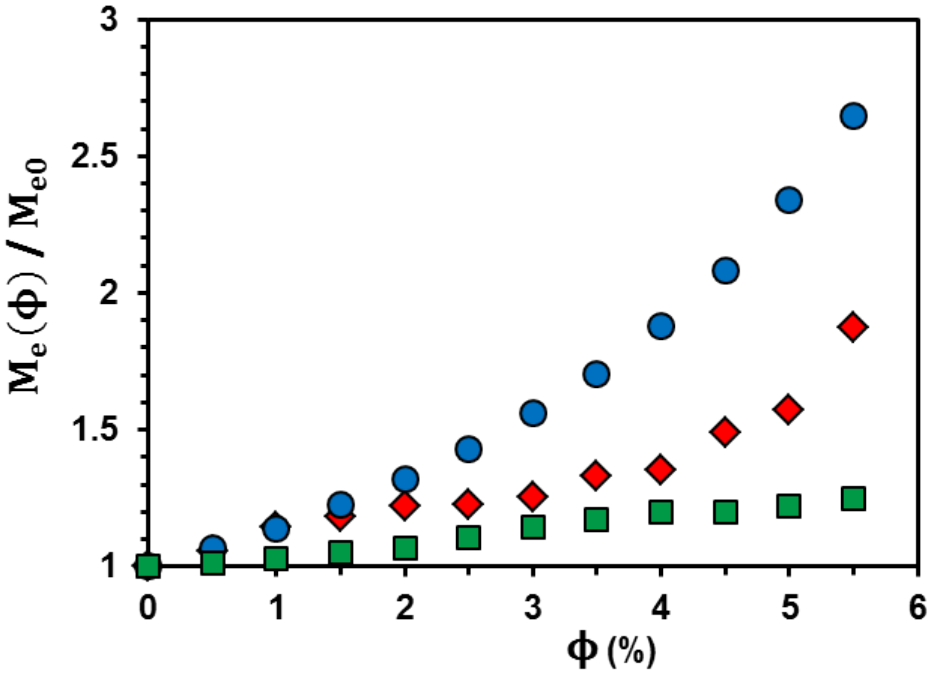

Figure 43 Normalized entanglement molecular weight, M_e (φ)/M_{e0} vs. ϕ for SiO_2–PBD nanocomposites obtained from oscillatory amplitude sweep measurement (diamonds). Also, M_e (φ)/M_{e0} estimates assuming (i) all PBD chains act as plasticizer (circles) and (ii) an effective amount of PBD calculated from T_g measurement act as plasticizer (squares). M_{e0} is the entanglement molecular weight for pure PI.

10^{-2} to 10^{7} Hz at temperatures ranging from –60ºC to 130ºC were obtained using a quartz cryosystem with a nitrogen gas stream. Figure 44 reports the terminal relaxation time ($\tau_p \sim 1/2\pi f_p$) of PI chains with increasing loading of SiO_2–PBD nanoparticles, as estimated from the low frequency (f_p) maximum in the dielectric loss spectra (Figure 45). Clearly, τ_p of the PI host decreases markedly upon addition of nanoparticles at all temperatures, indicating a speeding up of chain relaxation upon nanoparticle addition. Also, τ_p is found to be a strong function of temperature.

Further insights into the chain relaxation processes are obtained by fitting the relaxation data with the Vogel–Fulcher–Tamman (VFT) equation [279],

$$\tau_p = A \exp \frac{B}{T - C} \tag{14}$$

as shown with dashed lines in Figure 44. Here A is the high temperature limit of the relaxation time, B is the activation energy, T is the absolute temperature and C is the Vogel temperature. Values of these fitting parameters are summarized in Table 2. Both A and B decrease as the nanoparticle loading is increased, but the Vogel temperature (C) changes very little upon addition of nanoparticles to the host polymer. The Doolittle equation [150], $\eta \sim \exp(B/f)$, provides a conventional approach for relating the viscosity (η) to the activation energy (B) and free volume (f) of a material; $f \propto (T - C)$. The fact that C is essentially unaffected by particle loading implies that the effect of the nanoparticles on T_g is not likely a result of an increased free volume due to the presence of nanoparticles or to the large numbers of ends introduced by the nanoparticle–tethered PBD chains [280]. Rather, the particles appear to reduce the activation barrier, B, for motion of the host, which for an entangled polymer manifests as a reduction of the number of entanglements, N_e (= M_w/M_e) per chain, consistent with our earlier conclusion from

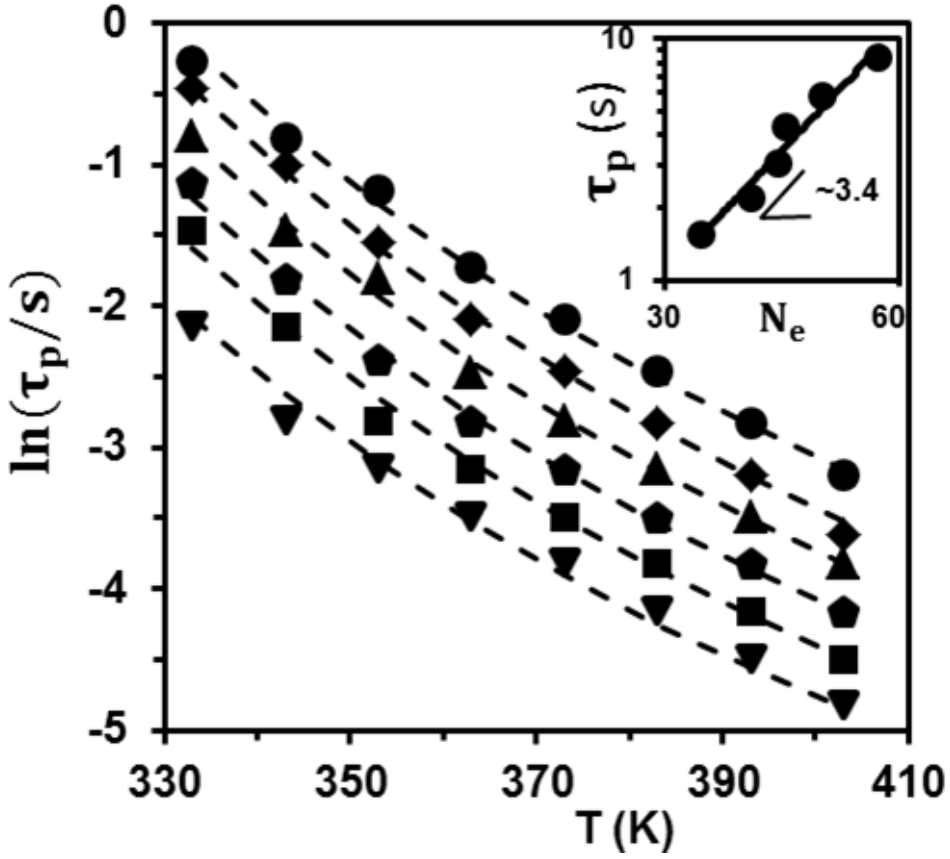

Figure 44 Temperature dependence of PI relaxation time (τ_p) for SiO_2–PBD/PI nanocomposites deduced from the low–frequency dielectric loss maxima at various ϕ (circle: ϕ = 0, PI316k, diamond: ϕ = 1%, triangle: ϕ = 2%, pentagon: ϕ = 3%, square: ϕ = 4%, and inverted triangle: ϕ = 5%). Dotted lines are VFT fits to the data. *Inset* is a log–log plot of τ_p vs. N_e at 30°C.

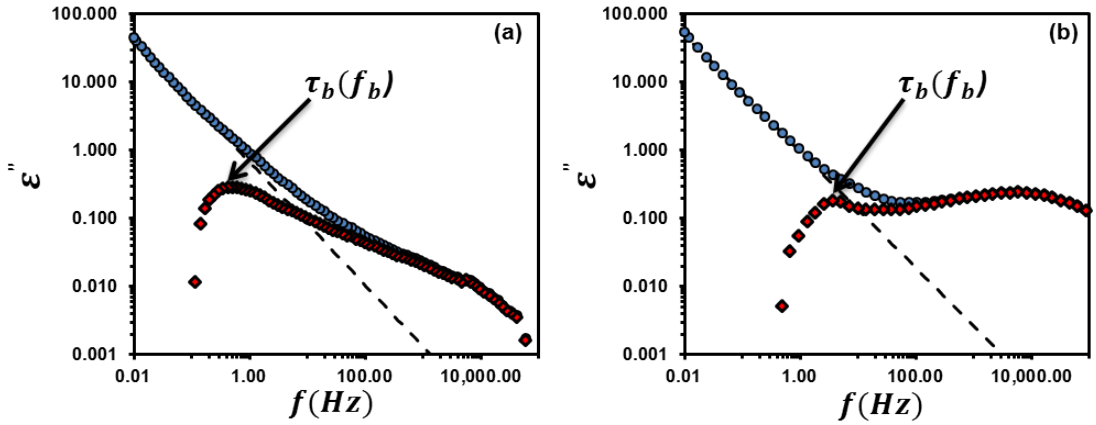

Figure 45 $\varepsilon''(f) = \varepsilon''_d(f) + \varepsilon''_c(f)$ calculation for **a.** PI316k and **b.** ϕ = 5% SiO_2–PBD nanocomposites. Circle symbol represents $\varepsilon''(f)$, dotted line represents $\varepsilon''_c(f)$ drawn from low frequency, and diamond symbol represents $\varepsilon''_d(f)$ which was used to find $\tau_p = (2\pi f_p)^{-1}$ where f_p corresponds to maximum in the dielectric loss spectrum, $\varepsilon''_d(f)$.

Table 2: VFT fit parameters for SiO_2–PBD/PI nanocomposites.

ϕ(%)	A	B	C
0	–9.7	1466.5	179
1	–10.1	1460.0	182
2	–10.3	1430.2	182
3	–10.5	1395.4	181
4	–10.75	1384.1	182
5	–10.81	1320.0	181

the $G_{e,0}$ data. Again, M_w is the molar mass of the PI host and M_e is the entanglement molecular weight computed from $G_{e,0}$. Further, as shown in the inset of Figure 44, τ_p is found to scale as $N_e^{3.4}$, as is expected for long entangled chains [150]. This provides a direct connection between the rheology data and relaxation experiments, and further confirms our hypothesis that addition of nanoparticles leads to dilation of the entanglement network and speeds up chain relaxation, which is in turn responsible for the lower viscosity of the nanocomposites as compared to the polymer host.

7.3.4. X–ray Photon Correlation Spectroscopy and Nanoparticle Motion

Finally, we present our investigations on the motion of the SiO_2 nanoparticles in the host polymer and the role they play in the phenomena discussed above. Relaxation processes associated with the nanoparticles are investigated using X–ray photon correlation spectroscopy (XPCS), where the temporal evolution of the X–ray scattering patterns from the nanocomposites reveal information about the dynamics of the silica core of the nanoparticles. XPCS measurements were performed at Sector 8–ID at the Advanced Photon Source (APS) across a range of the wave vector (q) using 7.35 keV X–rays. Instrumental specifications can be found elsewhere [281]. The normalized intensity–intensity autocorrelation function ($g_2(q,t)$), obtained from XPCS measurements, is related to the intermediate scattering function (ISF, $f(q, t)$) [281] as

$$g_2(q,t) = 1 + b\left[f(q,t)\right]^2 \tag{15}$$

Here, b and t are the instrument dependent Siegert factor (~ 0.4), and the delay time respectively. Numerous studies [281-283] have reported that the ISF, and consequentially $g_2(q,t)$, are best described by a stretched/compressed exponential functions of the form

$$f(q,t) = \exp\left[-\left(t/\tau_n\right)^{\beta}\right] \tag{16}$$

with τ_n and β denoting the q dependent relaxation time and the stretching/compression exponent of the ISF. The bottom inset in Figure 46a shows typical $g_2(q,t)$ at q = 0.09 nm^{-1} for a nanocomposite with ϕ = 1%. The $g_2(q,t)$ results shown here, as well as for other nanocomposites, were fitted with the functional forms described by Eq. (2) and (3), and is shown as the solid line in the inset. β was found to vary between 1.5 and 2 with q for all the systems with no specific trends, indicating a compressed exponential relaxation and signifying a comparatively faster decay of the $f(q,t)$. Such a compression of the relaxation is commonly seen for nanoparticle motion in glassy media and has been attributed to the non–equilibrium forces present in the glassy, non–ergodic systems [70, 71]. As shown in Figure 46a, τ_n follows a decidedly q^{-1} scaling for all the nanocomposites studied, indicating that the nanoparticle cores are hyperdiffusive in the entangled polymer host. Similar observations have been reported in many other systems ranging from thin films to suspensions, where the nanoparticle diffusion is restricted due to an entangled host or jamming [70, 71, 281-283]. We believe that such hyperdiffusive motion of the nanoparticles cores arises from their hopping between the cages formed by the entangled polymer around them. Additionally, as illustrated in the top inset for Figure 46a, at any q, τ_n increases with nanoparticle loading.

Balancing the viscous resistance on a hyperdiffusive nanoparticle with the Brownian force (kT/a) it experiences by collisions with surrounding molecules, $6\pi\eta_{micro}va = kT/a$, it is possible to estimate the effective/micro viscosity (η_{micro}) the nanoparticles experience in the host polymer. Here v (= $q\tau_n$) is the average particle velocity determined from the XPCS measurement [282], a is the particle radius and k is the Boltzmann constant. Surprisingly, in contrast to bulk viscosity (η), η_{micro} is found to be a linearly increasing function of particle volume fraction with a slope of

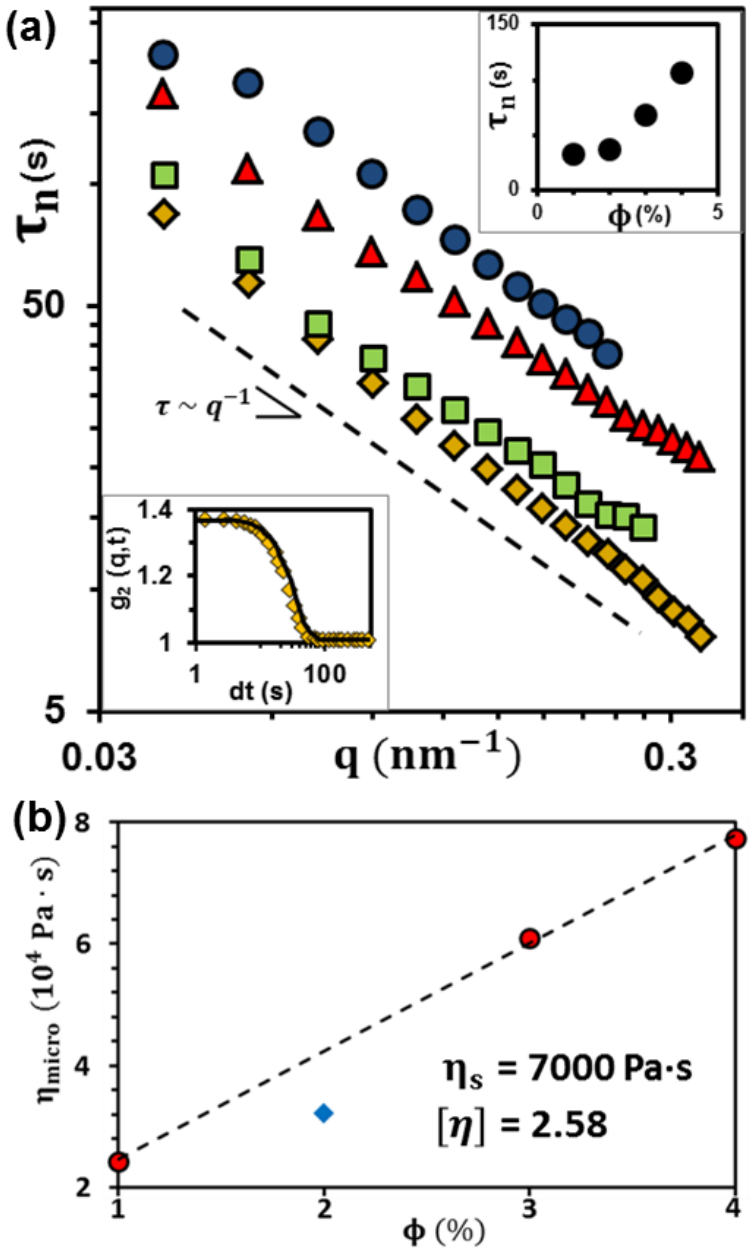

Figure 46 a. τ_n vs. q and b. η_{micro} vs. ϕ for SiO_2–PBD/PI nanocomposites. In a., lower *inset*: g_2 (q,t) vs. t for ϕ = 1% and upper *inset*: τ_n vs. ϕ. Symbols correspond to: diamonds: ϕ = 1%, squares: ϕ = 2%, triangles: ϕ = 3% and circles: ϕ = 4%. In b., the dotted line is a fit of the form $\eta = \eta_s (1 + [\eta]\phi)$ for 3 data points shown as circles only.

2.58 (Figure 46b), which is very close to Einstein's result [276] for intrinsic viscosity η (= 2.5) of hard spheres.

A competition between two effects with increasing ϕ where increasing nanoparticle crowding hinders an individual nanoparticle motion while the fraction of tethered chains participating in the plasticization of the polymer host progressively decreases can be attributed to explain the opposing trends in η_{micro} and η (see Table 3). While the former dominates η_{micro} even at the lowest particle loading considered, its effects on η are much less dramatic. However, we expect the particle crowding effects to eventually supersede the plasticization effects from the PBD chains and lead to an upturn in the bulk viscosity as well, as is observed for nanocomposites with particles having smaller corona (Figure 40b).

7.4. Conclusions

In conclusion, we have discovered that nanoparticles with densely grafted polymer chains act as effective plasticizers when suspended in well–entangled polymer hosts. The level of plasticization is a weak function of the nanoparticle volume fraction, which is interpreted to mean that only a fraction of each grafted polymer chain participates in producing the effect. Both the number of entanglements per host chain and the glass transition temperature of the host polymer are found to decrease upon particle addition. Further, the end–to–end vector relaxation time of the host chains is found to decrease in a manner consistent with theoretical estimates for solvent–dilation of the entangled polymer network. Characterization of the microscopic motion of the particles in the host reveals that nanoparticle motions in entangled polymers are hyperdiffusive, but that the particles experience their environment as a local viscosity, substantially smaller than the bulk viscosity of the host polymer, which increases proportionately with the volume fraction of particles in the nanocomposites. As a first step towards connecting

Table 3: Number of entanglement per chain (N_e), tube diameter (a_T), drift velocity of particle (v), microscopic viscosity (η_{micro}) and bulk viscosity (η) for SiO_2–PBD/PI nanocomposites.

ϕ(%)	N_e	a_T (nm)	v (nm/s)	η_{micro} (MPa s)	η (MPa s)
1	45.8	5.7	0.36	0.02	1.79
2	43.0	5.5	0.28	0.03	1.59
3	42.0	5.4	0.15	0.06	1.38
4	38.9	5.2	0.11	0.08	1.22

the strikingly different influences of nanoparticles on the macro– and microscopic viscosity in these composites, we contend that they stem from a balance between two principal effects. First, increasing the loading of sterically stabilized nanoparticles in the composites increases the tethered corona content, which plasticizes the host polymer, increases its entanglement spacing, and lowers the viscosity, chain relaxation time, and plateau modulus. In contrast, increasing the particle content in the composites enhances crowding, which inhibits particle motion and causes progressive increase in the particle relaxation time.

CHAPTER 8

TRANSPORT ANOMALIES IN SOFT COLLOIDS

Partly adapted with permission from

S. Srivastava, L. A. Archer, and S. Narayanan, Structure and transport anomalies in soft colloids. *Physical Review Letters* **110**, 148302 (2013).

Abstract

Anomalous trends in nanoparticle motion are reported in soft nanoparticle suspensions using dynamic X–ray scattering measurements. Contrary to normal expectations, and in conjunction to anomalous decrease in particle–particle correlations with increasing particle volume fraction as reported in Chapter 4, we find that particle dynamics become faster as volume fraction rises above a critical particle loading associated with particle overlap. Our observations bear many similarities to the cascade of structural and transport anomalies reported for complex, network forming molecular fluids such as water, and are argued to share similar physical origins.

8.1. Introduction

Increasing the concentration of particles in a dilute suspension normally decreases the space available for placing new particles, which lowers the configurational entropy, increases correlations between the particle centers and slows down particle motion. In this Chapter we report the dynamics of suspensions of soft, oligomer–grafted nanoparticles dispersed in a fluid chemically identical to the attached chains. We find that the suspensions exhibit anomalous properties wherein inter–particle correlations decrease (as reported in Chapter 4) and particle dynamics speed–up with an increase in the volume fraction ϕ above a critical value. Such anomalous behavior has been reported for complex liquids such as water [284, 285] and silica [286] and has been long argued to exist for systems with non–directional, core–softened repulsive interactions [215-217, 287-290]; herein we report the first instance of experimental observation of such behavior in a soft colloidal system.

Colloidal suspensions have been extensively studied as models for atomic and molecular liquids [62, 64, 291]. They share important similarities, including disordered structure, analogous long time dynamics, glass/jamming transitions, and ability to undergo solid–liquid phase transitions upon application of suitable density, pressure, or thermal fields. Recently, soft colloids have garnered significant attention for their ability to mimic more complex interactions in molecular fluids with non–hard–sphere like interactions [63, 65, 66, 215-225, 292]. Among the most striking observations reported in these systems is an anomalous transition to a state of reduced inter–particle correlation near the jamming transition [65, 215-225]. Suspensions of a variety of soft particles including soft microgel particles[65], tapioca pearls [218, 219], concentrated star polymer solutions [220] and nano–emulsions [221] have been shown to exhibit anomalous structural characteristics. These trends are analogous to those observed in water, wherein

isothermal compression allows a fifth molecule to enter into the tetrahedral network of molecules, leading to a decrease in structural order [284, 285]. This reduced order manifests as anomalous, high diffusivities upon compression [284, 285, 293, 294] as well as an anomalous reduction in density in water, but none of the other traits associated with the appearance anomalous structure in molecular liquids have so far been observed in soft colloidal systems.

We previously reported nanoparticle suspensions, created by densely grafting oligomeric polyethylene glycol (PEG) chains (M_W ~ 450 Da) on nanometer–sized silica (SiO_2) and suspended in a PEG oligomer (M_W ~ 550 Da) [43, 53]. These materials provide a good physical model for soft particle suspensions because enthalpic forces are completely turned off and thermal forces are significant [43]. In particular, we observed that these suspensions manifest little to no aging and are able to reach an equilibrium, Newtonian fluid regime even at particle loadings beyond the apparent "jamming" transition where the zero shear viscosity η of the suspensions appear to diverge [43]. These materials have also been shown to exhibit structure anomaly as discussed in Chapter 4. Here we focus on the relaxation processes in these suspensions and their behavior across the jamming transition.

8.2. Results and Discussion

8.2.1. Ergodic–*yet*–Hyperdiffusive Soft Nanoparticle Suspensions

Insights into the dynamics processes in these suspensions can be provided by the time–correlation of the scattering intensity patterns, as probed through X–ray photon correlation spectroscopy (XPCS) measurements, which were carried out at Sector 8–ID–I of the Advanced Photon Source. A contour map of the two–time intensity auto correlation function $G(q,t_1,t_2)\left(=\langle I(q,t_1)I(q,t_2)\rangle/\langle I(q,t_1)\rangle\langle I(q,t_2)\rangle\right)$ for a SiO_2–PEG nanoparticle suspensions is

shown in Figure 47a and clearly indicates towards the absence of any time dependent slowing down or speeding up of the nanoparticle motion [72]. These results in conjunction with the non–aging rheological characteristics of the suspensions [43] clearly point towards any absence of aging in these suspensions. Further averaging $G(q, t_1, t_2)$ for a fixed time interval, $t = t_2 - t_1$ can lead to the time autocorrelation of the scattering intensity patterns as $g_2(q,t) = \langle G(q,t_1,t) \rangle_{t_1}$, and subsequently the dynamic structure factor can be obtained as $f(q,t) = ((g_2(q,t) - 1)/b)^{1/2}$ [281]. Here, b is an instrument–dependent Seigert factor. Colloidal suspensions have been reported to exhibit two distinct relaxation processes near the jamming transition: a fast relaxation originating from in–cage rattling motion of particles with time scales typically < 1 ms, which is outside the measurement window for XPCS; and a slower relaxation originating from the nanoparticle cage–escape [64, 295]. The slower processes are characterized by partial correlation among scatterers at small times corresponding to $f(q,t) < 1$ and are succinctly captured at ϕ values both below and above ϕ_S, as shown in Figure 47b and Figure 47c, respectively. While a terminal relaxation ($f(q,t) \sim 0$ at large t) with finite relaxation time scales is expected for unjammed suspensions (Figure 47b), the appearance of a terminal relaxation regime for $\phi > \phi_S$ (Figure 47c) is in stark contrast to usual observations in jammed colloidal suspensions, even comprising of soft particles [65]. It is consistent, however, with our earlier report [43] that the suspensions are able to reach an equilibrium state characterized by a Newtonian flow regime and also the aforementioned non–aging characteristics.

We conjecture that a combination of factors might be responsible for the unique "jammed"–yet–equilibrated dynamic characteristics of the SiO_2–PEG/PEG suspensions: i) the small size of the particles mean that the Brownian stresses are quite large $O(0.3 \times 10^5$ Pa) and easily exceeds the

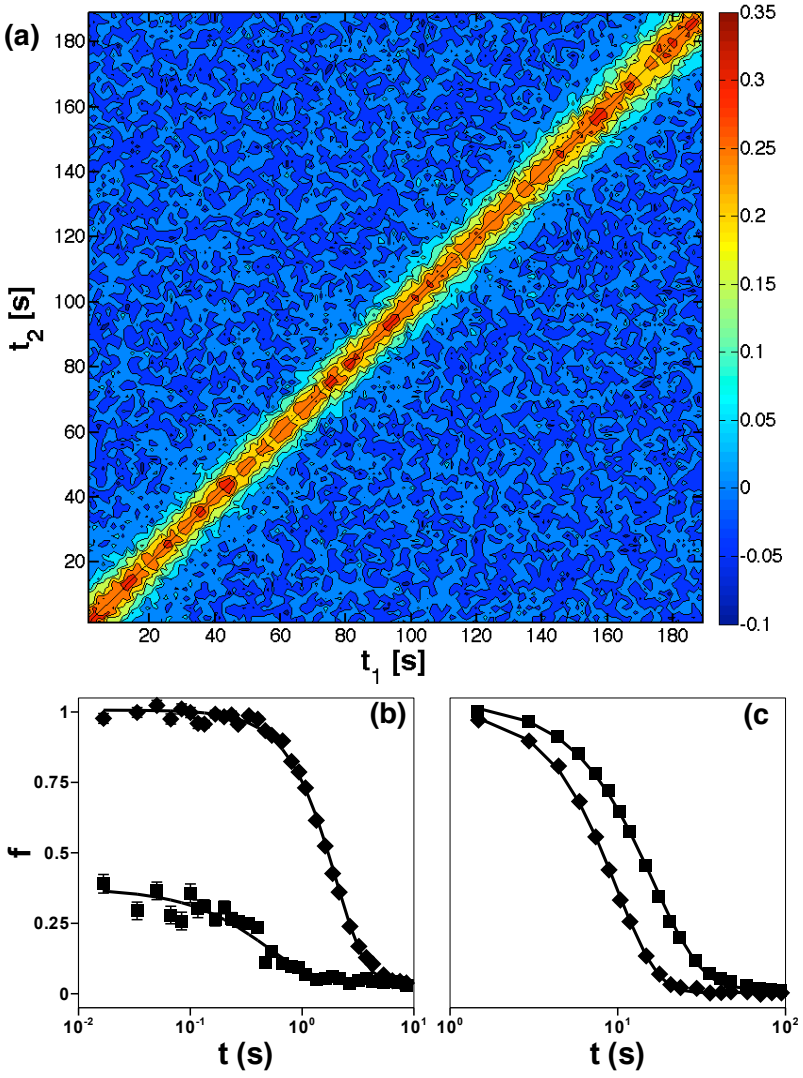

Figure 47 Temporal evolution of the scattering intensities. **a.** A contour map of the two–time correlation function G for the d = 10 nm, ϕ = 0.35 suspension at q = 0.568 nm^{-1}. **b.**, **c.** Dynamic structure factor $f(q,t)$ for d = 10 nm particle suspensions with **b.** ϕ = 0.19 (squares), 0.27 (diamonds), **c.** 0.30 (squares) and 0.35 (diamonds). Solid lines in **b.** and **c.** are compressed exponential fits.

viscous modulus *G"* of the "jammed" suspension [43], which produces a strong driving force for relaxation; ii) segmental motion of the tethered PEG oligomers provides an *internal lubrication* among overlapping particles, which favors particle relaxation and cage escape; and iii) the flexibility of the tethered PEG chains imparts softness to the particles, facilitating local rearrangements on the way to equilibrium. An advantage of these characteristics is that the time scale τ associated with the cage–escape motion of the nanoparticles is visible in the dynamic structure factor on convenient timescales for XPCS. By fitting the measured $f(q,t)$ (Figure 47b and Figure 47c) with a compressed exponential function [281]:

$$f(q,t) = f_0 \exp\left[-\left(\frac{t}{\tau}\right)^{\beta}\right] \tag{17}$$

it is possible to determine the time scale τ and the compression exponent β. Further, the nature of the forces acting on the nanoparticles can be elucidated by the wave vector dependence of τ and is presented in Figure 48. A characteristic $1/q$ scaling is observed for nearly all the suspensions, indicating a slow, hyperdiffusive motion of the nanoparticles. Similar ballistic motion of scatterers has been reported in a variety of jammed soft solids as well as glassy liquids [70-72, 281, 283, 296-298] and is generally understood to arise from residual stress dipoles that originate in a system going through the jamming transition. However, relaxation of these stress dipoles is expected to lead to significant aging behavior, which is inconsistent with our observations. Equally significant is the fact that at low nanoparticle loadings, a transition to a weak diffusive scaling with a $\tau \propto 1/q^2$ is found for the 24 nm particles, indicating that the hyperdiffusive behavior is not directly associated with particle–particle overlap or jamming. At the same time, this transition from diffusive to hyperdiffusive particle dynamics with increasing particle (scatterer) density is the first experimental report of the phenomenon to our knowledge.

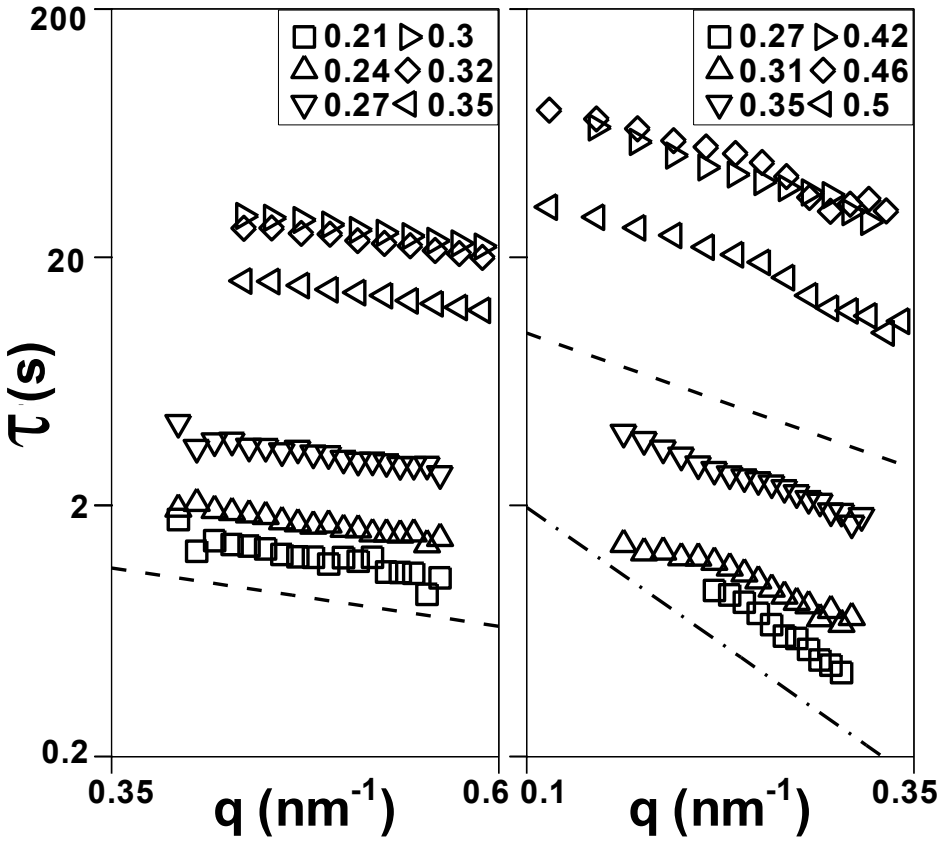

Figure 48 Wave vector dependence of relaxation time τ for d = 10 nm (left panel) and 24 nm (right panel). Dashed line denotes a $\tau \propto 1/q^2$, while the dash–dot line denotes $\tau \propto 1/q$ scaling.

8.2.2. Transport Anomaly

Figure 49 reports the characteristic relaxation time τ for the suspensions as a function of ϕ for four different particle sizes. Initially, τ grows with increasing ϕ as expected and is described fairly well by a fit of the Vogel–Fulcher–Tammann (VFT) form [66, 295], $\tau = \tau_\infty \exp\left[A/(\phi_0 - \phi)\right]$, shown as solid lines in the Figure. But beyond a critical $\phi = \phi_D$, particle dynamics clearly speed up, leading to a non–monotonic dependence of τ on ϕ in all but the largest 40 nm particles. As pointed out earlier, such counterintuitive transport behavior has heretofore only been observed in complex liquids such as water [284, 285, 293, 294]. At the same time, simulation studies for model systems interacting with Hertzian [215-217], Gaussian [216, 217, 287, 288] or other core–softened repulsive potentials [216, 217] [223, 289, 290] have predicted the underlying dynamic anomaly to occurs when $(\partial s_{ex}/\partial \ln \rho)_T > 0.42$, indicating that it should naturally follow the occurrence of a structural anomaly, as discussed in Chapter 4 ($(\partial s_{ex}/\partial \ln \rho)_T > 0$) [290]. s_{ex}, ρ and T denote excess entropy, density and temperature, respectively. That this "cascade" of anomalies [285, 290] is observed ($\phi_D > \phi_S$) (see Chapter 4 for a description of ϕ_S), for the first time, in our SiO_2–PEG/PEG suspensions indicate that these suspensions are good physical models for fluids in which core–softened repulsive interactions dominate. Our findings also support the hypothesis that the anomalous trends in dynamics of such fluids occur independent of hydrodynamic interactions between the particles and solvent [216, 217]. The structural and transport trends eventually return to normalcy in water owing to extremely steep short range repulsion in the limit of very high density [284, 285, 288] and we expect the same to occur in the soft suspensions investigated here as well in the limit of extreme overlap, however, crystallization prevents any investigation at even higher particle densities. Also, decreasing particle softness (increasing d) leads to progressively earlier onset of the crystallization, to the

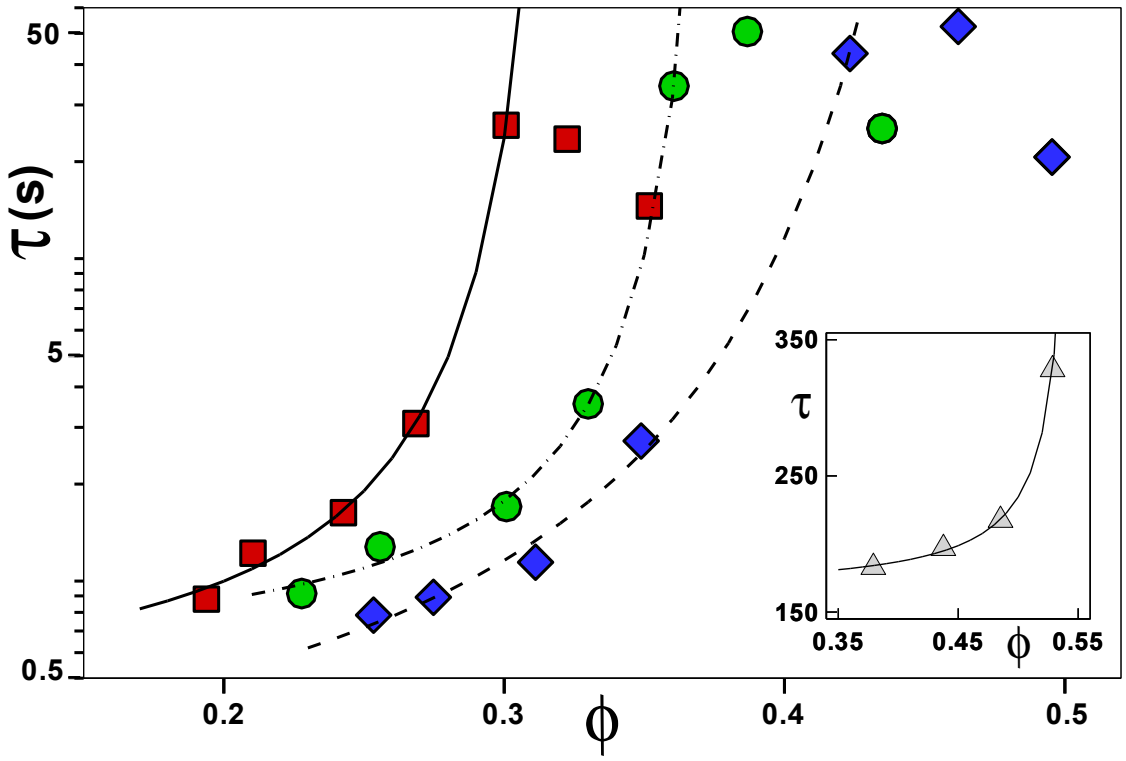

Figure 49 Particle loading dependence of the relaxation time τ for d = 10 nm (squares), 16 nm (circles), 24 nm (diamonds) and 40 nm (triangles, inset) suspensions. Lines indicate VFT fits. τ values reported at q = 0.49 nm^{-1}, 0.35 nm^{-1}, 0.19 nm^{-1}and 0.10 nm^{-1}, respectively.

extent that it prevents the observation of the dynamic anomaly in the largest, 40 nm nanoparticle suspensions.

8.3. Conclusions

In summary, we have studied suspensions of oligomer–grafted nanoparticles in an oligomeric fluid host and find structural (reported in Chapter 4) and dynamic trends that are consistent with theory, but heretofore not observed in experiments. In particular we find that particle–particle correlations increase with ϕ only up to a critical value ϕ_S, where after they decrease with increasing particle loading in the suspensions (see Chapter 4). Additionally, we find that the diffusivity of the particles exhibit a similar transition wherein the particle mobility first falls with increasing ϕ but then enters a regime of faster motion at $\phi > \phi_D$. Complex, network forming molecular fluids such as water and silica as well as systems interacting with core–softened repulsive interactions have also been shown to exhibit similar cascade of structural and transport anomalies, and it is generally understood that softness of the repulsive forces allows for strong entropic gains to more than compensate for the energetic cost of molecule/particles overlaps in all the cases. Our observations suggest that soft nano–colloids extend the tool–box of the experimental physicist interested in using suspensions for studying interactions and dynamics in molecular liquids.

CHAPTER 9

THE ORIGIN OF HYPERDIFFUSIVE RELAXATIONS IN SOFT MATTER*

Abstract

Small particles suspended in fluids move randomly over long length– and time–scales. This motion is the expected response of weakly interacting particles to uncoordinated bombardments from the fluid molecules. This feature of suspensions is considered a fundamental characteristic of their equilibrium state and, over long–enough observation times, leads to universal diffusive particle motions. We report on the motions of particles in single component suspensions in which the suspended (particle) and suspending (fluid) phases are chemically linked. Even in equilibrated state, relaxations in these suspensions are hyperdiffusive. Our observations add to a large number of recent reports, which show that diffusive motion is not the norm in soft matter such as colloidal gels, nanoemulsions and soft nanoparticle glasses. In such systems, particle motions can be highly correlated over long distances and time, belying long–lived, directed forces thought to arise from out–of–equilibrium, metastable states that can drive sudden irreversible structural re–arrangements. We show that hyperdiffusive motion in soft matter does not require such states and can arise naturally from volume fluctuations brought about by thermal forces. We further show that the simplicity of the force dipoles produced by volume fluctuations in our single–component suspensions leads to a physical origin for hyperdiffusion as fundamental as that commonly thought to produce diffusion of particles in dilute suspensions.

*P. Agarwal carried out a part of sample synthesis and measurements (rheology and X–ray photon correlation spectroscopy) presented in this chapter. R, Mangal also contributed towards sample synthesis and rheology measurements presented in this chapter.

9.1. Introduction

Dynamics of particles suspended in fluids have been observed and studied in great detail for close to two centuries, particularly following Brown's 1827 observation of motion of suspended organelles in water [299]. In dilute suspensions of particles in simple fluids, the inter–particle interactions are minimal and the particle motion is typically governed by steady, random bombardments from fluid molecules, leading to a linear scaling of the particle's mean square displacement with time [300]. With the advent of advanced characterization techniques and increasing latitude of applications, interest in particle motions in fluids has expanded to infer properties of complex fluids [301], including granular materials, polymers, foams, and emulsions. Many of these materials – foams, pastes, concentrated colloidal suspensions – exhibit arrested dynamics reminiscent of molecular glasses [66, 259], with metastable states [291] [258], thermally inaccessible relaxations and collective heterogeneous dynamics [58, 64, 302, 303], leading to their collective designation as soft glasses [68].

A growing number of recent reports have sought to shed light on terminal relaxations in such soft glasses [44, 70-72, 154, 263, 283, 296, 297, 304-307] and, remarkably, find them to be almost universally hyperdiffusive. Correspondingly, the inverse length scale, or wave vector q is found to scale as inverse of the characteristic relaxations time in scattering experiments. These relaxations are now thought to reflect a material's out–of–equilibrium response to internal stresses, which are either built into the systems at the glass transition [283, 305] or build up due to a variety of reasons, for instance, syneresis in attractive colloidal gels [70], charge accumulation in laponite suspensions [296], droplet collapse in emulsions [297], or progressive crosslinking of actin filaments [306]. Despite its wide range of potential origins, it is remarkable that hyperdiffusion manifests strikingly universal features in such a broad spectrum of materials;

including recent reports in metallic glasses [308]. It is also clear that the length and time scales [71] of the relaxation events are so much larger than those associated with the ballistic regime in Brownian motion [309] that the forces producing hyperdiffusion must be correlated over exceedingly long times.

In this Article, we present an account of relaxations in self–suspended nanoparticle fluids created by densely grafting short polymers to 10 ± 2 nm silica (SiO_2) nanospheres [42]. We find that these fluids spontaneously manifest simple Newtonian liquid flow behavior and negligible aging – both characteristics of an equilibrated suspension – yet exhibit decidedly hyperdiffusive particle dynamics on long time scales. This combination of dynamical features has not previously been reported in a suspension and provides new clues about the general origins of hyperdiffusion. In the absence of an explicit solvent, the single–component nature of the studied nanoparticle fluids leads to extremely homogenous particle arrangements and allows structural relaxations to be simply described by a well–known theoretical framework. Our results also provide insights into the role of temperature on structural relaxations in soft materials.

9.2. Materials and Methods

Self–suspended nanoparticle fluids were prepared by tethering polyisoprene (PI, M_w = 5000, 7.3 and 13.4 KDa, PDI ~ 1.1, 1.05 and 1.04) or polyethylene glycol (PEG, M_w = 5 KDa, PDI ~ 1.09,) chains on the surface of SiO_2 nanoparticles (LUDOX^{TM} SM–30) using previously reported synthesis methods [42]. XPCS measurements were carried out at Sector 8–ID–I of the APS. $g_1(q,t)$ was calculated as $g_1(q,t)=\sqrt{\left[\left\{\left\langle I(q,t_1)I(q,t_1+t)\right\rangle / \left\langle I(q)^2\right\rangle\right\}-1\right]/\beta}$, with β being an instrument–dependent contrast factor. Anton Paar MCR 501 rheometer with cone and plate geometry was used for rheology measurements.

9.3. Results and Discussion

9.3.1. Relaxation Dynamics at the Nanoscale

The intermediate scattering function $g_1(q,t)$, which is the spatial and temporal Fourier transform of the time–dependent particle pair number density correlation function $\langle n(r,t)n(0,0)\rangle$, was obtained from the X–ray photon correlation spectroscopy (XPCS) measurements [72] provides a convenient means of characterizing the long–time correlated motions of small particles in a fluid. The relaxation of correlation between particle positions typically decays as a compressed exponential function of time, t, with a wave vector (q)–dependent characteristic relaxation time τ as $g_1(q,t) = \exp\left[\left(t/\tau(q)\right)^{\beta}\right]$. Here n is the particle number density, r and t are position and time, respectively, and β the compression exponent. A representative $g_1(q,t)$ plot is shown in the inset of Figure 50 along with the computed fit of the expression (1). τ–q relationships obtained from measurements at multiple q values are reported in Figure 50 for two representative self–suspended suspension systems: (A) 5 KDa PEG tethered SiO_2 nanoparticles (PEG–SiO_2) and (B) 7.3 KDa PI tethered SiO_2 nanoparticles (PI–SiO_2) with particle volume fractions ϕ being 0.123 and 0.033, respectively. The trends for these, as well other systems spanning a range of ϕ (Figure 51), are seen to generally conform to a $\tau \alpha q^{-1}$ relationship, signifying hyperdiffusive relaxations of the nanoparticle cores. The range of length scales over which such hyperdiffusive relaxations are observed is noteworthy – the characteristic length scale $l \sim 2\pi/q$ varies from 10 nm to 165 nm (approximately 1–16 times the nanoparticle diameter d), indicating that the XPCS measurements probe particle relaxations at length scales considerably larger than those associated with the ballistic regime in Brownian motion ($<< d$) and substantially larger than typical interparticle separations λ ($= d(0.64/\phi)^{1/3} \sim 15 – 30$ nm) in the materials.

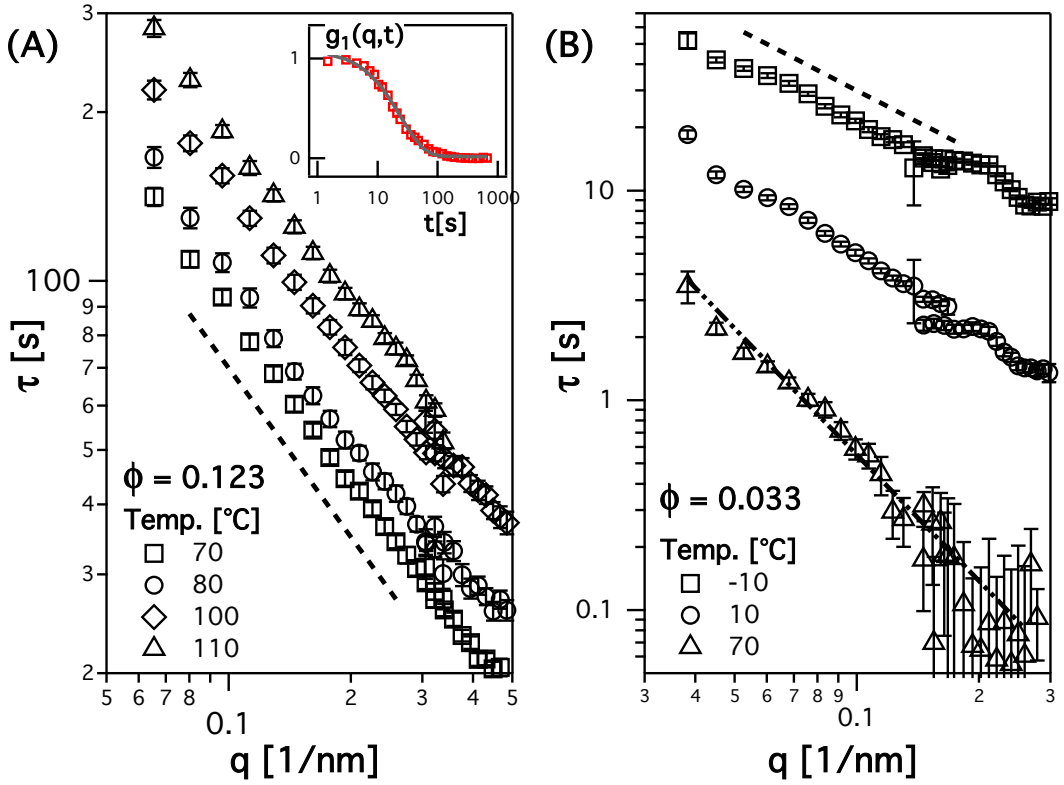

Figure 50 Hyperdiffusive particle dynamics. Characteristic relaxation time τ vs. wave vector q at different temperatures for **A.** 5 KDa PEG–SiO_2 and **B.** 7.3 KDa PI–SiO_2 nanoparticle fluids. Dashed and dashed–double dot lines correspond to –1 and –2 power law, respectively. *Inset* shows a $g_1(q,t)$ measurement at q = 0.24 nm^{-1} and 80°C (symbols) and the compressed exponential fit (line) for system depicted in **A.** with circles. The error bars are of the same size as symbols in the inset. The discontinuity in data sets is a result of two separate measurements in different q ranges being shown in the same plot.

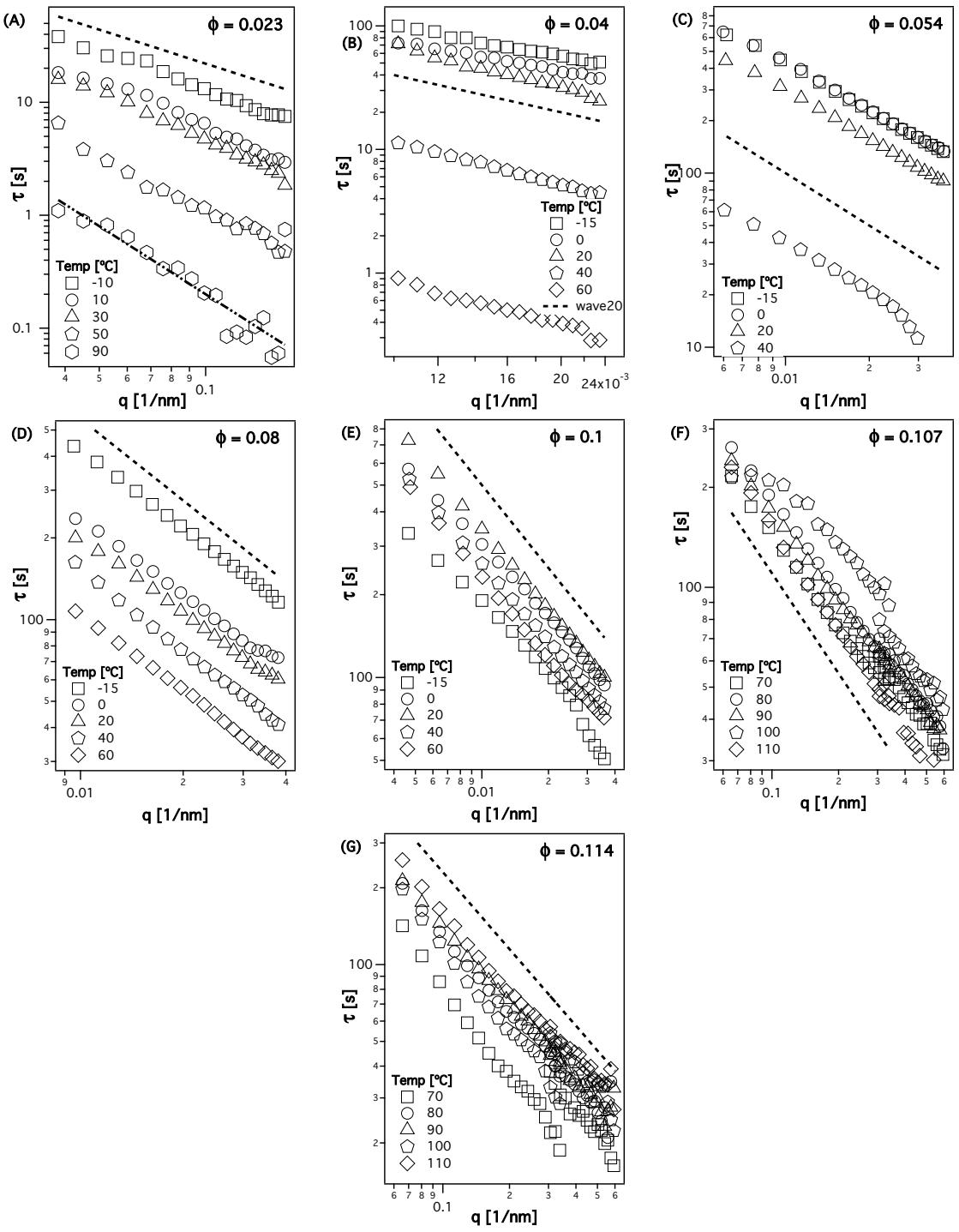

Figure 51 Characteristic relaxation time τ vs. wave vector q at different temperatures for **A.** 13.4 KDa PI–SiO_2 **B–D**. 5 KDa PI–SiO_2 and **E–G.** 5 KDa PEG–SiO_2. Dashed and dashed–double dot lines correspond to –1 and –2 power law, respectively.

The particle structure was shown to be independent of temperature in Chapter 4. In contrast, particle relaxation times deduced from the time–dependent XPCS measurements vary with temperature in a non–trivial manner. As shown in Figure 50b for ϕ = 0.023 systems, τ predictably decreases with temperature T as might be expected in a fluid with increasing thermal energy and decreasing resistance from the surroundings. This should be contrasted with results presented for the same material (ϕ = 0.123) with lower grafting density of the polymer chains. This fluid exhibits an unexpected increase in relaxation time with increasing T (Figure 50a).

Figure 52 reports the hyperdiffusion velocity ($v = 1/q\tau$) in a wide variety of self–suspended fluids. At low ϕ ($\phi \leq 0.08$), v is seen to increase monotonically with T; for intermediate ϕ (ϕ = 0.1, 0.107), an initial decrease in v is followed by an upturn; and for the most sparsely grafted particles (ϕ = 0.114, 0.123), v decreases monotonically with T. The unexpected decrease in v with T concurs with the previously reported thermal jamming [172] in similar nanoparticle fluids, which was attributed to an effective attraction between the polymer chains arising from the space–filling constraint, leading to an increase in the excluded volume of the chains and interdigitation with increasing temperature. With increasing ϕ, the chain interdigitation effects become stronger and, at low temperatures, may supersede the combined effects of thermal energy and reduced resistance to motion, producing the observed minimum in v. And, although a minimum in v was not observed for the fluids with the highest particle content, it can be expected subsequently at even higher T.

Simultaneous comparison of the temperature dependent behavior at the nano– and the macro–scale presented in Figure 53 highlights the versatility of these self–suspended fluids in accessing features associated with glassy materials. At lower ϕ, behaviors akin to what might be measured in a conventional suspension are observed at both the particle– and continuum–fluid scale.

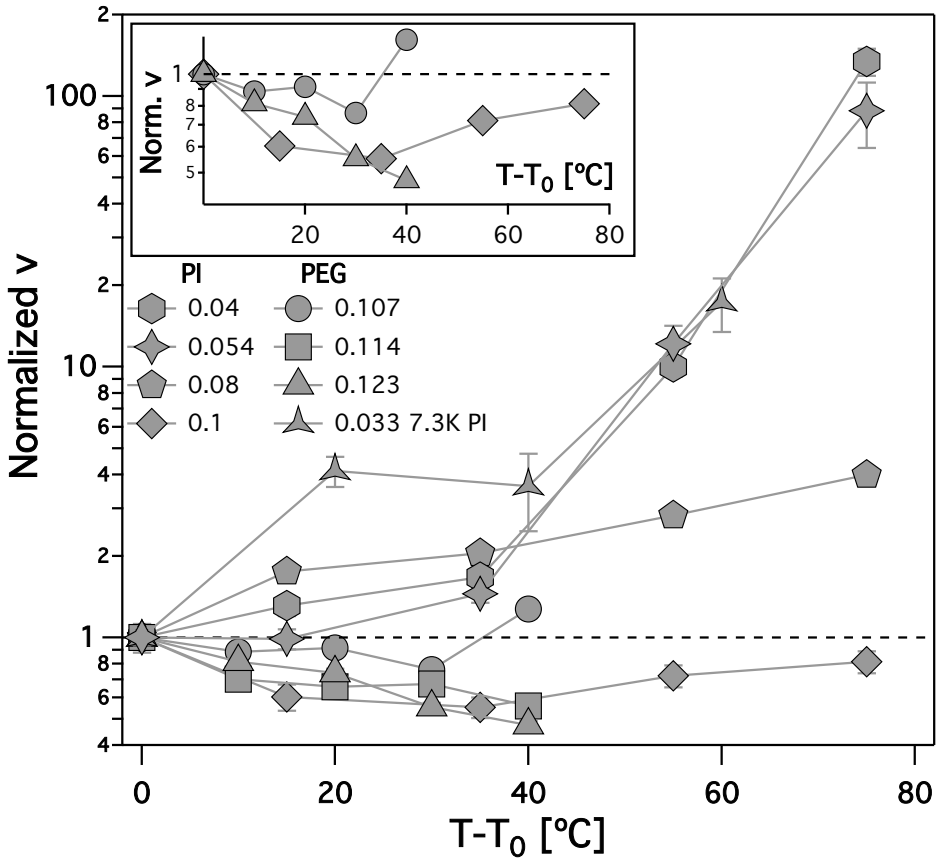

Figure 52 Anomalous temperature dependence of particle velocity. Normalized velocity v vs. adjusted temperature $T–T_0$ for 5 KDa PI–SiO_2 ($T_0 = –15^oC$), 7.3 KDa PI–SiO_2 ($T_0 = –10^oC$) and 5 KDa PEG–SiO_2 ($T_0 = 70^oC$) nanoparticle fluids. The lines are guide to the eye. The *inset* shows the same data for three samples with negative deviations on an adjusted scale for clarity.

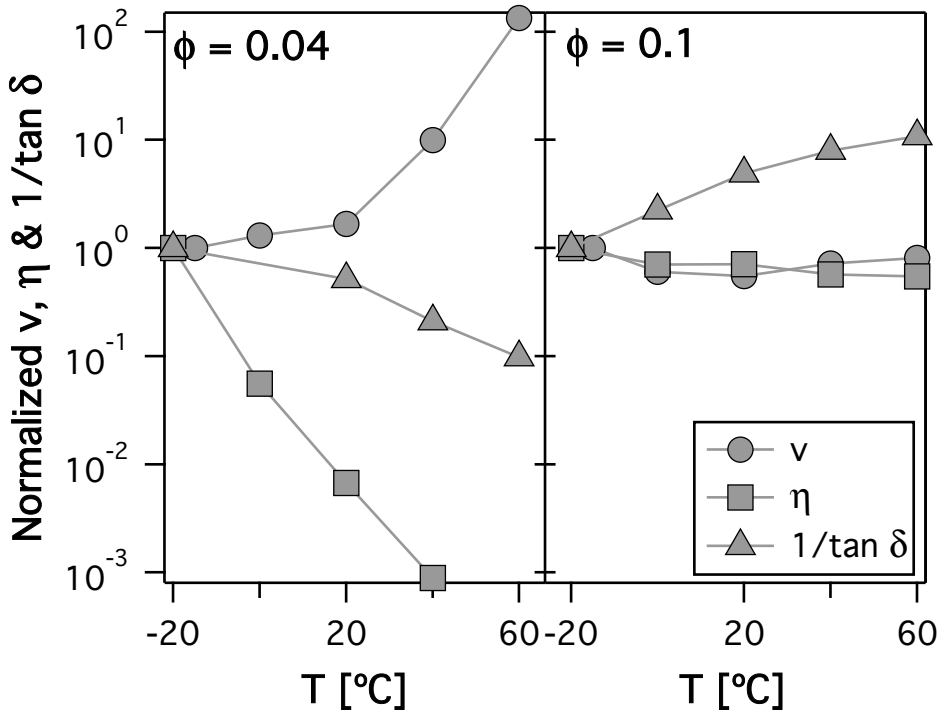

Figure 53 A versatile platform. Normalized velocity v, viscosity η and inverse loss tangent 1/tan δ vs. temperature T for 5 KDa PI–SiO_2 nanoparticle fluids with ϕ = 0.04 and 0.1. The variables are normalized by v at $T = -15^oC$ and η and 1/tan δ at $T = -20^oC$, respectively.

Specifically, the hyperdiffusion velocity v increases while the fluid viscosity η and the inverse loss tangent, 1/tan δ (=elastic shear modulus/mechanical loss modulus, G'/G'') decrease with temperature; all pointing to an increase of fluidity with temperature, consistent with normal expectations for simple fluids. In contrast, at higher $\phi = 0.1$, v exhibits a weak minimum, η is largely temperature independent, and 1/tan δ increases with increasing temperature, all indicating increasing jamming of the material as temperature rises. Thus, through completely antagonistic responses to temperature, these materials highlight the non–trivial role of temperature in soft materials and strongly contest current understanding that heating merely fluidizes a soft material.

9.3.2. Hyperdiffusive *At–Equilibrium* Systems

In combination with hyperdiffusive relaxations, Figure 54 highlight what we feel are the most remarkable features of the low ϕ self–suspended suspensions. The figure shows that these fluids manifest an accessible Newtonian flow regime with a shear rate independent viscosity, implying that the materials are able to reach equilibrium on the time scales of the flow. As reported previously [172], a unique feature of all self–suspended suspensions is that even when jammed, they do not exhibit the pronounced aging typically observed in soft glasses. Considered together with the fact that tan $\delta > 1$ for the low ϕ fluids at all temperatures studied (tan δ (–20^o C) = 1.2, see Figure 53), the materials appear to behave unambiguously as equilibrated viscous fluids on long time scales. It is then surprising that these same fluids exhibit hyperdiffusive particle motions on long time–scales (Figure 50b and Figure 51A–C). We suspect that this seemingly contradictory set of behaviors stem from the inherent frustration that the tethered polymers experience [46], implying that these fluids lie near the boundary of colloidal glasses and conventional suspensions. The space–filling constrain on the tethered chains leads to their slow dynamics [46] and hyperdiffusive relaxations, but weak thermal and/or shear forces can easily

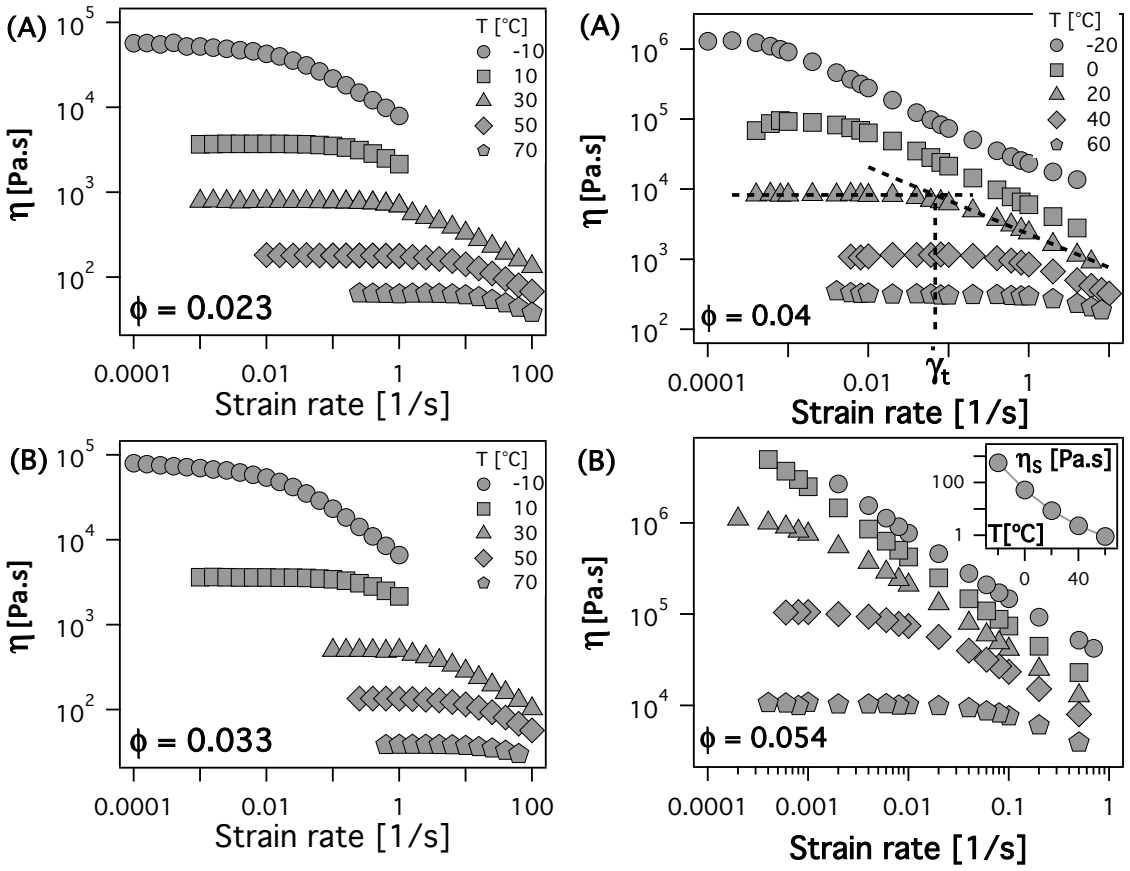

Figure 54 Hyperdiffusive systems with Newtonian flow regime. Rate sweeps at different temperatures for **A.** ϕ = 0.023 13.4 KDa PI–SiO_2 **B.** ϕ = 0.033 7.3 KDa PI–SiO_2 **C.** ϕ = 0.04 5 KDa PI–SiO_2 and **D.** ϕ = 0.054 5 KDa PI–SiO_2 nanoparticle fluids. *Inset* shows the zero shear viscosity η_S for 5 KDa PI.

overcome the entropic penalty imposed on the chains and thus the particles speed up upon heating and relax easily under shear. A crossover to diffusive particle motion ($\tau \alpha q^{-2}$) can also be expected in the extreme case when thermal forces completely overcome the space filling constraints on the tethered chains. Such a transition is clearly observed for $T \geq 70^{o}$C in self–suspended fluids based on 7.3 KDa (Figure 50B) and 13.4 KDa (Figure 51A) polyisoprene tethers. We would like to emphasize here that the hyperdiffusive to diffusive transition is unlike similar transitions in nanoparticle–polymer blends reported [283, 310] wherein the matrix itself underwent a glass to fluid transition, allowing the particle to move more freely.

9.3.3. Theoretical Estimates

Comparisons of the relevant time scales probed in our experiments provide insight into the relaxation processes that lead to the observed behaviors. The particle diffusivity ($= \tau^{-1}q^{-2}$) is estimated to be 100 nm^2/s, which is around two orders of magnitude smaller than the Stokes–Einstein diffusivity of the SiO_2 nanoparticles studied here. Taken in conjunction with the zero shear viscosity being at least two orders of magnitude higher than the corresponding polymer melt viscosity η_S (inset of Figure 54D), this simple analysis reveals that even at the relatively low nanoparticle loadings the tethered polymers and particles are under severe constraints; a hallmark of an essentially one–component fluid. Further, comparison (see Figure 55A) of the XPCS characteristic relaxation time τ_p ($=\tau(q \sim 2\pi/\lambda)$) and the characteristic relaxation time as probed by shear measurements τ_r ($= 1/\dot{\gamma}_t$), with $\dot{\gamma}_t$ being the shear rate associated with the transition from the Newtonian to the shear–thinning flow regime (shown in Figure 54C), reveal that they are of the same order, signifying that the XPCS measurements are probing at–equilibrium processes in the fluids. The Brownian configurational relaxation time scale [227] ($\tau_{Br} \sim 6\pi\eta_S a^3/k_B T$) based on η_S is found to be two orders of magnitude smaller than τ_r, highlighting the

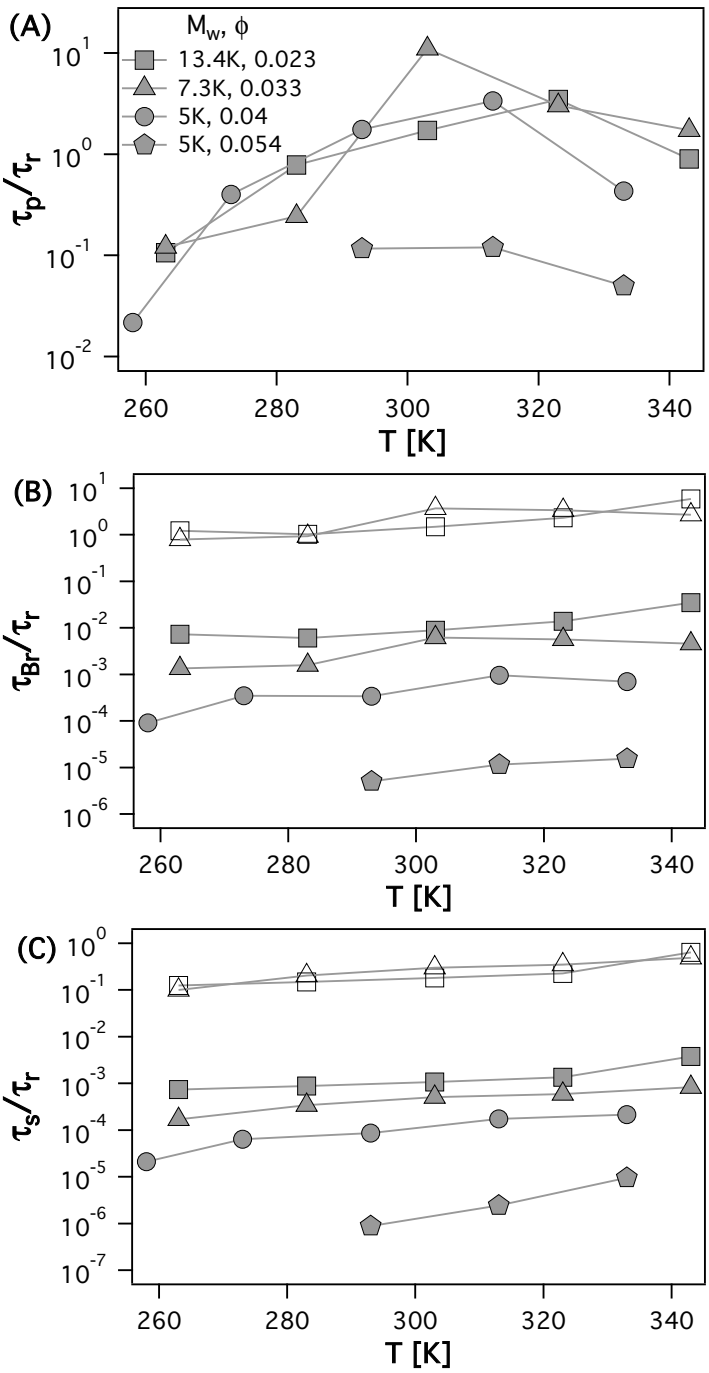

Figure 55 Competing time scales. The ratio of **A.** XPCS characteristic relaxation time τ_p and the characteristic relaxation time as probed by shear measurements τ_r, **B.** Brownian configurational relaxation time scale τ_{Br} and τ_r and **C.** strain propagation time scale τ_s and τ_r as a function of temperature T for various PI–SiO_2 nanoparticle fluids.

fact that the local viscosity that the particles experience is much higher than η_S. Here a and k_B correspond to the particle radius and the Boltzmann constant, respectively. The enhancement in local viscosity over η_S can be estimated from the diffusivity values obtained from XPCS measurements, leading to a revised estimate of $[\tau_{Br}/\tau_r]_{eff}$ (Figure 55B, open symbols) equal or larger than unity, indicating that hyperdiffusion is indeed faster than Brownian relaxations in these systems [283]. The whole fluid can thus be envisaged as being trapped in the "ballistic" regime because of insufficiency of collisions or collisions being ineffective in randomizing the particle trajectories.

Randomly occurring volume heterogeneities in out–of–equilibrium soft glasses are currently understood to lead to formation of force dipoles, which direct relaxations and particle motion [304] [70]. These relaxation processes also manifest as significant time–dependent rheology and aging. Additional understanding of the origins of hyperdiffusion can be obtained with the help of a simple analysis of these processes first proposed by Bouchaud and Pitard [311] that should be especially applicable to self–suspended materials that exhibit a Newtonian flow regime. The starting point is the equation of motion for the elastic strain field $\boldsymbol{u}$ at a point $\boldsymbol{r}$ produced by a force dipole of strength $\boldsymbol{P_0}$ and located at $\boldsymbol{r_0}$:

$$6\pi\eta an\frac{\partial \mathbf{u}}{\partial t} - K\nabla^2\mathbf{u} = \mathbf{P_0}\cdot\nabla\left(\mathbf{r}-\mathbf{r_0}\right) \tag{18}$$

Here K is the bulk modulus and n is the particle number density (= $3\phi/4\pi a^3$). Comparing the strain propagation time, $\tau_s \sim 6\pi\eta a^3 n/K$ to τ_r ((Figure 55C), we see that the ratio increases with temperature and decreases with particle loading, implying that as the temperature rises or particle content decreases, bulk relaxations become increasingly effective in competing with – and eventually overtaking – strain propagation; providing a straightforward explanation for the

transition from force–dipole driven hyperdiffusive to diffusive motions observed at the lowest particle loadings and highest temperature, 70°C when $\tau_s/\tau_r \sim 1$.

Thermal forces are the only drivers for generating force dipoles in the *at–equilibrium* systems considered here ($\phi \leq 0.054$), and hyperdiffusion arises from the system's response to thermal fluctuations in the volume associated with each particle and the accompanying chains. Balancing the energy requirements, $nK(\Delta V)^2=k_BT$, with ΔV being the change in the volume associated with the fluctuation in the interparticle distance ($\sim n^{-2/3}\Delta\lambda$), the strength of the resultant force dipole $|\mathbf{P}_0|$ can be estimated as $\left|\mathbf{P_0}\right| = \lambda\dfrac{\partial\left(nK\left(\Delta V\right)^2\right)}{\partial\lambda} = 2\lambda K\Delta\lambda n^{-1/3} = 2\left(\dfrac{Kk_BT}{n}\right)^{1/2}$. Lastly, we relate the dipole collapse time scale, θ, to τ_r ($=1/\dot{\gamma}_t$) and approximate K using the formula, $K = A\left(\nu_P\right)G \sim A\left(\nu_P\right)\eta_0\dot{\gamma}_t$. Thus, a Fourier analysis of Equation 18 [311], which yields the dynamic structure factor, $S\left(\mathbf{q},t\right) = \left\langle \exp\left[i\mathbf{q}\cdot\left(\mathbf{u}\left(\mathbf{r},t+t_1\right)-\mathbf{u}\left(\mathbf{r},t_1\right)\right)\right]\right\rangle$ as:

$$S(q,t) = \exp\left[-\frac{16\sqrt{2\pi^3}}{75}\rho\theta\left(\frac{q\left|\mathbf{P_0}\right|}{4\pi K\theta}t\right)^{\frac{3}{2}}\right] \tag{19}$$

can predict hyperdiffusion velocity v:

$$v = \frac{2}{75^{2/3}}\frac{\left|\mathbf{P_0}\right|\rho^{2/3}}{K\theta^{1/3}} = \frac{4}{75^{2/3}}\sqrt{\frac{A\left(\nu_P\right)k_BT\dot{\gamma}_t}{\eta_0}}n^{\frac{1}{6}}N_c^{\frac{2}{3}} \tag{20}$$

Here ρ ($\sim nN_c/\theta$) represents the rate of dipole collapse per unit volume, η_0 is the zero shear viscosity, ν_P is the Poisson's ratio (= 0.3), $A\left(\nu_P\right) = 2\left(1+\nu_P\right)/3\left(1-2\nu_P\right)$, θ is the dipole evolution time and N_c is the number of neighbors (= 12). Details of the calculations are provided below (*N1*).

The velocity estimates from this expression are compared with the experimental results in Figure 56. The agreement is not quantitative, but is surprisingly good considering the simplicity of the analysis and the rough estimates for some of the parameter, most notably K and θ, used for the comparisons. The extended Bouchaud–Pitard analysis is also able to reproduce experimentally observed trends with temperature surprisingly well. Thus, through a straightforward estimation of the magnitude and lifetime of force dipoles, we obtain the first direct confirmation that strain fields arising in response to stress dipoles in an equilibrated soft material can produce hyperdiffusive relaxation.

9.4. Conclusions

With an increasing number of materials exhibiting hyperdiffusive relaxations, the results presented here provide an important advancement in the understanding of the origins of the phenomenon. The unique structure of the one–component nanoparticle glasses allows temperature induced volume perturbation, which are typically considered insignificant in glassy or jammed systems, to induce hyperdiffusive relaxations in these systems even at equilibrium. The minimalistic material platform allowed for a simple theoretical description of the relaxations, and the agreement between theory and experiments observed here provides good support for the hypothesis that hyperdiffusion in glassy materials arises from a system's response to internal stresses; however, the origin of these internal stresses might vary considerably from one material to another.

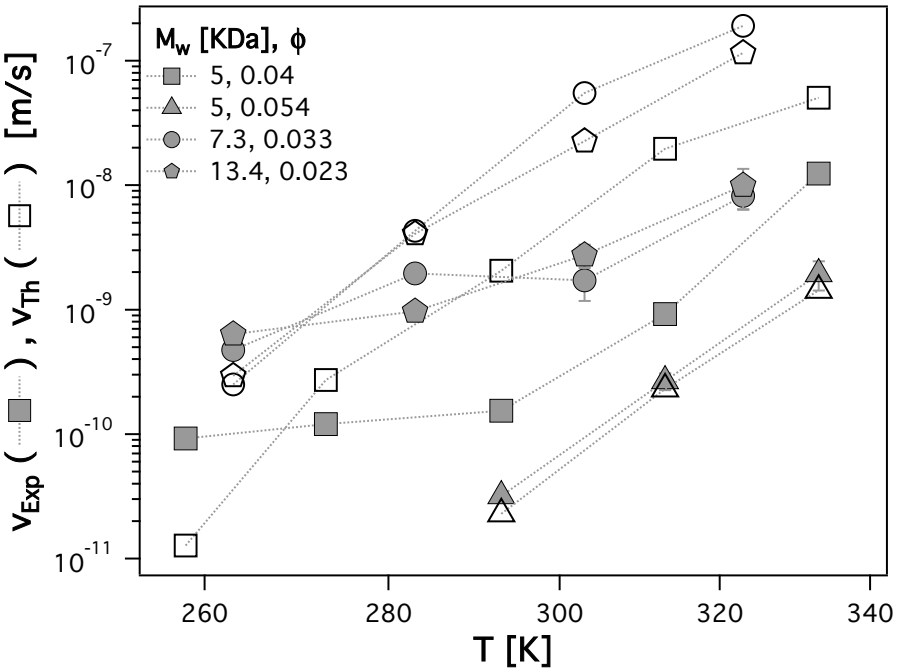

Figure 56 Comparisons between experiments and theoretical estimates. Experimental observations (filled symbols) and theoretical estimates (open symbols) of hyperdiffusion velocity v as a function of T for PI–SiO_2 nanoparticle fluids.

References

[1] A. C. Balazs, T. Emrick, and T. P. Russell, Science **314**, 1107 (2006).

[2] E. P. Giannelis, Advanced Materials **8**, 29 (1996).

[3] S. Sinha Ray and M. Okamoto, Progress in Polymer Science **28**, 1539 (2003).

[4] W. C. Chan and S. Nie, Science **281**, 2016 (1998).

[5] M. Wang, R. Joseph, and W. Bonfield, Biomaterials **19**, 2357 (1998).

[6] S. Ramakrishna, J. Mayer, E. Wintermantel, and K. W. Leong, Composites Science and Technology **61**, 1189 (2001).

[7] M. C. Chang, C. C. Ko, and W. H. Douglas, Biomaterials **24**, 2853 (2003).

[8] S. K. Misra, S. P. Valappil, I. Roy, and A. R. Boccaccini, Biomacromolecules **7**, 2249 (2006).

[9] S. R. Sershen, S. L. Westcott, N. J. Halas, and J. L. West, Journal of Biomedical Materials Research **51**, 293 (2000).

[10] W. A. Smith and B. A. Auld, IEEE Trans Ultrason Ferroelectr Freq Control **38**, 40 (1991).

[11] H. Y. Jiang, S. Kelch, and A. Lendlein, Advanced Materials **18**, 1471 (2006).

[12] M. Elimelech and W. A. Phillip, Science **333**, 712 (2011).

[13] B. H. Jeong, E. M. V. Hoek, Y. S. Yan, A. Subramani, X. F. Huang, G. Hurwitz, A. K. Ghosh, and A. Jawor, Journal of Membrane Science **294**, 1 (2007).

[14] X. Wang, X. Chen, K. Yoon, D. Fang, B. S. Hsiao, and B. Chu, Environ Sci Technol **39**, 7684 (2005).

[15] Q. Li, S. Mahendra, D. Y. Lyon, L. Brunet, M. V. Liga, D. Li, and P. J. Alvarez, Water Res **42**, 4591 (2008).

[16] N. Duran, P. D. Marcato, G. I. H. De Souza, O. L. Alves, and E. Esposito, Journal of Biomedical Nanotechnology **3**, 203 (2007).

[17] V. M. Boddu, K. Abburi, J. L. Talbott, and E. D. Smith, Environmental Science & Technology **37**, 4449 (2003).

[18] B. O. Dabbousi, M. G. Bawendi, O. Onitsuka, and M. F. Rubner, Applied Physics Letters **66**, 1316 (1995).

[19] N. C. Greenham, X. Peng, and A. P. Alivisatos, Phys Rev B Condens Matter **54**, 17628 (1996).

[20] H. Skaff, K. Sill, and T. Emrick, Journal of the American Chemical Society **126**, 11322 (2004).

[21] S. A. McDonald, G. Konstantatos, S. Zhang, P. W. Cyr, E. J. Klem, L. Levina, and E. H. Sargent, Nature materials **4**, 138 (2005).

[22] P. Gomez-Romero, Advanced Materials **13**, 163 (2001).

[23] F. Croce, G. B. Appetecchi, L. Persi, and B. Scrosati, Nature **394**, 456 (1998).

[24] J. B. Goodenough and Y. Kim, Chemistry of Materials **22**, 587 (2010).

[25] J. M. Tarascon and M. Armand, Nature **414**, 359 (2001).

[26] P. G. Bruce, B. Scrosati, and J. M. Tarascon, Angewandte Chemie **47**, 2930 (2008).

[27] X. W. Lou, L. A. Archer, and Z. C. Yang, Advanced Materials **20**, 3987 (2008).

[28] X. L. Ji, K. T. Lee, and L. F. Nazar, Nature materials **8**, 500 (2009).

[29] N. Jayaprakash, J. Shen, S. S. Moganty, A. Corona, and L. A. Archer, Angewandte Chemie **50**, 5904 (2011).

[30] A. Usuki, Y. Kojima, M. Kawasumi, A. Okada, Y. Fukushima, T. Kurauchi, and O. Kamigaito, Journal of Materials Research **8**, 1179 (1993).

[31] R. A. Vaia and E. P. Giannelis, Macromolecules **30**, 8000 (1997).

[32] Q. Zhang and L. A. Archer, Langmuir : the ACS journal of surfaces and colloids **18**, 10435 (2002).

[33] B. J. Anderson and C. F. Zukoski, Macromolecules **42**, 8370 (2009).

[34] N. Jouault, P. Vallat, F. Dalmas, S. r. Said, J. Jestin, and F. o. Boué, Macromolecules **42**, 2031 (2009).

[35] M. E. Mackay, A. Tuteja, P. M. Duxbury, C. J. Hawker, B. Van Horn, Z. Guan, G. Chen, and R. S. Krishnan, Science **311**, 1740 (2006).

[36] J. Mewis, W. J. Frith, T. A. Strivens, and W. B. Russel, AIChE Journal **35**, 415 (1989).

[37] C. Li, J. Han, C. Y. Ryu, and B. C. Benicewicz, Macromolecules **39**, 3175 (2006).

[38] J. Pyun, S. Jia, T. Kowalewski, G. D. Patterson, and K. Matyjaszewski, Macromolecules **36**, 5094 (2003).

[39] D. L. Green and J. Mewis, Langmuir : the ACS journal of surfaces and colloids **22**, 9546 (2006).

[40] R. Rodriguez, R. Herrera, L. A. Archer, and E. P. Giannelis, Advanced Materials **20**, 4353 (2008).

[41] P. Akcora *et al.*, Nature materials **8**, 354 (2009).

[42] P. Agarwal, H. Qi, and L. A. Archer, Nano letters **10**, 111 (2010).

[43] S. Srivastava, J. H. Shin, and L. A. Archer, Soft Matter **8**, 4097 (2012).

[44] S. Srivastava, L. A. Archer, and S. Narayanan, Physical Review Letters **110**, 148302 (2013).

[45] A. B. Bourlinos, R. Herrera, N. Chalkias, D. D. Jiang, Q. Zhang, L. A. Archer, and E. P. Giannelis, Advanced Materials **17**, 234 (2005).

[46] P. Agarwal, S. A. Kim, and L. A. Archer, Physical Review Letters **109**, 258301 (2012).

[47] H. Y. Yu and D. L. Koch, Langmuir : the ACS journal of surfaces and colloids **26**, 16801 (2010).

[48] K. Y. Lin and A. H. Park, Environ Sci Technol **45**, 6633 (2011).

[49] Y. Park, J. Decatur, K. Y. Lin, and A. H. Park, Phys Chem Chem Phys **13**, 18115 (2011).

[50] Y. Park, D. Shin, Y. N. Jang, and A.-H. A. Park, Journal of Chemical & Engineering Data **57**, 40 (2012).

[51] C. Petit, Y. Park, K.-Y. A. Lin, and A.-H. A. Park, The Journal of Physical Chemistry C **116**, 516 (2012).

[52] J. L. Schaefer, S. S. Moganty, D. A. Yanga, and L. A. Archer, Journal of Materials Chemistry **21**, 10094 (2011).

[53] J. L. Nugent, S. S. Moganty, and L. A. Archer, Adv Mater **22**, 3677 (2010).

[54] J. L. Schaefer, D. A. Yanga, and L. A. Archer, Chemistry of Materials **25**, 834 (2013).

[55] M. E. Mackay, T. T. Dao, A. Tuteja, D. L. Ho, B. van Horn, H. C. Kim, and C. J. Hawker, Nature materials **2**, 762 (2003).

[56] A. Tuteja, M. E. Mackay, C. J. Hawker, and B. Van Horn, Macromolecules **38**, 8000 (2005).

[57] A. Tuteja, P. M. Duxbury, and M. E. Mackay, Macromolecules **40**, 9427 (2007).

[58] L. Berthier, G. Biroli, J. P. Bouchaud, L. Cipelletti, D. El Masri, D. L'Hote, F. Ladieu, and M. Pierno, Science **310**, 1797 (2005).

[59] S. Torquato, Nature **405**, 521 (2000).

[60] D. A. Weitz, Science **323**, 214 (2009).

[61] C. A. Angell, Science **267**, 1924 (1995).

[62] P. N. Pusey and W. van Megen, Nature **320**, 340 (1986).

[63] K. N. Pham *et al.*, Science **296**, 104 (2002).

[64] E. R. Weeks, J. C. Crocker, A. C. Levitt, A. Schofield, and D. A. Weitz, Science **287**, 627 (2000).

[65] Z. Zhang *et al.*, Nature **459**, 230 (2009).

[66] J. Mattsson, H. M. Wyss, A. Fernandez-Nieves, K. Miyazaki, Z. Hu, D. R. Reichman, and D. A. Weitz, Nature **462**, 83 (2009).

[67] P. Sollich, F. Lequeux, P. Hébraud, and M. E. Cates, Physical Review Letters **78**, 2020 (1997).

[68] P. Sollich, Physical Review E **58**, 738 (1998).

[69] P. Agarwal, Ph.D., Cornell University, 2012.

[70] L. Cipelletti, S. Manley, R. C. Ball, and D. A. Weitz, Phys Rev Lett **84**, 2275 (2000).

[71] L. Cipelletti, L. Ramos, S. Manley, E. Pitard, D. A. Weitz, E. E. Pashkovski, and M. Johansson, Faraday Discussions **123**, 237 (2003).

[72] A. Madsen, R. L. Leheny, H. Guo, M. Sprung, and O. Czakkel, New Journal of Physics **12**, 055001 (2010).

[73] P. Cassagnau, Polymer **49**, 2183 (2008).

[74] V. Mittal, Materials **2**, 992 (2009).

[75] P. H. C. Camargo, K. G. Satyanarayana, and F. Wypych, Materials Research-Ibero-American Journal of Materials **12**, 1 (2009).

[76] H. Zou, S. Wu, and J. Shen, Chem Rev **108**, 3893 (2008).

[77] B. J. Anderson and C. F. Zukoski, Langmuir : the ACS journal of surfaces and colloids **26**, 8709 (2010).

[78] D. W. Janes, J. F. Moll, S. E. Harton, and C. J. Durning, Macromolecules **44**, 4920 (2011).

[79] J. Moll and S. K. Kumar, Macromolecules **45**, 1131 (2012).

[80] O. Pravaz, B. Droz, P. Schurtenberger, and H. Dietsch, Nanoscale **4**, 6856 (2012).

[81] C. Bartholome, E. Beyou, E. Bourgeat-Lami, P. Cassagnau, P. Chaumont, L. David, and N. Zydowicz, Polymer **46**, 9965 (2005).

[82] C. Derec, G. Ducouret, A. Ajdari, and F. Lequeux, Phys Rev E Stat Nonlin Soft Matter Phys **67**, 061403 (2003).

[83] P. Rittigstein, R. D. Priestley, L. J. Broadbelt, and J. M. Torkelson, Nature materials **6**, 278 (2007).

[84] R. K. Iler.

[85] D. A. Savin, J. Pyun, G. D. Patterson, T. Kowalewski, and K. Matyjaszewski, Journal of Polymer Science Part B: Polymer Physics **40**, 2667 (2002).

[86] Q. Zhang and L. A. Archer, Langmuir : the ACS journal of surfaces and colloids **19**, 8094 (2003).

[87] J. Choi, M. J. A. Hore, J. S. Meth, N. Clarke, K. I. Winey, and R. J. Composto, ACS Macro Letters **2**, 485 (2013).

[88] F. M. Du, R. C. Scogna, W. Zhou, S. Brand, J. E. Fischer, and K. I. Winey, Macromolecules **37**, 9048 (2004).

[89] F. M. Du, J. E. Fischer, and K. I. Winey, Physical Review B **72** (2005).

[90] G. Jiang, M. J. Hore, S. Gam, and R. J. Composto, Acs Nano **6**, 1578 (2012).

[91] M. J. A. Hore and R. J. Composto, Current Opinion in Chemical Engineering **2**, 95 (2013).

[92] N. S. T. Do, D. M. Schaetzl, B. Dey, A. C. Seabaugh, and S. K. Fullerton-Shirey, The Journal of Physical Chemistry C **116**, 21216 (2012).

[93] P. F. Green, Soft Matter **7**, 7914 (2011).

[94] S. K. Kumar, N. Jouault, B. Benicewicz, and T. Neely, Macromolecules **46**, 3199 (2013).

[95] N. J. Fernandes, H. Koerner, E. P. Giannelis, and R. A. Vaia, MRS Communications **3**, 13 (2013).

[96] M. K. Crawford *et al.*, Physical Review Letters **110** (2013).

[97] S. Alexander, Journal de Physique **38**, 983 (1977).

[98] P. G. de Gennes, Macromolecules **13**, 1069 (1980).

[99] S. T. Milner, T. A. Witten, and M. E. Cates, Macromolecules **21**, 2610 (1988).

[100] P. G. Ferreira, A. Ajdari, and L. Leibler, Macromolecules **31**, 3994 (1998).

[101] H. Oh and P. F. Green, Nature materials **8**, 139 (2009).

[102] C. Chevigny, F. Dalmas, E. Di Cola, D. Gigmes, D. Bertin, F. o. Boué, and J. Jestin, Macromolecules **44**, 122 (2011).

[103] Q. Lan, L. F. Francis, and F. S. Bates, Journal of Polymer Science Part B: Polymer Physics **45**, 2284 (2007).

[104] C. Xu, K. Ohno, V. Ladmiral, and R. J. Composto, Polymer **49**, 3568 (2008).

[105] M. E. McEwan, S. A. Egorov, J. Ilavsky, D. L. Green, and Y. Yang, Soft Matter **7**, 2725 (2011).

[106] X. Wang, V. J. Foltz, M. Rackaitis, and G. G. A. Böhm, Polymer **49**, 5683 (2008).

[107] S. Srivastava, P. Agarwal, and L. A. Archer, Langmuir : the ACS journal of surfaces and colloids **28**, 6276 (2012).

[108] D. Sunday, J. Ilavsky, and D. L. Green, Macromolecules **45**, 4007 (2012).

[109] S. Fischer, A. Salcher, A. Kornowski, H. Weller, and S. Forster, Angewandte Chemie **50**, 7811 (2011).

[110] R. S. Ndong and W. B. Russel, Journal of Rheology **55**, 331 (2011).

[111] R. Inoubli, S. Dagreou, A. Lapp, L. Billon, and J. Peyrelasse, Langmuir : the ACS journal of surfaces and colloids **22**, 6683 (2006).

[112] A.-S. Robbes, F. Cousin, F. Meneau, F. Dalmas, R. Schweins, D. Gigmes, and J. Jestin, Macromolecules **45**, 9220 (2012).

[113] S. E. Harton and S. K. Kumar, Journal of Polymer Science Part B: Polymer Physics **46**, 351 (2008).

[114] V. Pryamtisyn, V. Ganesan, A. Z. Panagiotopoulos, H. Liu, and S. K. Kumar, The Journal of chemical physics **131**, 221102 (2009).

[115] G. D. Smith and D. Bedrov, Langmuir : the ACS journal of surfaces and colloids **25**, 11239 (2009).

[116] D. M. Trombly and V. Ganesan, The Journal of chemical physics **133**, 154904 (2010).

[117] J. Kalb, D. Dukes, S. K. Kumar, R. S. Hoy, and G. S. Grest, Soft Matter **7**, 1418 (2011).

[118] T. V. M. Ndoro, E. Voyiatzis, A. Ghanbari, D. N. Theodorou, M. C. Böhm, and F. Müller-Plathe, Macromolecules **44**, 2316 (2011).

[119] R. Hasegawa, Y. Aoki, and M. Doi, Macromolecules **29**, 6656 (1996).

[120] T. B. Martin, P. M. Dodd, and A. Jayaraman, Physical Review Letters **110** (2013).

[121] T. B. Martin and A. Jayaraman, Soft Matter (2013).

[122] M. J. A. Hore, A. L. Frischknecht, and R. J. Composto, ACS Macro Letters **1**, 115 (2012).

[123] A. L. Frischknecht, M. J. A. Hore, J. Ford, and R. J. Composto, Macromolecules **46**, 2856 (2013).

[124] R. B. Thompson, V. V. Ginzburg, M. W. Matsen, and A. C. Balazs, Science **292**, 2469 (2001).

[125] J.-Y. Lee, R. Thompson, D. Jasnow, and A. Balazs, Physical Review Letters **89** (2002).

[126] J. Y. Lee, Z. Shou, and A. C. Balazs, Macromolecules **36**, 7730 (2003).

[127] M. R. Bockstaller, Y. Lapetnikov, S. Margel, and E. L. Thomas, Journal of the American Chemical Society **125**, 5276 (2003).

[128] M. R. Bockstaller, R. A. Mickiewicz, and E. L. Thomas, Advanced Materials **17**, 1331 (2005).

[129] J. J. Chiu, B. J. Kim, E. J. Kramer, and D. J. Pine, Journal of the American Chemical Society **127**, 5036 (2005).

[130] B. J. Kim, J. J. Chiu, G. R. Yi, D. J. Pine, and E. J. Kramer, Advanced Materials **17**, 2618 (2005).

[131] Y. Lin *et al.*, Nature **434**, 55 (2005).

[132] B. J. Kim, J. Bang, C. J. Hawker, and E. J. Kramer, Macromolecules **39**, 4108 (2006).

[133] J. J. Chiu, B. J. Kim, G.-R. Yi, J. Bang, E. J. Kramer, and D. J. Pine, Macromolecules **40**, 3361 (2007).

[134] B. J. Kim, J. Bang, C. J. Hawker, J. J. Chiu, D. J. Pine, S. G. Jang, S. M. Yang, and E. J. Kramer, Langmuir : the ACS journal of surfaces and colloids **23**, 12693 (2007).

[135] S. G. Jang, E. J. Kramer, and C. J. Hawker, Journal of the American Chemical Society **133**, 16986 (2011).

[136] S. G. Jang, A. Khan, C. J. Hawker, and E. J. Kramer, Macromolecules **45**, 1553 (2012).

[137] S. C. Warren, L. C. Messina, L. S. Slaughter, M. Kamperman, Q. Zhou, S. M. Gruner, F. J. DiSalvo, and U. Wiesner, Science **320**, 1748 (2008).

[138] M. Grzelczak, J. Vermant, E. M. Furst, and L. M. Liz-Marzan, Acs Nano **4**, 3591 (2010).

[139] Y. Lin, V. K. Daga, E. R. Anderson, S. P. Gido, and J. J. Watkins, Journal of the American Chemical Society **133**, 6513 (2011).

[140] R. Shenhar, T. B. Norsten, and V. M. Rotello, Advanced Materials **17**, 657 (2005).

[141] A. Haryono and W. H. Binder, Small **2**, 600 (2006).

[142] J. Kao, K. Thorkelsson, P. Bai, B. J. Rancatore, and T. Xu, Chem Soc Rev **42**, 2654 (2013).

[143] P. Akcora *et al.*, Macromolecules **43**, 1003 (2010).

[144] J. F. Moll, P. Akcora, A. Rungta, S. Gong, R. H. Colby, B. C. Benicewicz, and S. K. Kumar, Macromolecules **44**, 7473 (2011).

[145] L. Meli, A. Arceo, and P. F. Green, Soft Matter **5**, 533 (2009).

[146] X. C. Chen and P. F. Green, Soft Matter **7**, 1192 (2011).

[147] V. S. Minnikanti, Z. Qian, and L. A. Archer, The Journal of chemical physics **126**, 144905 (2007).

[148] A.-S. Robbes, F. Cousin, F. Meneau, F. Dalmas, F. Boué, and J. Jestin, Macromolecules **44**, 8858 (2011).

[149] P. G. deGennes, C. R. Acad. Sci. Paris **290**, 509 (1980).

[150] M. Rubinstein and R. H. Colby.

[151] A. Silberberg, Journal of Colloid and Interface Science **125**, 14 (1988).

[152] J. P. Cohen-Addad, Polymer **30**, 1820 (1989).

[153] A. Tuteja, P. Duxbury, and M. Mackay, Physical Review Letters **100**, 077801 (2008).

[154] D. Kim, S. Srivastava, S. Narayanan, and L. A. Archer, Soft Matter **8**, 10813 (2012).

[155] J. T. Kalathi, G. S. Grest, and S. K. Kumar, Phys Rev Lett **109**, 198301 (2012).

[156] R. G. Schmidt, G. V. Gordon, C. c. A. Dreiss, T. Cosgrove, V. J. Krukonis, K. Williams, and P. M. Wetmore, Macromolecules **43**, 10143 (2010).

[157] K. Nusser, G. J. Schneider, W. Pyckhout-Hintzen, and D. Richter, Macromolecules **44**, 7820 (2011).

[158] M. J. Hore and R. J. Composto, Acs Nano **4**, 6941 (2010).

[159] M. J. A. Hore and R. J. Composto, Macromolecules **45**, 6078 (2012).

[160] S. S. Ojha, A. Dang, C. M. Hui, C. Mahoney, K. Matyjaszewski, and M. R. Bockstaller, Langmuir : the ACS journal of surfaces and colloids (2013).

[161] J. Guo, Z. Yang, Y. Yu, H. D. Abruna, and L. A. Archer, Journal of the American Chemical Society **135**, 763 (2013).

[162] A. B. Bourlinos, E. P. Giannelis, Q. Zhang, L. A. Archer, G. Floudas, and G. Fytas, Eur Phys J E Soft Matter **20**, 109 (2006).

[163] A. B. Bourlinos, S. Ray Chowdhury, R. Herrera, D. D. Jiang, Q. Zhang, L. A. Archer, and E. P. Giannelis, Advanced Functional Materials **15**, 1285 (2005).

[164] R. Rodriguez, R. Herrera, A. B. Bourlinos, R. Li, A. Amassian, L. A. Archer, and E. P. Giannelis, Applied Organometallic Chemistry **24**, 581 (2010).

[165] M. L. Jespersen, P. A. Mirau, E. von Meerwall, R. A. Vaia, R. Rodriguez, and E. P. Giannelis, Acs Nano **4**, 3735 (2010).

[166] Q. Li, L. Dong, J. Fang, and C. Xiong, Acs Nano **4**, 5797 (2010).

[167] A. Chremos and A. Z. Panagiotopoulos, Physical Review Letters **107** (2011).

[168] H. Y. Yu and D. L. Koch, Langmuir : the ACS journal of surfaces and colloids (2013).

[169] M. Doi and S. F. Edwards.

[170] M. Doi and N. Kuzuu, J. Polym. Sci., Polym. Phys. Ed. **18**, 775 (1980).

[171] S. Goyal and F. A. Escobedo, The Journal of chemical physics **135**, 184902 (2011).

[172] P. Agarwal, S. Srivastava, and L. A. Archer, Physical Review Letters **107**, 268302 (2011).

[173] A. Chremos, A. Z. Panagiotopoulos, and D. L. Koch, The Journal of chemical physics **136**, 044902 (2012).

[174] H.-Y. Yu, S. Srivastava, L. A. Archer, and D. L. Koch, In preperation.

[175] I. Choi, H. Ahn, and M. J. Park, Macromolecules **44**, 7327 (2011).

[176] P. Agarwal, M. Chopra, and L. A. Archer, Angewandte Chemie **50**, 8670 (2011).

[177] B. V. S. Iyer, I. G. Salib, V. V. Yashin, T. Kowalewski, K. Matyjaszewski, and A. C. Balazs, Soft Matter **9**, 109 (2013).

[178] R. R. Bhattacharjee, R. Li, L. Estevez, D.-M. Smilgies, A. Amassian, and E. P. Giannelis, Journal of Materials Chemistry **19**, 8728 (2009).

[179] R. K. Mallavajula, S. S. Moganty, and L. A. Archer, in preperation.

[180] D. Kim and L. A. Archer, Langmuir : the ACS journal of surfaces and colloids (2011).

[181] Y. Zhang, S. Gu, B. Yan, and J. Ren, Journal of Materials Chemistry **22**, 14843 (2012).

[182] S. S. Moganty, N. Jayaprakash, J. L. Nugent, J. Shen, and L. A. Archer, Angewandte Chemie **49**, 9158 (2010).

[183] S. S. Moganty, S. Srivastava, Y. Lu, J. L. Schaefer, S. A. Rizvi, and L. A. Archer, Chemistry of Materials **24**, 1386 (2012).

[184] Y. Lu, S. K. Das, S. S. Moganty, and L. A. Archer, Adv Mater **24**, 4430 (2012).

[185] Y. Lu, S. S. Moganty, J. L. Schaefer, and L. A. Archer, Journal of Materials Chemistry **22**, 4066 (2012).

[186] I. Villaluenga, X. Bogle, S. Greenbaum, I. Gil de Muro, T. Rojo, and M. Armand, Journal of Materials Chemistry A (2013).

[187] S. M. Liff, N. Kumar, and G. H. McKinley, Nature materials **6**, 76 (2007).

[188] S. S. Sternstein and A.-J. Zhu, Macromolecules **35**, 7262 (2002).

[189] V. Goel, T. Chatterjee, L. Bombalski, K. Yurekli, K. Matyjaszewski, and R. Krishnamoorti, Journal of Polymer Science Part B: Polymer Physics **44**, 2014 (2006).

[190] C. Chevigny, N. Jouault, F. Dalmas, F. Boué, and J. Jestin, Journal of Polymer Science Part B: Polymer Physics **49**, 781 (2011).

[191] M. McEwan and D. Green, Soft Matter **5**, 1705 (2009).

[192] D. Maillard, S. K. Kumar, B. Fragneaud, J. W. Kysar, A. Rungta, B. C. Benicewicz, H. Deng, L. C. Brinson, and J. F. Douglas, Nano letters **12**, 3909 (2012).

[193] R. Krishnamoorti, MRS Bulletin **32**, 341 (2011).

[194] D. H. Napper, *Polymeric stabilization of colloidal dispersions* (Academic Press London, 1983), Vol. 7.

[195] F. Hussain, M. Hojjati, M. Okamoto, and R. E. Gorga, Journal of Composite Materials **40**, 1511 (2006).

[196] G. Schmidt and M. M. Malwitz, Current Opinion in Colloid & Interface Science **8**, 103 (2003).

[197] Z. Zhang, M. A. Horsch, M. H. Lamm, and S. C. Glotzer, Nano letters **3**, 1341 (2003).

[198] M. R. Jones, R. J. Macfarlane, B. Lee, J. Zhang, K. L. Young, A. J. Senesi, and C. A. Mirkin, Nature materials **9**, 913 (2010).

[199] G. Lindenblatt, W. Schärtl, T. Pakula, and M. Schmidt, Macromolecules **34**, 1730 (2001).

[200] K. Ohno, T. Morinaga, S. Takeno, Y. Tsujii, and T. Fukuda, Macromolecules **40**, 9143 (2007).

[201] N. Dutta and D. Green, Langmuir : the ACS journal of surfaces and colloids **24**, 5260 (2008).

[202] D. Dukes, Y. Li, S. Lewis, B. Benicewicz, L. Schadler, and S. K. Kumar, Macromolecules **43**, 1564 (2010).

[203] C. Chevigny, J. Jestin, D. Gigmes, R. Schweins, E. Di-Cola, F. Dalmas, D. Bertin, and F. o. Boué, Macromolecules **43**, 4833 (2010).

[204] S. Gupta, Q. Zhang, T. Emrick, A. C. Balazs, and T. P. Russell, Nature materials **5**, 229 (2006).

[205] Q. Wang and L. Zhu, Journal of Polymer Science Part B: Polymer Physics **49**, 1421 (2011).

[206] G. Han, P. Ghosh, and V. M. Rotello, Nanomedicine (Lond) **2**, 113 (2007).

[207] S. D. Brown *et al.*, Journal of the American Chemical Society **132**, 4678 (2010).

[208] A. Bergmann, G. Fritz, and O. Glatter, Journal of Applied Crystallography **33**, 1212 (2000).

[209] Q. Zhang and L. A. Archer, Langmuir : the ACS journal of surfaces and colloids **22**, 717 (2006).

[210] Q. Zhang, Q. Zhang, and L. A. Archer, J Phys Chem B **110**, 4924 (2006).

[211] T. A. Witten and P. A. Pincus, Macromolecules **19**, 2509 (1986).

[212] K. A. Cogan, M. Capel, and A. P. Gast, Macromolecules **24**, 6512 (1991).

[213] A. Chremos, A. Z. Panagiotopoulos, H. Y. Yu, and D. L. Koch, The Journal of chemical physics **135**, 114901 (2011).

[214] J. Ilavsky and P. R. Jemian, Journal of Applied Crystallography **42**, 347 (2009).

[215] L. Berthier, A. J. Moreno, and G. Szamel, Physical Review E **82**, 060501 (2010).

[216] M. J. Pond, J. R. Errington, and T. M. Truskett, The Journal of chemical physics **134** (2011).

[217] M. J. Pond, J. R. Errington, and T. M. Truskett, Soft Matter **7**, 9859 (2011).

[218] X. Cheng, Physical Review E **81** (2010).

[219] X. Cheng, Soft Matter **6**, 2931 (2010).

[220] G. A. McConnell and A. P. Gast, Macromolecules **30**, 435 (1997).

[221] S. Graves, K. Meleson, J. Wilking, M. Y. Lin, and T. G. Mason, The Journal of chemical physics **122** (2005).

[222] M. Watzlawek, H. Löwen, and C. N. Likos, Journal of Physics: Condensed Matter **10**, 8189 (1998).

[223] G. Foffi, F. Sciortino, P. Tartaglia, E. Zaccarelli, F. Verso, L. Reatto, K. Dawson, and C. Likos, Physical Review Letters **90** (2003).

[224] L. Silbert, A. Liu, and S. Nagel, Physical Review E **73** (2006).

[225] H. Jacquin, L. Berthier, and F. Zamponi, Physical Review Letters **106** (2011).

[226] P. Agarwal and L. A. Archer, Physical Review E **83**, 041402 (2011).

[227] W. B. Russel, D. A. Saville, and W. R. Schowalter, *Colloidal Dsipersions* (Cambridge University Press, New York, 1992), Cambridge Monographs on Mechanics and Applied Mathematics.

[228] R. C. Ball, J. F. Marko, S. T. Milner, and T. A. Witten, Macromolecules **24**, 693 (1991).

[229] D. Vlassopoulos, Journal of Polymer Science Part B: Polymer Physics **42**, 2931 (2004).

[230] C. Christopoulou, G. Petekidis, B. Erwin, M. Cloitre, and D. Vlassopoulos, Philosophical Transactions of the Royal Society A: Mathematical, Physical and Engineering Sciences **367**, 5051 (2009).

[231] E. Stiakakis, A. Wilk, J. Kohlbrecher, D. Vlassopoulos, and G. Petekidis, Physical Review E **81**, 020402 (2010).

[232] S. A. Rogers, P. T. Callaghan, G. Petekidis, and D. Vlassopoulos, Journal of Rheology (1978-present) **54**, 133 (2010).

[233] B. M. Erwin, D. Vlassopoulos, M. Gauthier, and M. Cloitre, Physical Review E **83**, 061402 (2011).

[234] D. Vlassopoulos, G. Fytas, S. Pispas, and N. Hadjichristidis, Physica B: Condensed Matter **296**, 184 (2001).

[235] G. A. McConnell, A. P. Gast, J. S. Huang, and S. D. Smith, Physical Review Letters **71**, 2102 (1993).

[236] G. A. McConnell, M. Y. Lin, and A. P. Gast, Macromolecules **28**, 6754 (1995).

[237] A. P. Gast, Langmuir : the ACS journal of surfaces and colloids **12**, 4060 (1996).

[238] S. Förster, M. Zisenis, E. Wenz, and M. Antonietti, The Journal of chemical physics **104**, 9956 (1996).

[239] J. Buitenhuis and S. Förster, The Journal of chemical physics **107**, 262 (1997).

[240] H. Watanabe, Acta Polymerica **48**, 215 (1997).

[241] B. Loppinet, G. Fytas, D. Vlassopoulos, C. N. Likos, G. Meier, and G. J. Liu, Macromolecular Chemistry and Physics **206**, 163 (2005).

[242] E. van Ruymbeke, A. Pamvouxoglou, D. Vlassopoulos, G. Petekidis, G. Mountrichas, and S. Pispas, Soft Matter **6**, 881 (2010).

[243] F. Renou, J. Stellbrink, and G. Petekidis, Journal of Rheology (1978-present) **54**, 1219 (2010).

[244] V. Carrier and G. Petekidis, Journal of Rheology (1978-present) **53**, 245 (2009).

[245] R. Höhler and S. Cohen-Addad, Journal of Physics: Condensed Matter **17**, R1041 (2005).

[246] C. Prestidge and T. F. Tadros, Journal of Colloid and Interface Science **124**, 660 (1988).

[247] W. J. Frith, T. A. Strivens, and J. Mewis, Journal of Colloid and Interface Science **139**, 55 (1990).

[248] D. A. R. Jones, B. Leary, and D. V. Boger, Journal of Colloid and Interface Science **150**, 84 (1992).

[249] J. Mewis and P. D. Haene, Makromolekulare Chemie. Macromolecular Symposia **68**, 213 (1993).

[250] U. Genz, B. D'Aguanno, J. Mewis, and R. Klein, Langmuir : the ACS journal of surfaces and colloids **10**, 2206 (1994).

[251] L. Raynaud, B. Ernst, C. Vergé, and J. Mewis, Journal of Colloid and Interface Science **181**, 11 (1996).

[252] A. Grand and G. Petekidis, Rheol Acta **47**, 579 (2008).

[253] R. G. Larson, *The Structure and Rheology of Complex Fluids* (OUP USA, 1999).

[254] X. Cheng, J. H. McCoy, J. N. Israelachvili, and I. Cohen, Science **333**, 1276 (2011).

[255] Q. D. Nguyen and D. V. Boger, Annual Review of Fluid Mechanics **24**, 47 (1992).

[256] J. R. Stokes and J. H. Telford, Journal of Non-Newtonian Fluid Mechanics **124**, 137 (2004).

[257] V. Kobelev and K. S. Schweizer, Physical Review E **71** (2005).

[258] W. van Megen and P. N. Pusey, Physical Review A **43**, 5429 (1991).

[259] T. Mason and D. Weitz, Physical Review Letters **75**, 2770 (1995).

[260] M. Cloitre, R. Borrega, and L. Leibler, Physical Review Letters **85**, 4819 (2000).

[261] M. Siebenbürger, M. Fuchs, H. Winter, and M. Ballauff, Journal of Rheology **53**, 707 (2009).

[262] T. Mason, J. Bibette, and D. Weitz, Physical Review Letters **75**, 2051 (1995).

[263] L. Ramos and L. Cipelletti, Physical Review Letters **87**, 245503 (2001).

[264] S. M. Fielding, P. Sollich, and M. E. Cates, Journal of Rheology **44**, 323 (2000).

[265] S. Jo and K. Park, Biomaterials **21**, 605 (2000).

[266] D. K. Aswal, S. Lenfant, D. Guerin, J. V. Yakhmi, and D. Vuillaume, Analytica Chimica Acta **568**, 84 (2006).

[267] G. B. M. P. A. O'Connell, Polymer Engineering & Science **37**, 1485 (1997).

[268] P. A. O'Connell and G. B. McKenna, Mechanics of Time-Dependent Materials **6**, 207 (2002).

[269] J. D. Ferry, *Viscoelastic Properties of Polymers* (Wiley, 1980).

[270] P. Sollich, F. Lequeux, P. H 閎 raud, and M. E. Cates, Phys. Rev. Lett. **78**, 2020 (1997).

[271] C. Daniel, I. W. Hamley, M. Wilhelm, and W. Mingvanish, Rheol. Acta **40**, 39 (2001).

[272] H. Wyss, K. Miyazaki, J. Mattsson, Z. Hu, D. Reichman, and D. Weitz, Physical Review Letters **98**, 238303 (2007).

[273] D. R. Paul and L. M. Robeson, Polymer **49**, 3187 (2008).

[274] M. E. Baur and W. H. Stockmayer, The Journal of chemical physics **43**, 4319 (1965).

[275] H. Watanabe, Macromolecular Rapid Communications **22**, 127 (2001).

[276] A. Einstein, Annalen der Physik **17**, 549 (1905).

[277] G. K. Batchelor, Journal of Fluid Mechanics **83**, 97 (1977).

[278] P. R. Couchman, Physics Letters A **70**, 155 (1979).

[279] C. A. Angell, K. L. Ngai, G. B. McKenna, P. F. McMillan, and S. W. Martin, J Appl Phys **88**, 3113 (2000).

[280] P. G. Santangelo, C. M. Roland, K. L. Ngai, A. K. Rizos, and H. Katerinopoulos, Journal of Non-Crystalline Solids **172–174, Part 2**, 1084 (1994).

[281] R. L. Leheny, Current Opinion in Colloid & Interface Science **17**, 3 (2012).

[282] S. Narayanan, D. Lee, A. Hagman, X. Li, and J. Wang, Physical Review Letters **98**, 185506 (2007).

[283] H. Guo *et al.*, Physical Review Letters **102**, 075702 (2009).

[284] A. Scala, F. W. Starr, E. La Nave, F. Sciortino, and H. E. Stanley, Nature **406**, 166 (2000).

[285] J. R. Errington and P. G. Debenedetti, Nature **409**, 318 (2001).

[286] M. S. Shell, P. G. Debenedetti, and A. Z. Panagiotopoulos, Physical Review E **66**, 011202 (2002).

[287] A. Barros de Oliveira, P. A. Netz, T. Colla, and M. C. Barbosa, The Journal of chemical physics **124** (2006).

[288] W. P. Krekelberg, T. Kumar, J. Mittal, J. R. Errington, and T. M. Truskett, Physical Review E **79**, 031203 (2009).

[289] P. Kumar, S. V. Buldyrev, F. Sciortino, E. Zaccarelli, and H. E. Stanley, Physical Review E **72**, 021501 (2005).

[290] J. R. Errington, T. M. Truskett, and J. Mittal, The Journal of chemical physics **125** (2006).

[291] P. N. Pusey and W. van Megen, Physical Review Letters **59**, 2083 (1987).

[292] C. Mayer *et al.*, Nature materials **7**, 780 (2008).

[293] K. R. Harris and L. A. Woolf, Journal of the Chemical Society, Faraday Transactions 1: Physical Chemistry in Condensed Phases **76**, 377 (1980).

[294] K. R. Harris and P. J. Newitt, Journal of Chemical & Engineering Data **42**, 346 (1997).

[295] G. Brambilla, D. El Masri, M. Pierno, L. Berthier, L. Cipelletti, G. Petekidis, and A. Schofield, Physical Review Letters **102** (2009).

[296] R. Bandyopadhyay, D. Liang, H. Yardimci, D. A. Sessoms, M. A. Borthwick, S. G. J. Mochrie, J. L. Harden, and R. L. Leheny, Physical Review Letters **93** (2004).

[297] H. Guo, J. Wilking, D. Liang, T. Mason, J. Harden, and R. Leheny, Physical Review E **75** (2007).

[298] H. Guo, S. Ramakrishnan, J. L. Harden, and R. L. Leheny, The Journal of chemical physics **135**, 154903 (2011).

[299] R. Brown, Phil. Mag. **4**, 161 (1828).

[300] A. Einstein, Annalen der Physik **322**, 549 (1905).

[301] P.-G. de Gennes, Angewandte Chemie International Edition in English **31**, 842 (1992).

[302] M. D. Ediger, Annu Rev Phys Chem **51**, 99 (2000).

[303] A. Duri, D. Sessoms, V. Trappe, and L. Cipelletti, Physical Review Letters **102**, 085702 (2009).

[304] L. Cipelletti and L. Ramos, Journal of Physics: Condensed Matter **17**, R253 (2005).

[305] R. Narayanan, P. Thiyagarajan, S. Lewis, A. Bansal, L. Schadler, and L. Lurio, Physical Review Letters **97**, 075505 (2006).

[306] O. Lieleg, J. Kayser, G. Brambilla, L. Cipelletti, and A. R. Bausch, Nature materials **10**, 236 (2011).

[307] S. Mazoyer, L. Cipelletti, and L. Ramos, Physical Review E **79**, 011501 (2009).

[308] B. Ruta, Y. Chushkin, G. Monaco, L. Cipelletti, E. Pineda, P. Bruna, V. M. Giordano, and M. Gonzalez-Silveira, Physical Review Letters **109**, 165701 (2012).

[309] P. Langevin, C.R. Acad. Sci. Paris **146**, 530 (1908).

[310] C. Caronna, Y. Chushkin, A. Madsen, and A. Cupane, Physical Review Letters **100**, 055702 (2008).

[311] J. P. Bouchaud and E. Pitard, Eur Phys J E Soft Matter **9**, 287 (2002).